



Investigation of a new way of synthesis for Nano crystallites of $\text{La}_2\text{O}_2\text{S}$ & $1\%\text{Ln}^{3+}$ ($\text{Ln} = \text{Pr}, \text{Eu}, \text{Tb}, \text{Dy}, \text{Er}$) doped $\text{La}_2\text{O}_2\text{S}$ and study their structural and optical properties



Kevil Shah ^{a,*}, Aleksandar Ćirić ^b, K.V.R. Murthy ^a, B.S. Chakrabarty ^a

^a Luminescence Lab, Applied Physics Department, Faculty of Technology & Engineering, The Maharaja Sayajirao University of Baroda, Vadodara, Gujarat, India

^b University of Belgrade, Vinca Institute of Nuclear Sciences, 11001, Belgrade, Serbia

ARTICLE INFO

Article history:

Received 11 June 2020

Received in revised form

8 July 2020

Accepted 13 August 2020

Available online 27 August 2020

Keywords:

XRD Study

Combustion technique

UV – Visible spectroscopy

Photoluminescence spectroscopy

EDAX Spectra

ABSTRACT

Nano-crystallite Lanthanum oxysulfide ($\text{La}_2\text{O}_2\text{S}$), a versatile compound with a wide range of applications, has been synthesized by the Solid State, Hydrothermal, and a novel Furnace Combustion technique. The last one limits the precursors, thus minimizing the resource usage, does not require passing of the H_2S , CS_2 , or any of the hazardous gasses during the reaction and is less time-consuming while providing the maximum yield output. Thus, the novel Furnace Combustion method is marked for potential industrial use. The comparative XRD analysis showed the highest phase purity of the samples created by the Furnace Combustion technique, which was then employed for the synthesis of $1\% \text{Ln}^{3+}:\text{La}_2\text{O}_2\text{S}$ ($\text{Ln} = \text{Pr}, \text{Eu}, \text{Tb}, \text{Dy}, \text{Er}$) samples. The crystallite size was estimated by the Scherrer equation. The EDAX spectra proved the successful incorporation of doped elements. The samples showed absorption peaks in the UV region attributed to the excitation into $4f5d$ for Pr^{3+} and Tb^{3+} , charge-transfer state for Eu^{3+} , host absorption for Dy^{3+} and $4f$ levels for Er^{3+} doped samples. The emission spectra showed $4f - 4f$ transitions typical for the doped rare-earth ions. The bandgap energies are estimated by the Tauc plot. The 4.95 eV band-gap of pristine $\text{La}_2\text{O}_2\text{S}$ is significantly dropped by doping. The refractive index values slightly increased by doping with rare-earth ions from 2.00 for the pure sample to ca. 2.20 for the doped samples.

© 2020 Elsevier B.V. All rights reserved.

1. Introduction

The advancement in the field of nanotechnology and material science has provided a thrust in the exploration of various compounds and materials and has played an important role in optimizing the functionality of the materials. This advancement has worked as a catalyst especially in the area of luminescence which has significantly increased the demand for rare-earth-doped optical materials owing to their wide range of applicability [1–5]. Photoluminescence occurs when the material absorbs at least one photon and spontaneously emits another with a different energy, the process depending upon the structure of phosphor materials, surrounding environment and type of activators used [6–8]. Most of the phosphor materials and activators are rare earth based

compounds or rare earth elements. There are seventeen rare earth elements and they have similar chemical properties but differ in physical properties due to their electronic structure. All have unique optical properties. Their similar characteristics are due to the same order of magnitude of Coulomb and spin-orbit interactions. (Thus the intermediate coupling scheme applies). Besides, they have partially filled $4f$ orbital surrounded by completely filled $5s$ and $5p$ orbitals which makes the radial wave function of $4f$ orbitals less extended than $5s$ and $5p$ orbitals [1].

The rare-earth compounds are intensively used in high-performance luminescence and display devices such as solid-state lighting, field emission diodes, in-vivo fluorescence imaging, MRI imaging, UV-LED, LASER, etc. Their use especially in the biotechnological field is because of the sharp inter-configurational transition lines between $4f$ levels [2,9,10]. The rare-earth hosts doped with another lanthanide ion are very efficient luminescent materials due to their high thermal stability, low phonon energy, and high rates of energy transfer. Rare-earth materials have played an important role not only in optical technology but also in all high-

* Corresponding author.

E-mail addresses: shah.kevil-apphy@msubaroda.ac.in (K. Shah), aleksandar.ciric@ff.bg.ac.rs (A. Ćirić), drmurthykvr@yahoo.com (K.V.R. Murthy), bschakrabarty-apphy@msubaroda.ac.in (B.S. Chakrabarty).

tech industries such as petrochemical, ceramics, electronics, agriculture, lamps, laser, magnetic materials, metallurgy, biological, pharmaceutical, etc [2,11,12]. Due to the wide range of applications associated with the rare earth materials, they were the preferred choice for this study.

The rare-earth oxysulfides are becoming more industrially relevant. They are an excellent laboratory system for the systematic investigation of rare-earth luminescence because virtually all rare-earth doped activators exhibit high luminescent efficiency and have the same crystallographic structure regardless of the ion size [13]. Lanthanum oxysulfide is uniaxial $p\bar{3}m$ crystal (hexagonal) and wide indirect bandgap (4.6eV–4.8eV) semiconductor material [14,15]. This wide-bandgap enables to minimize the phonon emission, giving a good ground for the efficient photoluminescence [16]. Lanthanum oxysulfide has high thermal as well as chemical stability, making it a potentially applicable material in scientific and industrial field such as steel industry [17,18,21], as a catalyst [20,21], in Ceramic industry [25], for lasing [22] and as electroluminescent [23] and photoconductive material [24] e.g. Bi: La₂O₂S is used as cathodoluminescent material [25]. The Eu³⁺: La₂O₂S is used in surface temperature imaging [30], as a non-contact optical temperature sensor [26,27] and as a scintillator in optical fiber sensors for detecting UV radiation in real-time [28]. Tb³⁺: La₂O₂S is used as an optical sensor for human skin temperature measurements [29] and in X-ray imaging [30].

Lanthanum Oxysulfide has been synthesized by several methods such as Solid State reaction (in which nitrate is firstly converted into Oxalate and then Oxalate gets decomposed into oxysulfide [31–33]), Sulfur – Carbonate flux method [34], Rose's mixture flux technique [35], by passing H₂S gas at high temperature [36–38], by sulfurization agent in molten alkali metal salts [39], Catalyst technique [40,41], Gel thermolysis [42], by combustion reaction with dithiooxamide as fuel [43], by a two-step method involving combustion followed with Solid State technique [44], by Solid State reaction with sulfurization flux (Na₂CO₃ and S powder) [45], Precipitation method [46,47], by two step method involving hydrothermal followed by solid state method [48], by passing N₂/H₂ gas mixture [49], Solid State flux method [50], Reflux method [51], Solid State reaction by passing H₂S/N₂ gas, Solid State reaction by passing CS₂/CO gas in material which is pre synthesized by hydrothermal method [52], by thermal decomposition in eutectic molten salt [53], One step flux method [54] and finally, ethanol assisted combustion technique [18,55].

In this paper, two studies have been discussed. The first one is a comparative study of structural data from XRD studies of samples synthesized by different synthesis techniques. Three different techniques were used to synthesize Lanthanum oxysulfide namely, solid-state reaction, hydrothermal reaction and furnace combustion technique. Here the approach was to minimize the resources used by limiting the number of precursors, avoid the use of H₂S, CS₂, or any hazardous gases during the reaction, produce maximum yield in less time thus expecting it to become an industrially friendly technique. The analysis of the structural parameters from XRD suggests that the furnace combustion technique was the best technique for synthesis of the Lanthanum oxysulfide. In this technique, Lanthanum Nitrate Hexahydrate and Thiourea (an organo-sulfur compound) were used as precursors with urea – ethanol as fuel with no pre- or post-treatment. It produced high yield for a brief production time of only 20 min. This technique is briefly described in the experimental as well as in result and analysis sections. It differs from the previously used ethanol combustion technique. In the previous method, thioacetamide was used as a precursor, and pre- or post-treatment was required for completing the process.

The second study covers the analysis of the morphology, optical and photoluminescence properties of various Lanthanide ions doped in La₂O₂S. The five samples 1%Pr³⁺: La₂O₂S, 1%Eu³⁺: La₂O₂S, 1%Tb³⁺: La₂O₂S, 1%Dy³⁺: La₂O₂S, and 1%Er³⁺: La₂O₂S were synthesized by furnace combustion technique. According to our knowledge, we are the first to report this kind of industrial friendly, furnace combustion technique for the synthesis of Lanthanum oxysulfide.

2. Experimental procedure

Firstly, three techniques namely, solid-state technique, hydrothermal technique, and Furnace combustion technique were used to synthesize the pristine Lanthanum oxysulfide. Two samples were synthesized by the Solid State Technique. The precursors for the first sample were Lanthanum nitrate hexahydrate (La(NO₃)₃·6H₂O) and thiourea (NH₂CSNH₂). The mixture of these materials was put in the crucible and kept in the furnace at 1000 °C for 8 h. For the second sample, same precursors were used with the addition of sulfur powder used as a flux. The mixture was kept in the furnace for 8 h at 1000 °C. After the reaction, both the samples were allowed to cool down naturally. Both samples were in the form of porous layers, which were crushed into fine powder form by using a mortar pestle.

Two samples were synthesized by the hydrothermal technique. The precursors for the first sample were Lanthanum nitrate hexahydrate (La(NO₃)₃·6H₂O) and thiourea (NH₂CSNH₂). They were dissolved in 100 ml distilled water, stirred for 5 min and then transferred in an autoclave maintained at 250 °C and kept for 24 h. The same precursors were used for the second sample but with added flux (sulfur powder). The method followed was the same. Products were filtered and washed by deionized water and dried at 150 °C for 2 h in oven. Mortar pestle was used to turn the products into fine powder.

Two samples were synthesized by Furnace combustion technique. The precursors for the first sample were Lanthanum nitrate hexahydrate (La(NO₃)₃·6H₂O) and thiourea (NH₂CSNH₂) along with 2 g m of Urea as fuel, 5 ml of ethanol and 10 ml of deionized water. They were mixed to form a solution, poured in a crucible and heated in the furnace till combustion began. The same precursors were used for the second sample with addition of flux (sulfur powder). Same method was followed. The combustion started on a full scale in about 20 min at the temperature of 490 °C. Massive amount of fumes were released in either cases. Products were allowed to cool down naturally in the furnace. After 24 h, the obtained samples were crushed into fine powder form by using a mortar – pestle. A higher yield was obtained in this case.

XRD technique was used for the structural characterization of the six samples. UV – Visible technique was used for the optical characterization of only one sample synthesized by the furnace combustion method without flux.

The XRD characterization of both samples synthesized by Furnace combustion technique (with and without flux) showed better results. With these results, it was clear that the samples synthesized by Furnace combustion technique with and without flux have better structural properties. However, the sample synthesized using sulfur as flux would have environmental consequences. Hence, it was decided to use the method without the use of flux to synthesize the five rare earth elements doped Lanthanum oxysulfide. All the samples were synthesized at 1% doping ratio to the host. They are 1% Pr³⁺: La₂O₂S, 1% Eu³⁺: La₂O₂S, 1% Tb³⁺: La₂O₂S, 1% Dy³⁺: La₂O₂S and 1% Er³⁺: La₂O₂S. All dopant ions were in the form of their Nitrate Hexahydrates with 99.9% purity, procured from reputed commercial vendors.

As an illustration, for the synthesis of 1% Pr³⁺: La₂O₂S,

stoichiometric amounts of Praseodymium nitrate hexahydrate ($\text{Pr}(\text{NO}_3)_3 \cdot 6\text{H}_2\text{O}$), Lanthanum nitrate hexahydrate ($\text{La}(\text{NO}_3)_3 \cdot 6\text{H}_2\text{O}$) and thiourea (NH_2CSNH_2) were taken along with 2 g m of Urea as fuel, 5 ml ethanol and 10 ml deionized water. The process followed has been already described above. Similar procedure was used for the synthesis of 1% Eu^{3+} : $\text{La}_2\text{O}_2\text{S}$, 1% Tb^{3+} : $\text{La}_2\text{O}_2\text{S}$, 1% Dy^{3+} : $\text{La}_2\text{O}_2\text{S}$, and 1% Er^{3+} : $\text{La}_2\text{O}_2\text{S}$.

The XRD, UV – Visible, EDAX & Photoluminescence studies were carried out for all these doped samples to analyze their structural, morphological, optical & photoluminescence properties.

3. Results and analysis

3.1. Structural and morphological analysis

A Bruker X-ray diffractometer was used for the study of phase and structural characterization of the samples. The $\text{Cu K}\alpha$ radiation of 1.54 \AA was used for a scanning interval between 5° and 75° .

Fig. 1 shows the XRD pattern of the six samples of undoped $\text{La}_2\text{O}_2\text{S}$ synthesized by the three techniques mentioned above, with and without flux. The structural parameters obtained from the XRD pattern are given in Table 1. It is clear from the table that the solid-state and hydrothermal techniques with and without flux does not give single-phase $\text{La}_2\text{O}_2\text{S}$.

In **solid-state technique** with and without flux, the synthesized phase was bis Oxolanthanum Sulfate. The peaks match with ICDD/JCPDS file no. 85-1535 with a space group of monoclinic lattice.

In the **hydrothermal technique** without flux, the phase corresponds to Lanthanum Hydroxide Sulfate. All Peaks match with JCPDS file no. 73-5330. The hydroxide phase gets removed with the addition of flux in precursors and the phase is again stabilized as bis Oxolanthanum Sulfate.

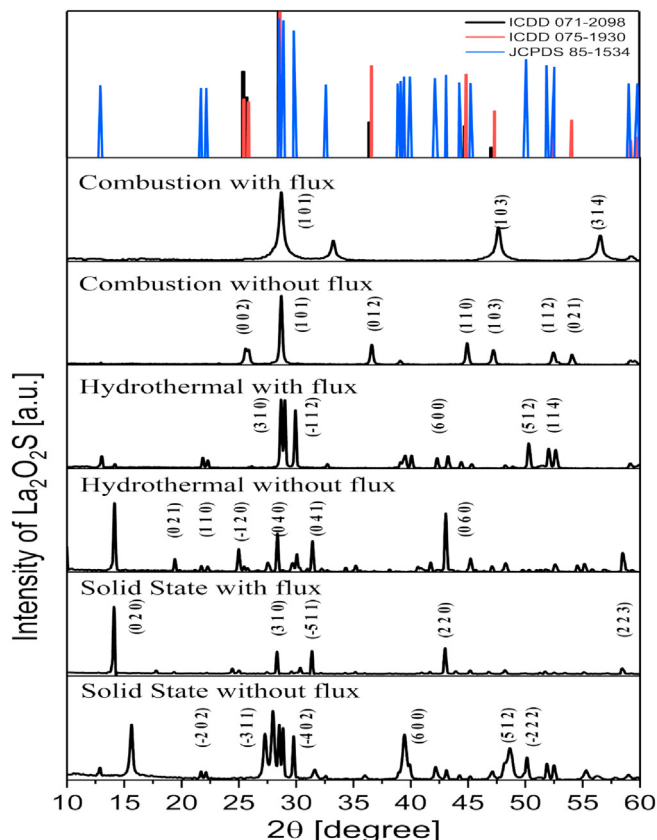


Fig. 1. XRD of undoped $\text{La}_2\text{O}_2\text{S}$.

In the **furnace combustion technique** with and without flux, the XRD pattern makes it clear that it is a single phase hexagonal lattice and a highly crystalline structure. All peaks match with JCPDS file no. 75-1930 for the sample without flux and with JCPDS file no. 71-2098 for the sample with flux. The highest intensity peaks in both these cases were observed at a 2θ value of 28.90° corresponding to hkl plane (1 0 1). The lattice parameters from ICDD file number 75-1930 for the sample without flux are $a (A^\circ) = b (A^\circ) = 4.0344$ & $c (A^\circ) = 6.9016$. For the sample with flux, the lattice parameters as per ICDD file number 71-2098 are $a (A^\circ) = b (A^\circ) = 4.0313$ & $c (A^\circ) = 6.9097$. The numbers of peaks for the sample with flux are less in comparison to the number of peaks for the sample without flux. Peak broadening is also observed in the sample with flux. This makes the furnace combustion technique with and without flux, a more appropriate technique for the synthesis of a hexagonal lattice of Lanthanum Oxysulfide. However, looking to the fact that the sample with flux needs sulfur for the purpose of synthesis, it was thought to be appropriate to use the furnace combustion technique without flux for synthesis of the samples to be studied. It would also limit the needed resources.

Fig. 2 shows the XRD patterns of doped $\text{La}_2\text{O}_2\text{S}$ samples in comparison with the XRD pattern of pristine $\text{La}_2\text{O}_2\text{S}$, with apparent variation of peaks. The number of peaks increased compared to pristine $\text{La}_2\text{O}_2\text{S}$, and the XRD also detected the incorporated rare-earth ions in the host. The peaks of all doped $\text{La}_2\text{O}_2\text{S}$ materials were the same. Almost all peaks of doped $\text{La}_2\text{O}_2\text{S}$ showed larger broadening than the broadening of peaks of the pristine $\text{La}_2\text{O}_2\text{S}$. The first peak at 2θ value of 12.104° was matched with ICDD card number 27-0263, the four peaks at 2θ values of 28.35° , 36.20° , 39.72° and 52.25° were matched with ICDD card number 75-1930, three peaks at 2θ values of 27.54° , 48.93° & 55.43° were matched with ICDD card number 75-1954 and one peak at 2θ value of 47.31° was matched with ICDD card number 71-2098. All these cards were of the single hexagonal lattice. The highest peak at 2θ value of $28^\circ 35'$ with the hkl plane (1 0 1) was the same as compared with the highest intensity peak of pristine $\text{La}_2\text{O}_2\text{S}$. Table 2 presents the structural data of 1% Ln^{3+} : $\text{La}_2\text{O}_2\text{S}$, as extracted from the XRD and compared with pristine $\text{La}_2\text{O}_2\text{S}$. From the table it may be concluded that the crystallite size and volume of the unit cell decrease in comparison to the pristine sample. The atomic radius decreases in the order $\text{La} > \text{Pr} > \text{Eu} > \text{Tb} > \text{Dy} > \text{Er}$, i.e. all rare-earth dopant elements have an ionic radius less than the host element Lanthanum, the reason behind the decrease in crystallite size and volume of the unit cell and the peaks shifting in XRD. If dopant size is smaller than the base metal, it occupies the interstitial position leading to change in the lattice structure. The d spacing between the atoms shrunk, resulting in increase of the peaks at larger angles, as is evident from Fig. 2. For the calculation of lattice parameters, all peaks were compared with standard hkl values. The values of lattice parameters were calculated from the peaks. They are: $a (A^\circ) = b (A^\circ) = 3.73$ and $c (A^\circ) = 7.40$. Fig. 3 displays the EDAX Spectrum of $\text{La}_2\text{O}_2\text{S}$ and 1% Ln^{3+} : $\text{La}_2\text{O}_2\text{S}$ samples. The spectra showed traces of all lanthanide ions doped into the Lanthanum oxysulfide and also identified the elemental composition of the material. Table 3 shows the data extracted from the EDAX spectrum with an atomic percentage of composition and Table 4 gives the data with weight percentage, proving that the composition of every 1% Ln^{3+} : $\text{La}_2\text{O}_2\text{S}$ sample is of high purity. The results clearly indicate that the incorporation of dopant is substitutional in nature.

3.2. UV – visible analysis

Shimadzu make UV-Visible Spectrometer was used for characterization of pristine $\text{La}_2\text{O}_2\text{S}$ as well as five dopant samples of 1% Ln^{3+} : $\text{La}_2\text{O}_2\text{S}$. Fig. 4 shows the absorbance characteristics of pristine

Table 1
Structural data from the XRD spectra of three different synthesis roots.

Synthesis Methods	Phase Name with space group	ICDD	Avg. Crystallite Size (nm)	Density (g/cm ³)	Volume (Å ³)
Solid State					
Without Flux	La ₂ O ₆ S(15:C12/C1) 085-1535 52.21 5.466 Oxolanthanum sulfate				493.21
With flux 1%	La ₂ O ₆ S(15:C12/C1) 085-1535 68.38 5.532 Oxolanthanum sulfate				487.34
Hydrothermal					
Without flux	La(OH)SO ₄ (14:P121/n1) 073-5330 84.87 4.37 Lanthanum hydroxide sulfate				484.33
1%flux	La ₂ O ₆ S(15:C12/C1) 085-1535 74.58 5.56 Oxolanthanum sulfate				382.36
Furnace combustion					
Without flux	La ₂ O ₂ S(164:P-3m1) 075-1930 31.9 5.83 Lanthanum oxysulfide				97.28
1%flux	La ₂ O ₂ S(164:P-3m1) 071-2098 30.7 5.83 Lanthanum oxysulfide				97.25

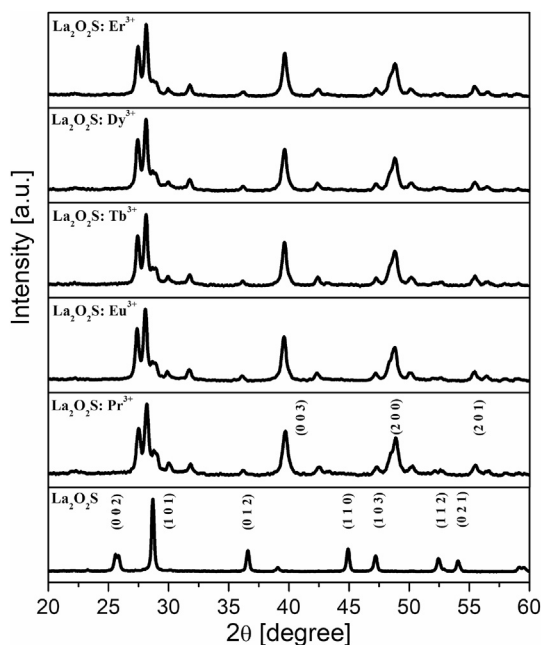


Fig. 2. XRD pattern of pristine La₂O₂S and 1%Ln³⁺: La₂O₂S.

La₂O₂S and the corresponding Tauc plot. Fig. 5 presents the absorbance graph of the other five 1% Ln³⁺: La₂O₂S samples. A 0.05 M aqueous solution was used for UV – Visible analysis. Fig. 6 shows the Tauc plot for the optical band gap of all five samples of 1% Ln³⁺: La₂O₂S.

Table 5 gives the data of the wavelength at which maximum absorbance occurs, optical bandgap and refractive index according to the standard procedures mentioned elsewhere [56,57]. The molar extinction coefficient was calculated using Beer – Lambert law. There is a significant difference of absorbance peak positions

between La₂O₂S and 1% Ln³⁺: La₂O₂S. The possible reason for this significant difference can be explained by the fact that there is absorption between 2p orbital of O⁻² and 4f orbital of Ln³⁺ [19,40].

For the optical band calculation, Tauc plot has been used, which is based on the relation [56]:

$$\alpha h\nu = K_1(h\nu - E_g)^n \quad (1)$$

Eq. (1) (the Tauc equation) gives the relation between absorption coefficient α and the optical energy band gap E_g . The graph plotted between $(\alpha h\nu)^{1/n} \rightarrow (h\nu)$ gives the band gap value. Here $n = 2$ is taken for the allowed indirect electronic transition. The estimated bandgap of pristine La₂O₂S is 4.96 eV and decreases for 1% Ln³⁺: La₂O₂S. The optical band gap is 3.73 eV for 1% Pr³⁺: La₂O₂S, 3.77 eV for 1% Eu³⁺: La₂O₂S, 3.83 eV for 1% Tb³⁺: La₂O₂S, 3.82 eV for 1% Dy³⁺: La₂O₂S, and 3.70 eV for 1% Er³⁺: La₂O₂S. The decrease in optical band gap values can be attributed to an overlapping of wave functions of electrons bounded to the Ln³⁺, causing formation of an energy band rather than discrete energy levels.

The refractive index η was calculated from the equation given by V. Kumar and J. K. Singh [57].

$$\eta = K E_g^C \quad (2)$$

where $K = 3.3668$ and $C = -0.32234$ are constants and E_g is the optical band gap.

The refractive index η is 2.00 for La₂O₂S and varies between 2.18 and 2.20 for 1% Ln³⁺: La₂O₂S samples.

The term molar extinction coefficient is a measure of how strongly a chemical substance absorbs light at a particular wavelength. It is an intrinsic property of a material that depends upon the composition and structure of a material. The molar extinction coefficient is calculated from the Beer–Lambert law, given by the equation

$$\epsilon = \frac{A}{LC} \quad (3)$$

Table 2
Structural data of 1%Ln³⁺: La₂O₂S extracted from the XRD spectra.

Materials	Phase Name	JCPDS no.	Avg. Crystallite Size (nm)	Volume (Å ³)
La ₂ O ₂ S	164:P-3m1	75–1930	31.9	97.28
Ln ³⁺ : La ₂ O ₂ S	164:P-3m1	75-1930, 75-1954, 27-0263, 71-2098	13.2, 19.5, 22.10, 18.2, 16.9, (Pr ³⁺ , Eu ³⁺ Tb ³⁺ , Dy ³⁺ , Er ³⁺)	84.33

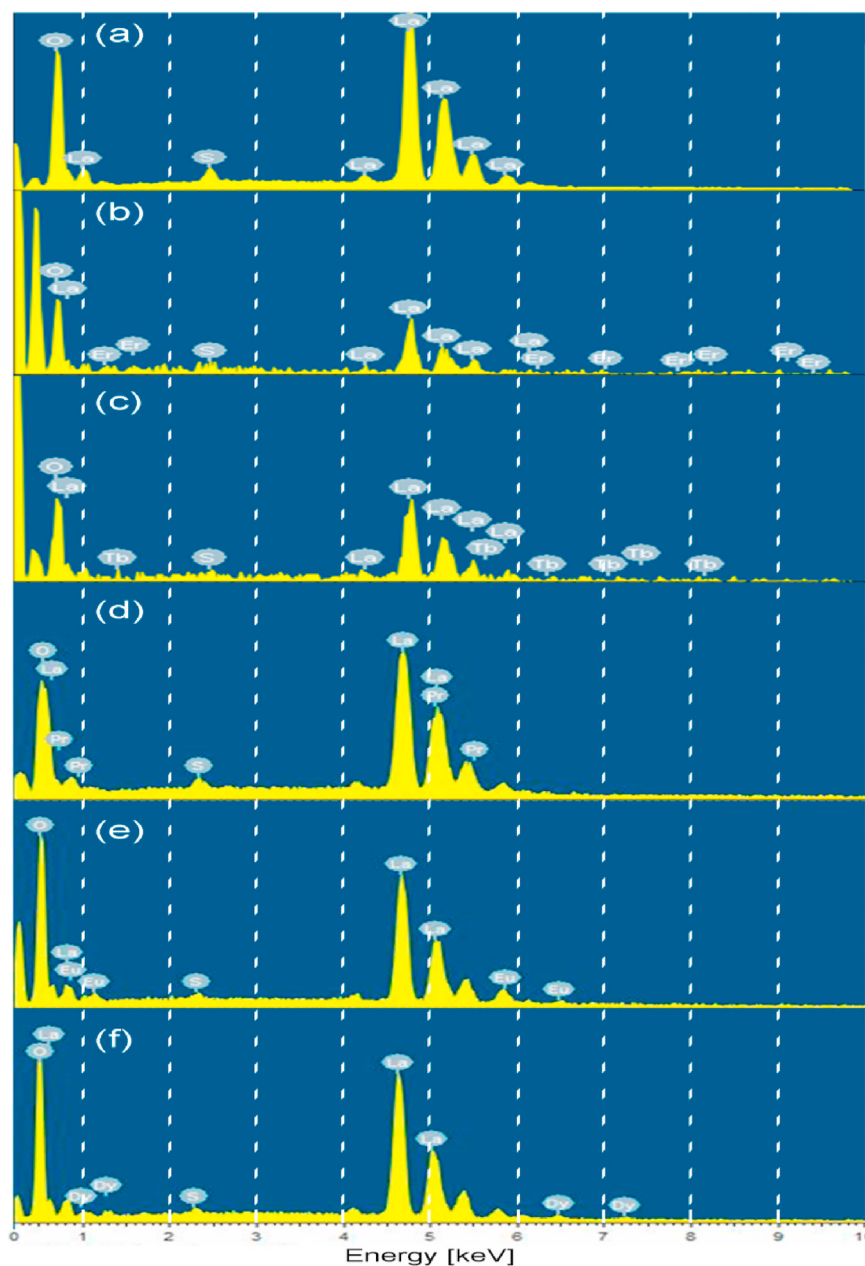


Fig. 3. EDAX spectrum of (a) $\text{La}_2\text{O}_2\text{S}$ (b) $1\%\text{Pr}^{3+}:\text{La}_2\text{O}_2\text{S}$ (c) $1\%\text{Eu}^{3+}:\text{La}_2\text{O}_2\text{S}$ (d) $1\%\text{Tb}^{3+}:\text{La}_2\text{O}_2\text{S}$ (e) $1\%\text{Dy}^{3+}:\text{La}_2\text{O}_2\text{S}$ (f) $1\%\text{Er}^{3+}:\text{La}_2\text{O}_2\text{S}$.

Table 3

EDAX data of $1\%\text{Ln}^{3+}:\text{La}_2\text{O}_2\text{S}$ from the spectrum with Atomic percentage.

Compound	Elements (Atomic %)							
	La	S	O	Pr	Eu	Tb	Dy	Er
$\text{La}_2\text{O}_2\text{S}:\text{Pr}^{3+}$	45.87	2.30	49.28	2.55	—	—	—	—
$\text{La}_2\text{O}_2\text{S}:\text{Eu}^{3+}$	40.36	1.19	55.17	—	3.28	—	—	—
$\text{La}_2\text{O}_2\text{S}:\text{Tb}^{3+}$	37.32	1.05	60.63	—	—	1.01	—	—
$\text{La}_2\text{O}_2\text{S}:\text{Dy}^{3+}$	44.54	1.35	52.04	—	—	—	2.08	—
$\text{La}_2\text{O}_2\text{S}:\text{Er}^{3+}$	34.32	3.27	61.96	—	—	—	—	0.34

Table 4

EDAX data of $1\%\text{Ln}^{3+}:\text{La}_2\text{O}_2\text{S}$ with a weight percentage.

Compound	Elements (Weight %)							
	La	S	O	Pr	Eu	Tb	Dy	Er
$\text{La}_2\text{O}_2\text{S}:\text{Pr}^{3+}$	83.91	0.97	10.39	4.73	—	—	—	—
$\text{La}_2\text{O}_2\text{S}:\text{Eu}^{3+}$	79.79	0.54	12.56	—	7.10	—	—	—
$\text{La}_2\text{O}_2\text{S}:\text{Tb}^{3+}$	81.67	0.53	15.28	—	—	2.52	—	—
$\text{La}_2\text{O}_2\text{S}:\text{Dy}^{3+}$	83.61	0.58	11.25	—	—	—	4.56	—
$\text{La}_2\text{O}_2\text{S}:\text{Er}^{3+}$	80.56	1.77	16.70	—	—	—	—	0.97

Here A is the amount of light absorbed by the sample for a particular wavelength. L is the distance which the light travels through the solution and C is the concentration of the absorbing species per unit volume.

3.3. Photoluminescence analysis

The Photoluminescence excitation and emission spectra were recorded on a Shimadzu make Spectrophotofluorometer.

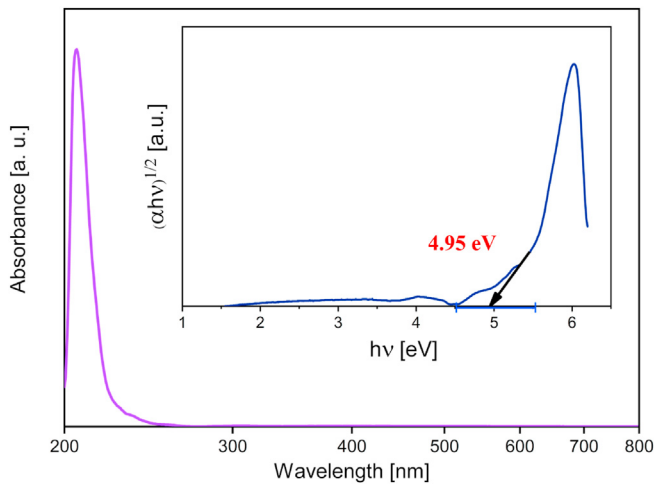


Fig. 4. UV-Visible and Tauc Plot of pristine $\text{La}_2\text{O}_2\text{S}$.

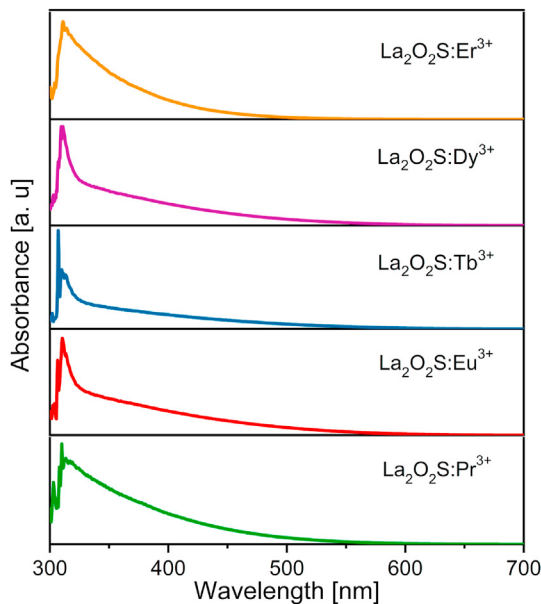


Fig. 5. UV-Visible graph of 1% Ln^{3+} : $\text{La}_2\text{O}_2\text{S}$.

Fig. 7a shows the spectra of Pr^{3+} : $\text{La}_2\text{O}_2\text{S}$. The $4f^2$ configuration of Pr^{3+} has 13 energy levels observed in absorption or fluorescence spectra or in both [61]. The excitation spectra was recorded at the emission wavelength $\lambda_{\text{emi}} = 500$ nm. The $4f5d$ transition in Pr^{3+} : $\text{La}_2\text{O}_2\text{S}$ was responsible for the excitation band with maximum at 282 nm [49,58,59]. The ground state of Pr^{3+} at $^3\text{H}_4$ and $^1\text{S}_0$ is the highest energy level at 48800 cm^{-1} . The $4f5d$ transitions were observed at approximately 35460 cm^{-1} , lower than the highest excitation energy level of Pr^{3+} . PL emission spectra were recorded at an excitation wavelength of $\lambda_{\text{exc}} = 282$ nm. The most intense and sharp peak is observed at 512 nm, and the second in intensity at 498 nm. The transition from energy level $^3\text{P}_0$ (20474.93 cm^{-1}) to ground energy level $^3\text{H}_4$ (0 cm^{-1}), $^3\text{P}_0 \rightarrow ^3\text{H}_4$ is responsible for peaks at 498 nm and at 512 nm [61]. The other two weak peaks at 541 nm and 554 nm are due to the transition $^3\text{P}_0$ (20474.93 cm^{-1}) $\rightarrow ^3\text{H}_5$ (2222 cm^{-1}).

From Fig. 7b of Eu^{3+} : $\text{La}_2\text{O}_2\text{S}$, PL excitation peak is observed at 283 nm by monitoring the emission $\lambda_{\text{emi}} = 580$ nm. The CT (charge transfer) transition is accountable for PL excitation spectra of Eu^{3+} :

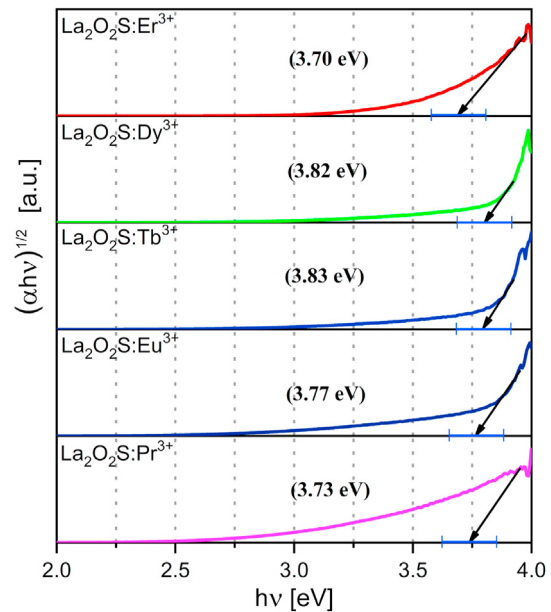


Fig. 6. Tauc plot of Ln^{3+} : $\text{La}_2\text{O}_2\text{S}$.

$\text{La}_2\text{O}_2\text{S}$ in which transition between $2p$ orbital of O^{2-} and $4f$ orbital of Eu^{3+} (which is at 35460 cm^{-1}) occurs [19,40]. The emission spectra is recorded by irradiation $\lambda_{\text{exc}} = 283$ nm. There are five emission peaks at 581 nm, 587 nm, 596 nm, 616 nm and 626 nm, due to $4f$ - $4f$ transitions. The transition $^5\text{D}_0$ (17267 cm^{-1}) $\rightarrow ^7\text{F}_0$ (0 cm^{-1} , ground level) was responsible for the emission at a wavelength of 581 nm; the peaks at 587 nm, and 596 nm due to $^5\text{D}_0 \rightarrow ^7\text{F}_1$ (355 cm^{-1}). The emission peaks at 616 nm and 626 nm are due the transition $^5\text{D}_0 \rightarrow ^7\text{F}_2$ (1022 cm^{-1}) [61].

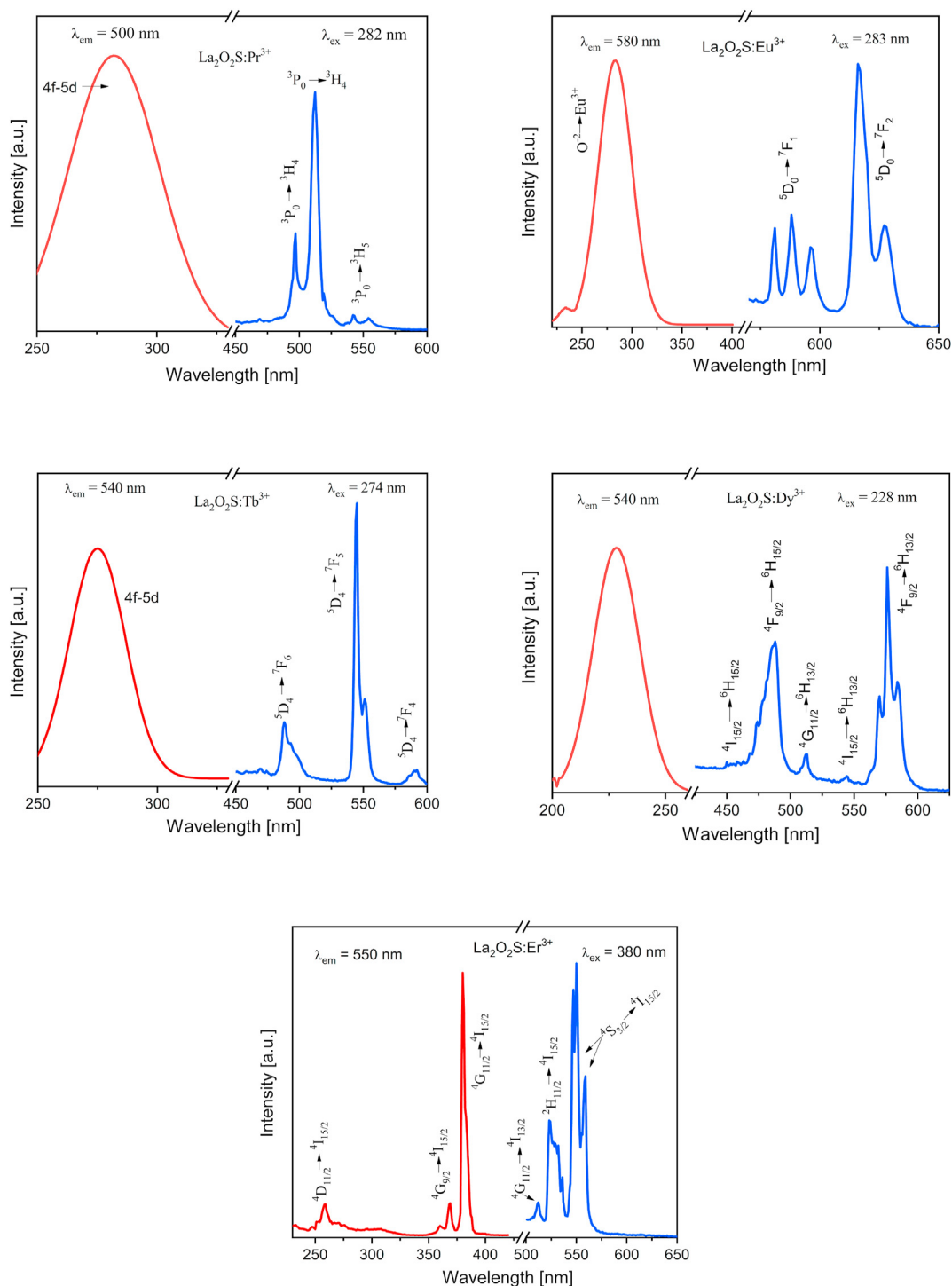
From Fig. 7c for the PL of Tb^{3+} : $\text{La}_2\text{O}_2\text{S}$, the maximum excitation was observed at a wavelength of 274 nm, by observing the emission at $\lambda_{\text{emi}} = 540$ nm. The $4f5d$ transition in Tb^{3+} : $\text{La}_2\text{O}_2\text{S}$ is accountable for the excitation spectra [35,49]. Under the excitation of 274 nm, three emission peaks were observed. The transition $^5\text{D}_4$ (20462.60 cm^{-1}) $\rightarrow ^7\text{F}_6$ (0 cm^{-1} , ground level) was responsible for emission peak at 487 nm. The transition $^5\text{D}_4 \rightarrow ^7\text{F}_5$ (2043.26 cm^{-1}) is responsible for a highest peak at 543 nm, and the peak at 590 nm is due to $^5\text{D}_4 \rightarrow ^7\text{F}_4$ (3266.42 cm^{-1}) [61].

In Fig. 7d of Dy^{3+} : $\text{La}_2\text{O}_2\text{S}$, the excitation was recorded at an emission wavelength of 540 nm. The excitation spectra has maximum at 228 nm. The host absorption is accountable for excitation in 1% Dy^{3+} : $\text{La}_2\text{O}_2\text{S}$ [58–60]. Under the excitation at 228 nm, six emission peaks appeared at 450 nm, 458 nm, 487 nm, 512 nm, 544 nm and 575 nm. The highest intensity peak is at 575 nm due to the $^4\text{F}_{9/2}$ (21097 cm^{-1}) $\rightarrow ^6\text{H}_{13/2}$ (3556 cm^{-1}) transition. The transition from $^4\text{I}_{15/2}$ (22247 cm^{-1}) $\rightarrow ^6\text{H}_{13/2}$ is responsible for the peak at a wavelength of 544 nm, which is less intense. The two weak peaks observed at 450 nm and 458 nm are due to the transition $^4\text{I}_{15/2} \rightarrow ^6\text{H}_{15/2}$ (0 cm^{-1} , ground level). The second most intense peak is spotted at 487 nm due to the transition $^4\text{F}_{9/2} \rightarrow ^6\text{H}_{15/2}$. The transition $^4\text{G}_{11/2}$ (23215 cm^{-1}) $\rightarrow ^6\text{H}_{13/2}$ is responsible for a peak at 512 nm [61].

Er^{3+} : $\text{La}_2\text{O}_2\text{S}$, PL excitation spectrum (Fig. 7e) was monitored at an emission wavelength of $\lambda_{\text{emi}} = 550$ nm. Three excitation peaks were recorded at 259 nm, 368 nm and 380 nm. Here the $4f$ - $4f$ transitions are responsible for the excitation spectra. Two weak excitation peaks are observed at 259 nm due to $^4\text{I}_{15/2}$ (0 cm^{-1} , ground energy level) $\rightarrow ^4\text{D}_{11/2}$ (39000 cm^{-1}) and at 368 nm due to $^4\text{I}_{15/2} \rightarrow ^4\text{G}_{9/2}$ (27412 cm^{-1}). The highest excitation peak is observed

Table 5UV/VIS data of host $\text{La}_2\text{O}_2\text{S}$ as well as $1\%\text{Ln}^{3+}:\text{La}_2\text{O}_2\text{S}$.

Compounds	λ_{max} (nm)	Band Gap (eV)	Refractive index η	ϵ_{λ} Molar decadic extinction coefficient $\text{mol}^{-1} \text{cm}^{-1}$
$\text{La}_2\text{O}_2\text{S}$	208	4.95	2.00	20
$\text{La}_2\text{O}_2\text{S}:\text{Pr}^{3+}$	311	3.73	2.20	21
$\text{La}_2\text{O}_2\text{S}:\text{Eu}^{3+}$	313	3.77	2.19	31
$\text{La}_2\text{O}_2\text{S}:\text{Tb}^{3+}$	307	3.83	2.18	32
$\text{La}_2\text{O}_2\text{S}:\text{Dy}^{3+}$	313	3.82	2.20	27
$\text{La}_2\text{O}_2\text{S}:\text{Er}^{3+}$	311	3.70	2.20	20

**Fig. 7.** (a): Emission and excitation graph of $1\%\text{Pr}^{3+}:\text{La}_2\text{O}_2\text{S}$. (b): Emission and excitation graph of $1\%\text{Eu}^{3+}:\text{La}_2\text{O}_2\text{S}$. (c): Emission and excitation graph of $1\%\text{Tb}^{3+}:\text{La}_2\text{O}_2\text{S}$. (d): Emission and excitation graph of $1\%\text{Dy}^{3+}:\text{La}_2\text{O}_2\text{S}$. (e): Emission and excitation graph of $1%\text{Er}^{3+}:\text{La}_2\text{O}_2\text{S}$.

at 380 nm due to the transition $4I_{15/2} \rightarrow 4G_{11/2}$ (26368 cm^{-1}) [60]. PL emission spectrum was recorded at the excitation wavelength of 380 nm. Four peaks were observed in the visible region. The first peak is observed at 512 nm due to the transition $4G_{11/2} \rightarrow 4I_{13/2}$ (6480 cm^{-1}). The second peak at 522 nm is due to the $2H_{11/2}$ (19087 cm^{-1}) $\rightarrow 4I_{15/2}$ transition. The third peak, which is the most intense peak observed at a wavelength of 550 nm and the fourth peak at 559 nm are due to the transition $4S_{13/2}$ (18353 cm^{-1}) $\rightarrow 4I_{15/2}$.

4. Conclusion

From the comparative study of structural data from the XRD spectra of three synthesis techniques for the preparation of Lanthanum oxysulfide, the furnace combustion technique was found to be the best technique. It has the potential to become an industrially friendly technique as it requires less time for synthesis, has minimum number of precursors and data from XRD suggests that a pure hexagonal phase can be synthesized by this technique. The five samples of $1\% \text{Ln}^{3+} : \text{La}_2\text{O}_2\text{S}$ synthesized by using the furnace combustion technique and matched with ICDD files confirmed the hexagonal lattice formation for all the samples. The undoped $\text{La}_2\text{O}_2\text{S}$ was found to have a bandgap of 4.96 eV which significantly decreased for the doped samples. From the study of PL excitation spectrum, it is suggested that 4f-5d transition was responsible for excitations of $1\% \text{Pr}^{3+} : \text{La}_2\text{O}_2\text{S}$ and $1\% \text{Tb}^{3+} : \text{La}_2\text{O}_2\text{S}$, while CT transition was accountable for excitation in $1\% \text{Eu}^{3+} : \text{La}_2\text{O}_2\text{S}$. The host absorption was responsible in $1\% \text{Dy}^{3+} : \text{La}_2\text{O}_2\text{S}$ and 4f-4f transition was accountable for excitation in $1\% \text{Er}^{3+} : \text{La}_2\text{O}_2\text{S}$. The PL emission of all $1\% \text{Ln}^{3+} : \text{La}_2\text{O}_2\text{S}$ were found to be highly intense and in the visible region. The emission of $1\% \text{Er}^{3+} : \text{La}_2\text{O}_2\text{S}$ was recorded for the first time in the visible range of the spectrum.

CRedit authorship contribution statement

Keval Shah: Conceptualization, Methodology, Investigation, Validation, Resources, Writing - original draft, Formal analysis, Visualization. **Aleksandar Ćirić:** Data curation, Visualization. **K.V.R. Murthy:** Resources, Writing - review & editing. **B.S. Chakrabarty:** Supervision, Writing - review & editing.

Declaration of competing interest

The authors declare that they have no known competing financial interests or personal relationships that could have appeared to influence the work reported in this paper.

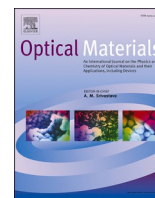
Appendix A. Supplementary data

Supplementary data to this article can be found online at <https://doi.org/10.1016/j.jallcom.2020.156725>.

References

- [1] G.H. Dieke, R.A. Satten, Spectra and energy levels of rare earth ions in crystals, *Am. J. Phys.* (1970), <https://doi.org/10.1119/1.1976350>.
- [2] A.R. Jha, Rare Earth Materials: Properties and Applications, 2014, <https://doi.org/10.1201/b17045>.
- [3] M. Ikram, S. Ali, M. Aqeel, A. Ul-Hamid, M. Imran, J. Haider, A. Haider, A. Shahbaz, S. Ali, Reduced graphene oxide nanosheets doped by Cu with highly efficient visible light photocatalytic behavior, *J. Alloys Compd.* (2020), <https://doi.org/10.1016/j.jallcom.2020.155588>.
- [4] A. Raza, M. Ikram, M. Aqeel, M. Imran, A. Ul-Hamid, K.N. Riaz, S. Ali, Enhanced industrial dye degradation using Co doped in chemically exfoliated MoS₂ nanosheets, *Appl. Nanosci.* (2020), <https://doi.org/10.1007/s13204-019-01239-3>.
- [5] J. Hassan, M. Ikram, A. Ul-Hamid, M. Imran, M. Aqeel, S. Ali, Application of chemically exfoliated boron nitride nanosheets doped with Co to remove organic pollutants rapidly from textile water, *Nanoscale Res. Lett.* (2020), <https://doi.org/10.1186/s11671-020-03315-y>.
- [6] The rare earth elements: an introduction, *Choice Rev. Online.* (2016), <https://doi.org/10.5860/choice.196797>.
- [7] T. Wu, J. Zhou, B. Wu, W. Li, Effect of La₂O₃ content on wear resistance of alumina ceramics, *J. Rare Earths* (2016), [https://doi.org/10.1016/S1002-0721\(16\)60027-3](https://doi.org/10.1016/S1002-0721(16)60027-3).
- [8] W. Wu, F. Zhang, X. Bian, S. Xue, S. Yin, Q. Zheng, Effect of loaded organic phase containing mixtures of silicon and aluminum, single iron on extraction of lanthanum in saponification P507-HCl system, *J. Rare Earths* (2013), [https://doi.org/10.1016/S1002-0721\(12\)60348-2](https://doi.org/10.1016/S1002-0721(12)60348-2).
- [9] C.H. Yan, Z.G. Yan, Y.P. Du, J. Shen, C. Zhang, W. Feng, Controlled Synthesis and Properties of Rare Earth Nanomaterials, 2011, <https://doi.org/10.1016/B978-0-444-53590-0.00004-2>.
- [10] J. Shen, L.D. Sun, C.H. Yan, Luminescent rare earth nanomaterials for bioprobes applications, *Dalton Trans.* (2008), <https://doi.org/10.1039/b805306e>.
- [11] G.C. Righini, M. Ferrari, Photoluminescence of rare-earth-doped glasses, *Riv. Del Nuovo Cim.* (2005), <https://doi.org/10.1393/ncr/i2006-10010-8>.
- [12] A. Kitai, Luminescent Materials and Applications, 2008, <https://doi.org/10.1002/9780470985687>.
- [13] L.E. Sobon, K.A. Wickersheim, R.A. Buchanan, R.V. Alves, Growth and properties of lanthanum oxysulfide crystals, *J. Appl. Phys.* (1971), <https://doi.org/10.1063/1.1660682>.
- [14] C.W. Struck, W.H. Fonger, Dissociation of Eu+3 charge-transfer state in Y₂O₃ and La₂O₃ into Eu+2 and a free hole, *Phys. Rev. B* (1971), <https://doi.org/10.1103/PhysRevB.4.22>.
- [15] R. Vali, Electronic, dynamical, and dielectric properties of lanthanum oxysulfide, *Comput. Mater. Sci.* (2006), <https://doi.org/10.1016/j.commatsci.2005.08.007>.
- [16] C. Koepke, A.J. Wojtowicz, A. Lempicki, Excited-state absorption in excimer-pumped CaWO₄ crystals, *J. Lumin.* (1993), [https://doi.org/10.1016/0022-2313\(93\)90003-6](https://doi.org/10.1016/0022-2313(93)90003-6).
- [17] C. Li, H. Wang, B. Bai, L. Zhang, Thermodynamic analysis of precipitation of La-O-S-as inclusions in steel, in: *Miner. Met. Mater. Ser.*, 2019, https://doi.org/10.1007/978-3-030-05955-2_75.
- [18] Y. Hou, G. Xiong, L. Liu, G. Li, N. Moelans, M. Guo, Effects of LaAlO₃ and La₂O₃ inclusions on the initialization of localized corrosion of pipeline steels in NaCl solution, *Scripta Mater.* (2020), <https://doi.org/10.1016/j.scriptamat.2019.10.025>.
- [19] S. Imashuku, K. Wagatsuma, Cathodoluminescence analysis of nonmetallic inclusions in steel deoxidized and desulfurized by rare-earth metals (La, Ce, Nd), *Metall. Mater. Trans. B Process Metall. Mater. Process. Sci.* (2020), <https://doi.org/10.1007/s11663-019-01732-8>.
- [20] S. Tan, D. Li, Enhancing oxygen storage capability and catalytic activity of lanthanum oxysulfide (La₂O₃S) nanocatalysts by sodium and iron/sodium doping, *ChemCatChem* (2018), <https://doi.org/10.1002/cctc.201701117>.
- [21] J.A. Bagilo, Lanthanum oxysulfide as a catalyst for the oxidation of CO and COS by SO₂, *Ind. Eng. Chem. Prod. Res. Dev.* (1982), <https://doi.org/10.1021/i300005a007>.
- [22] I. Iparraguirre, J. Azkargorta, O. Merdignac-Conanec, M. Al-Saleh, C. Chlique, X. Zhang, R. Balda, J. Fernández, Laser action in Nd³⁺-doped lanthanum oxysulfide powders, *Optic Express* (2012), <https://doi.org/10.1364/oe.20.023690>.
- [23] C. Freiburg, W. Krumpfen, U. Troppenz, Determinations of Ce, Eu and Tb in the electroluminescent materials Gd₂O₃S and La₂O₃S by total-reflection X-ray spectrometry, *Spectrochim. Acta Part B At. Spectrosc.* (1993), [https://doi.org/10.1016/0584-8547\(93\)80032-P](https://doi.org/10.1016/0584-8547(93)80032-P).
- [24] W.I. Dobrov, R.A. Buchanan, Photoconductivity and luminescence in lanthanum oxysulfide, *Appl. Phys. Lett.* (1972), <https://doi.org/10.1063/1.1654343>.
- [25] B.M. Jaffar, H.C. Swart, H.A.A. Seed Ahmed, A. Yousif, R.E. Kroon, Cathodoluminescence degradation of Bi doped La₂O₃ and La₂O₃S phosphor powders, *Phys. B Condens. Matter* (2019), <https://doi.org/10.1016/j.physb.2019.411659>.
- [26] L.J.B. Erasmus, H.C. Swart, J.J. Terblans, La₂O₃S:Eu³⁺ stability as temperature sensor, *Appl. Surf. Sci.* (2019), <https://doi.org/10.1016/j.apsusc.2019.05.075>.
- [27] G. Jiang, X. Wei, Y. Chen, C. Duan, M. Yin, B. Yang, W. Cao, Luminescent La₂O₃S:Eu³⁺ nanoparticles as non-contact optical temperature sensor in physiological temperature range, *Mater. Lett.* (2015), <https://doi.org/10.1016/j.matlet.2014.12.057>.
- [28] Y. Yan, X. Zhang, H. Li, Y. Ma, T. Xie, Z. Qin, S. Liu, W. Sun, E. Lewis, An optical fiber sensor based on La₂O₃S:Eu scintillator for detecting ultraviolet radiation in real-time, *Sensors* (2018), <https://doi.org/10.3390/s18113754>.
- [29] S.V. Yap, R.M. Ranson, W.M. Cranton, D. Koutsogeorgis, Decay time characteristics of La₂O₃S:Eu and La₂O₃S:Tb for use within an optical sensor for human skin temperature measurement, *Appl. Opt.* (2008), <https://doi.org/10.1364/AO.47.004895>.
- [30] I. Kandarakis, D. Cavouras, Experimental and theoretical assessment of the performance of Gd₂O₃S:Tb and La₂O₃S:Tb phosphors and Gd₂O₃S:Tb-La₂O₃S:Tb mixtures for X-ray imaging, *Eur. Radiol.* (2001), <https://doi.org/10.1007/s003300000715>.
- [31] R. Ward, J.J. Pitha, A.L. Smith, The preparation of lanthanum oxysulfide and its properties as a base material for phosphors stimulated by Infrared 1, *J. Am. Chem. Soc.* (1947), <https://doi.org/10.1021/ja01200a009>.
- [32] H. Ratinen, X-ray-excited optical fluorescence of ten rare earth ions in Y₂O₃S,

- La2O2S, and Gd2O2S, Phys. Status Solidi (1972), <https://doi.org/10.1002/pssa.2210120211>.
- [33] K. Rajamohan Reddy, K. Annapurna, N. Sooraj Hussain, S. Buddhudu, Fluorescence spectra of Tb³⁺: Ln₂O₂S powder phosphors, Spectrosc. Lett. (1997).
- [34] K.C. Bleijenberg, F.A. Kellendonk, C.W. Struck, Two-photon excited luminescence of thulium-activated lanthanum oxysulfide (La2O2S-Tm³⁺), J. Chem. Phys. (1980), <https://doi.org/10.1063/1.440583>.
- [35] K. Rajamohan Reddy, K. Annapurna, S. Buddhudu, Fluorescence spectra of Eu³⁺:Ln2O2S (Ln = Y, La, Gd) powder phosphors, Mater. Res. Bull. (1996), [https://doi.org/10.1016/0025-5408\(96\)00129-8](https://doi.org/10.1016/0025-5408(96)00129-8).
- [36] Y. Kitazawa, Y. Kunimoto, M. Wakihara, M. Taniguchi, Phase equilibria and oxidation mechanisms in the La-S-O system, J. Therm. Anal. (1982), <https://doi.org/10.1007/BF01912953>.
- [37] K. Ikeue, T. Kawano, M. Eto, D. Zhang, M. Machida, X-ray structural study on the different redox behavior of La and Pr oxysulfates/oxysulfides, J. Alloys Compd. (2008), <https://doi.org/10.1016/j.jallcom.2007.04.145>.
- [38] E.I. Sal'nikova, D.I. Kaliev, P.O. Andreev, Kinetics of phase formation upon the treatment of La₂(SO₄)₃ and La₂O₂SO₄ in a hydrogen flow, Russ. J. Phys. Chem. (2011), <https://doi.org/10.1134/S0036024411120296>.
- [39] S. Buddhudu, F.J. Bryant, Optical transitions of erbium(3+):lanthanum oxide sulfide (La2O2S) and erbium(3+):yttrium oxide sulfide (Y2O2S), J. Less Common. Met. (1989), [https://doi.org/10.1016/0022-5088\(89\)90195-1](https://doi.org/10.1016/0022-5088(89)90195-1).
- [40] J. Ma, M. Fang, N.T. Lau, On the synergism between La2O2S and CoS2 in the reduction of SO2 to elemental sulfur by CO, J. Catal. (1996), <https://doi.org/10.1006/jcat.1996.0024>.
- [41] R.H. Krauss, R.G. Hellier, J.C. McDaniel, Surface temperature imaging below 300 K using La₂O₂S:Eu, Appl. Optic. (1994), <https://doi.org/10.1364/ao.33.003901>.
- [42] H. Peng, S. Huang, F. You, J. Chang, S. Lu, Lin Cao, Preparation and surface effect analysis of trivalent europium-doped nanocrystalline La2O2S, J. Phys. Chem. B (2005), <https://doi.org/10.1021/jp0453414>.
- [43] T. Xia, W.H. Cao, X.X. Luo, Y. Tian, Combustion synthesis and spectra characteristic of Gd2O2S: Tb³⁺ and La2O2S: Eu³⁺ x-ray phosphors, J. Mater. Res. (2005), <https://doi.org/10.1557/JMR.2005.0301>.
- [44] X. xian Luo, W. he Cao, Ethanol-assistant solution combustion method to prepare La2O2S:Yb,Pr nanometer phosphor, J. Alloys Compd. (2008), <https://doi.org/10.1016/j.jallcom.2007.06.011>.
- [45] D. Qilin, S. Hongwei, W. Meiyuan, B. Xue, D. Biao, Q. Ruifei, Q. Xuesong, Z. Hui, Size and concentration effects on the photoluminescence of La 2O2S:Eu³⁺ nanocrystals, J. Phys. Chem. C (2008), <https://doi.org/10.1021/jp808343f>.
- [46] Z. Liu, X. Sun, S. Xu, J. Lian, X. Li, Z. Xiu, Q. Li, D. Huo, J.G. Li, Tb³⁺ and Eu³⁺ doped lanthanum oxysulfide nanocrystals. Gelatin-templated synthesis and luminescence properties? J. Phys. Chem. C (2008) <https://doi.org/10.1021/jp0764687>.
- [47] J. Lian, B. Wang, P. Liang, F. Liu, X. Wang, Fabrication and luminescent properties of La2O 2S:Eu³⁺ translucent ceramic by pressureless reaction sintering, Opt. Mater. (2014), <https://doi.org/10.1016/j.optmat.2014.01.024>.
- [48] L. Yu, F. Li, H. Liu, Fabrication and photoluminescent characteristics of one-dimensional La 2O2S:Eu³⁺ nanocrystals, J. Rare Earths (2013), [https://doi.org/10.1016/S1002-0721\(12\)60285-3](https://doi.org/10.1016/S1002-0721(12)60285-3).
- [49] X. Wang, J.G. Li, M.S. Molokeev, Q. Zhu, X. Li, X. Sun, Layered hydroxyl sulfate: controlled crystallization, structure analysis, and green derivation of multi-color luminescent (La,RE)2O2SO4 and (La,RE)2O2S phosphors (RE = Pr, Sm, Eu, Tb, and Dy), Chem. Eng. J. (2016), <https://doi.org/10.1016/j.cej.2016.05.089>.
- [50] M. Pokhrel, A.K. Gangadharan, D.K. Sardar, High upconversion quantum yield at low pump threshold in Er 3+/Yb3+ doped La2O2S phosphor, Mater. Lett. (2013), <https://doi.org/10.1016/j.matlet.2013.02.062>.
- [51] D. Ma, S. Liu, Y. Zhang, C. Zhang, S. Huang, Controlled synthesis of Eu³⁺-doped La2O2S nanophosphors by refluxing method, J. Exp. Nanosci. (2013), <https://doi.org/10.1080/17458080.2011.591002>.
- [52] Q. Pan, D. Yang, S. Kang, J. Qiu, G. Dong, Regulating mid-infrared to visible fluorescence in monodispersed Er³⁺-doped La2O2S (La2O2SO4) nanocrystals by phase modulation, Sci. Rep. (2016), <https://doi.org/10.1038/srep37141>.
- [53] S.W. Kim, T. Hasegawa, T. Abe, H. Nakagawa, S. Hasegawa, K. Seki, K. Toda, K. Uematsu, T. Ishigaki, M. Sato, Abnormal improvement in emission of lanthanum oxysulfide phosphor La2O2S:Tb³⁺ synthesized by a novel method, thermal decomposition in eutectic molten salt, Ceram. Int. (2016), <https://doi.org/10.1016/j.ceramint.2016.03.176>.
- [54] L. Wang, X. Yang, Q. Zhang, B. Song, C. Wong, Luminescence properties of La2O2S:Tb³⁺ phosphors and phosphor-embedded polymethylmethacrylate films, Mater. Des. (2017), <https://doi.org/10.1016/j.matdes.2017.04.003>.
- [55] J. Fernández, R. Balda, M. Barredo-Zuriarrain, O. Merdrignac-Conanec, N. Hakmeh, S. García-Revilla, M.A. Arriandiaga, Spectroscopic and thermal study of Er-doped oxysulfide crystal powders, Laser Refrig. Solids VIII (2015), <https://doi.org/10.1117/12.2076963>.
- [56] J. Tauc, R. Grigorovici, A. Vancu, Optical properties and electronic structure of amorphous germanium, Phys. Status Solidi (1966), <https://doi.org/10.1002/pssb.19660150224>.
- [57] V. Kumar, J.K. Singh, Model for calculating the refractive index of different materials, Indian J. Pure Appl. Phys. (2010).
- [58] C. Gorller-Walrand, K. Binnemans, Spectral intensities of f-f transitions.pdf, Handb. Phys. Chem. Rare Earths 25 (1998).
- [59] Adv. Spec. Laser. Sen. (2006), <https://doi.org/10.1007/1-4020-4789-4>.
- [60] W.T. Carnall, G.L. Goodman, K. Rajnak, R.S. Rana, A systematic analysis of the spectra of the lanthanides doped into single crystal LaF₃, J. Chem. Phys. (1989), <https://doi.org/10.1063/1.455853>.
- [61] G.H. Dieke, H. Crosswhite, Spectra and energy levels of rare earth ions in crystals 13 (1968). Che, Interscience Publishers.



Research Article

Upconversion photoluminescence of sub-micron lanthanum oxysulfide particles co-doped with $\text{Yb}^{3+}/\text{Ho}^{3+}$ and $\text{Yb}^{3+}/\text{Tm}^{3+}$ synthesized by optimized combustion technique

Aleksandar Ćirić^{a,*}, Milica Sekulić^a, Kevil Shah^b, Bishwajit S. Chakrabarty^b, Miroslav D. Dramićanin^a

^a Vinča Institute of Nuclear Sciences – National Institute of the Republic of Serbia, University of Belgrade, Belgrade, Serbia

^b Applied Physics Department, Faculty of Technology & Engineering, The Maharaja Sayajirao University of Baroda, Vadodara, Gujarat, India



ARTICLE INFO

Keywords:

Sub-micron particles
Upconversion
 Yb^{3+}
 Ho^{3+}
 Tm^{3+}
Solution combustion

ABSTRACT

Upconversion sub-micron particles are one of the most perspective materials due to their wide application range, the most important being in the bio-medicinal field where they can be used for labeling, sensing, treatment or drug delivery. Chemically stable upconversion sub-micron particles of $\text{La}_2\text{O}_2\text{S}$ co-doped with $\text{Yb}^{3+}/\text{Ho}^{3+}$ and $\text{Yb}^{3+}/\text{Tm}^{3+}$ were synthesized and characterized. Different concentrations of $\text{Yb}^{3+}/\text{Ho}^{3+}$ and $\text{Yb}^{3+}/\text{Tm}^{3+}$ were successfully incorporated into the hexagonal crystal structure of lanthanum oxysulfide using the optimized solution combustion synthesis method with urea as a fuel. Sub-micron particles of less than 50 nm in diameter showed the typical upconversion photoluminescence when excited by 980 nm laser. The highest PL intensities were obtained in $\text{La}_2\text{O}_2\text{S}$ co-doped with 8 wt% Yb and 1.5 wt% Ho, or in case of $\text{La}_2\text{O}_2\text{S}:\text{Yb}^{3+}/\text{Tm}^{3+}$ with 4 wt% Yb and 0.5 wt% Tm.

The CIE 1976 chromaticity coordinates of Ho^{3+} photoluminescence emission are (0.119, 0.581), with color purity of 98.7 %. The chromaticity of upconversion emission was invariant to doping concentrations.

1. Introduction

The main feature of upconversion materials is the absorption of low energy photons with the resulting emission of higher energy photons. Although the upconversion materials have many applications, e.g. by enhancing the solar cell efficiency [1], due to the fact that the excitation often lies within the biological transparency windows [2] they have found their way into multiple biological and medicinal usages, given that the particle size is adequately small to cause no unwanted disturbance to the living cells. The sub-micron particles have received considerable attention in recent years, due to their broad range of potential applications: as thermometers [3–5], for biological labeling and imaging [6], cancer treatment or drug delivery and therapy [7,8].

In order to be applicable in the sensitive bio-medicinal field, the sub-micron particles must possess several properties, out of which the most crucial are: (i) the low cytotoxicity, (ii) emission or excitation in the biologically transparent windows, (iii) high efficiency. Cytotoxicity is possibly the most important criteria in the selection of sub-micron particles for bio-medicinal applications, and it is the main advantage of sub-

micron particles over the heavy metal quantum dots [6]. The biological transparency of emission and excitation is extremely important in order for the excitation light to deeply penetrate into the tissue and for ensuring adequate detection. The three biological transparency windows lie in ranges of 650–950 nm, 1000–1350 nm, and 1550–1850 nm [2]. The most famous are the Yb^{3+} co-doped sub-micron particles due to the efficient Yb^{3+} absorption [9] in the first biological window (see Fig4 in Ref. [10]). Er^{3+} , Ho^{3+} , and Tm^{3+} have the $^{2S+1}L_J$ levels of the 4f configurations at energies that are very close to the energy of the $^2F_{5/2}$ excited level of Yb^{3+} . Thus, the sensitization of these trivalent lanthanides is very efficient by the energy transfer upconversion process (ETU) [11], with the subsequent emission from the co-doped pair. Ho^{3+} and Tm^{3+} have strong emissions in the first biological window, thus the $\text{Yb}^{3+}/\text{Ho}^{3+}$ and $\text{Yb}^{3+}/\text{Tm}^{3+}$ co-doped sub-micron particles are excellent materials for biological and medicinal applications. Also, they are promising probes for luminescence thermometry applications [12]. As the upconversion mechanism inherently has a low efficiency [13], it is crucial for the host matrix to have low phonon energy and to minimize the non-radiative depopulation of the emitting levels [14]. Fluorides are

* Corresponding author.

E-mail address: aleksandar.ciric@ff.bg.ac.rs (A. Ćirić).

recognized as the most efficient sub-micron hosts [3,15], however, their low chemical stability and cytotoxicity greatly limit their usage *in vivo* and for large scale industrial applications [16]. Alternately, the stable oxide materials can be used, but due to the higher phonon energy $>500\text{ cm}^{-1}$, the efficiency of the sub-micron particles can be lower. In contrast, the oxysulfides (IUPAC name: oxysulfide) pertain to the chemical stability of the oxides while having the phonon energy in between the two mentioned hosts (around 500 cm^{-1}) due to the incorporation of sulfide as ligand instead of oxide. Thus, they are promising sub-micron particles with the low cytotoxicity and high upconversion efficiency that is comparable to the efficiency of fluorides and can be several times higher than in oxides [16,17]. Furthermore, unlike fluorides, they can be easily mass-produced at low costs [18].

Solid-state synthesis method was developed 70 years ago and has been used for the synthesis of almost all phosphors [16,19–22], and has been used for synthesis of microcrystalline oxysulfides with high purity [23–25].

For the synthesis of the $\text{R}_2\text{O}_2\text{S}$ materials, the use of the solvent-thermal pressure relief with a flux agent in the lower atmosphere is very common. The high temperature and duration of these two techniques are key hurdles to wide application in research and industry.

Combustion synthesis is based on a self-propagating, exothermic reaction in an aqueous solution of organic salts combined with a fuel [26–28]. The most commonly used fuels employed for combustion synthesis are urea ($\text{CO}(\text{NH}_2)_2$), glycine ($\text{C}_2\text{H}_5\text{NO}_2$), β -Alanine ($\text{C}_3\text{H}_7\text{NO}_2$), glycerol ($\text{C}_3\text{H}_8\text{O}_3$), oxalyl dihydrazide ($\text{C}_2\text{H}_6\text{N}_4\text{O}_2$), citric acid ($\text{C}_6\text{H}_8\text{O}_7$) and many others. As reactive molecules are self-propagated, the combustion reaction begins and this reaction then includes the entire solution. The reaction temperature exceeds high values for a very short period while massive quantities of gases are released and these gases affect the growth of crystallites and reduce agglomerates, encouraging the production of a very porous structure [29,30].

This synthesis provides various benefits, such as the modification of the microstructure of the particles and the yield output of new materials using no or little harmful chemicals. K. Shah et al. [31] suggested a series of methods for the preparation of $\text{La}_2\text{O}_2\text{S}$ and the combustion method is being selected with the aim of obtaining the pure crystal phase without losing the beneficial optical properties. In this work urea ($\text{CO}(\text{NH}_2)_2$) and thiourea ($\text{SC}(\text{NH}_2)_2$) were used as fuel and source of sulfur in order to prevent the use of harmful gases, such as H_2S and CS_2 , during the reaction.

Taking all the merits into consideration, it is surprising that there are only scarce reports on the synthesis and upconversion of the $\text{Yb}^{3+}/\text{Tm}^{3+}$ and $\text{Yb}^{3+}/\text{Ho}^{3+}$ $\text{La}_2\text{O}_2\text{S}$ sub-micron particles [32,33]. This paper aims to fill that gap by applying the recently introduced optimized combustion technique for their synthesis, directly targeting the industry that is capable of mass-production primarily for biological and medicinal applications. For this purpose, the morphology, structure, and photoluminescent properties of microcrystalline $\text{La}_2\text{O}_2\text{S}:\text{Yb}^{3+}/\text{Tm}^{3+}$ or $\text{La}_2\text{O}_2\text{S}:\text{Yb}^{3+}/\text{Ho}^{3+}$ sub-micron particles are investigated.

2. Experimental

Lanthanum oxysulfide co-doped with Yb/Ho and Yb/Tm were synthesized by optimized combustion method at $490\text{ }^\circ\text{C}$. Nitrate hexahydrates (99.9 % purity from Xinyu advanced materials limited) were used as sources of lanthanide ions (La, Yb, Ho, and Tm). Firstly, urea was dissolved in a mixture of distilled water and ethanol, and the solution was added to the stoichiometric mixture of lanthanide nitrates and thiourea. Once the solution has been homogenized, it is moved to the aluminum crucible and heated in the furnace at $490\text{ }^\circ\text{C}$. The reaction began immediately and within 20 min the gasses were released, and the voluminous powder was formed.

The structure of the samples is checked by Rigaku SmartLab Diffractometer using X-ray diffraction operating with Cu K radiation (30

mA, 40 kV, 2θ range from 10 to 90° , step 0.02°). The scanning electron microscope (Mira 3 Tescan; 20 keV, magnifications of 10,000, 50,000, and 100,000) was used for the microstructural study. Energy dispersive X-ray spectroscopy (EDS) was performed by the Jeol JSM 5800 SEM equipped with Oxford Inca 3.2 EDS. Solid-state laser 980 nm (150 mW, MDLH 980 3 W, high-stability, fluctuations below 1 %) was used for the excitation of upconversion emission, and emission spectra were collected through the bifurcated optical fiber connected to spectrophotometer FHR 1000 equipped with the ICCD detector (Horiba Jobin-Yvon). All samples were recorded under the same experimental conditions.

3. Results and discussion

XRD patterns (Fig. 1) correspond to the hexagonal phase of lanthanum oxysulfide ($\text{P}\bar{3}\text{m}1$ symmetry, ICDD 01-75-1930 card) with an average crystallite size of about 225 \AA (22.5 nm ; calculated with Scherrer's equation as average from peaks at 25.6° , 28.6° , 36.5° and 45.0°). The partial substitution of La ions by Yb, Ho, and Tm dopants did not alter the crystal structure of $\text{La}_2\text{O}_2\text{S}$. In this structure, La^{3+} is coordinated by seven ions, four oxygen and three sulfur ions [19]. The crystal structure consists of alternative stacking layers, a positive charged (La_2O_2) $^{2+}$ layer and a layer of sulfide S^{2-} groups [34]. These layers provide large lattice constants which is beneficial for doping without concentration quenching of emission. The agglomerated particles were also present in other $\text{La}_2\text{O}_2\text{S}$ synthesized by the combustion method, with similar size of crystallites. For example, $\text{La}_2\text{O}_2\text{S}:\text{Yb}^{3+}/\text{Pr}^{3+}$ created by ethanol and thioacetamide fuels resulted in $25\text{--}40\text{ nm}$ [35], while $\text{La}_2\text{O}_2\text{S}:\text{Bi}$ by thioacetamide fuel in 27 nm crystallites [36].

Fig. 2. Presents the SEM images, where the micrographs show the usual agglomerate of sub-micron particles produced during combustion synthesis, but there are still sufficiently visible round shaped particles. Detailed analysis was performed using ImageJ software on SEM image with magnification 100,000 times and as seen in Fig. 2d on the histogram the average particle size is 44.5 nm . EDS analysis revealed that codopants were incorporated in concentrations as given in Fig. 3. EDS spectra are given in the supporting material in Fig. S1.

Fig. 3 displays the upconversion photoluminescence emission spectra under 980 nm excitation and the corresponding analysis. Fig. 3a presents the concentration-dependent spectra of $\text{La}_2\text{O}_2\text{S}:\text{Yb}^{3+}/\text{Ho}^{3+}$ (note that the ordinate is given on a logarithmic scale). The highest PL intensity was observed in the sample doped with 8 wt% of Yb^{3+} and 1.5 wt% of Ho^{3+} . The major peak (green emission) originates from the electron transitions between closely spaced $^5\text{F}_4$ and $^5\text{S}_2$ levels and the $^5\text{I}_8$

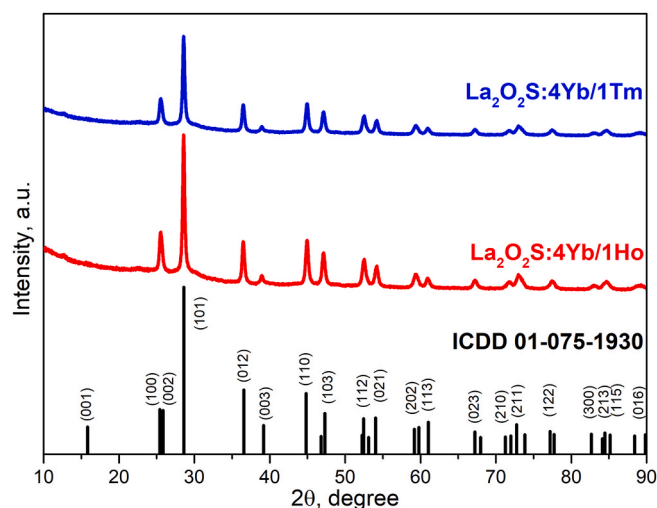


Fig. 1. XRD of $\text{La}_2\text{O}_2\text{S}:\text{4\%Yb/1\%Tm}$ (blue line) and $\text{La}_2\text{O}_2\text{S}:\text{4\%Yb/1\%Ho}$ (red line) compared to ICDD 01-075-1930 with characteristic planes.

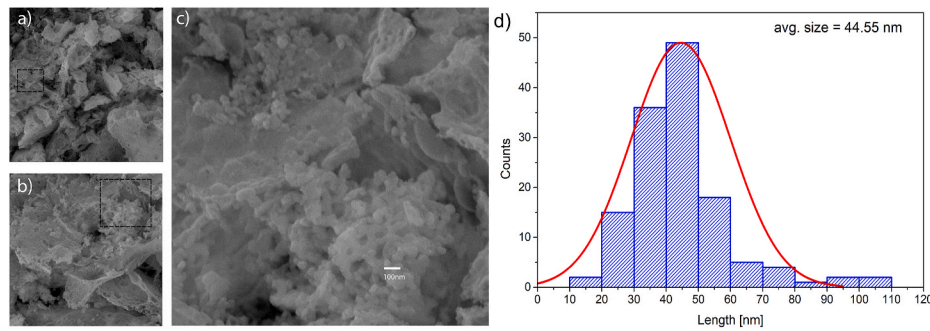


Fig. 2. SEM images of La₂O₂S:Yb³⁺/Ho³⁺ with magnification of a) 10,000, b) 50,000 and c) 100,000 (magnified regions are selected). D) Particle size histogram.

ground level. The slightly weaker emission (red emission centered at 667 nm) is attributed to ⁵F₅→⁵I₈ transition, and the emission of the lowest intensity is located around 760 nm and is due ⁵S₂→⁵I₇ transition.

PL spectra of the Tm³⁺ co-doped samples are given in Fig. 3b. The emissions are due to the ¹G₄→³F₄, ³F_{2,3}→³H₆, and ³H₄→³H₆ transitions at 654 nm, 669 nm + 694 nm, and 799 nm, respectively [37]. In Fig. 3b, the emission intensity is presented in a logarithmic scale; thus, the later transition truly dominates in the emission spectra. Contrary to co-doping with Ho³⁺, the highest emission intensity was observed with the lowest concentration of Yb³⁺ and the highest concentration of Tm³⁺. The samples co-doped with 15 wt% and 8 wt% of Yb³⁺ presented no significant change in the intensity of dominant peaks, but the 654 nm emission experienced significant quenching with the former Yb doping concentration. The integrated upconversion emission intensities of Ho³⁺ and Tm³⁺ co-doped samples of different doping concentrations are compared in Fig. 3c, showing that Tm³⁺ produced significantly higher emission yield.

It is well-known that Ho³⁺ and Tm³⁺, unlike Er³⁺, do not have energy levels that match the 980 nm [38], thus, these ions cannot be excited unless they are in the vicinity of the Yb³⁺ ions [39]. The Yb³⁺ has a large absorption cross-section at this wavelength, resulting in the ²F_{7/2}→²F_{5/2} excitation [40]. After the rapid de-excitation to the lowest Stark sublevel of the ²F_{5/2} level, the Yb³⁺ can either emit NIR photon or transfer energy to the Ho³⁺ or Tm³⁺. As the acceptor levels ⁵I₆ and ³H₅ of Ho³⁺ and Tm³⁺, respectively, are lower in energy than the ²F_{5/2} of Yb³⁺, the energy transfer process is phonon-assisted (Fig. 3e) [9]. In the case of Ho³⁺, the ⁵I₆ level may experience another energy transfer upconversion (ETU) to ⁵F₄, or de-excite to ⁵I₇ and then experience the second ETU to ⁵F₅ [41]. After multiphonon de-excitation from ³H₅ to ³F₄, the Tm³⁺ is further excited by the second ETU to ³F₂. After multiphonon de-excitation to ³H₄, Tm³⁺ experiences the third, phonon-assisted, ETU, populating the ¹G₄ level [42], with subsequent emissions to ³H₆ and ³F₄ levels.

The CIE 1931 and CIE 1976 chromaticity coordinates were estimated by the JOES application software [43], while the CIE 1976 diagram is presented in Fig. 3d. The chromaticity is determined from the emission spectrum in Fig. 3a by converting the intensity to be proportional to irradiance (see Fig. 3d inset). The emission color does not depend significantly on the doping concentration. As the upconversion emission color of Tm³⁺ co-doped samples lie in the NIR region, it is of no significance for chromaticity and Tm³⁺ is dropped from this analysis. In Ho³⁺ doped samples, however, the upconversion emission has a pure green color, while the third peak at above 750 nm lies outside the visible range [44]. The color purity (CP) is calculated from the equation [45]:

$$CP[\%] = \sqrt{\frac{(x - 1/3)^2 + (y - 1/3)^2}{(x_d - 1/3)^2 + (y_d - 1/3)^2}} \times 100\% \quad (1)$$

where (x_d, y_d) is the CIE 1931 coordinate of the dominant wavelength (λ_{dom}), and 1/3 values are the coordinates of the Standard Illuminant E (the ideal white source) [46]. The dominant wavelength is obtained by

extrapolating the straight line from the coordinates of the standard illuminant, through the (x,y) coordinate, to the spectral locus. Due to the high color purity, the dominant wavelength (λ_{dom}) has almost the same coordinate as colors of PL emissions. The CIE 1931 coordinates of Ho³⁺ co-doped samples are x = 0.312, y = 0.679, CP = 98.7 %, λ_{dom} = 550.6 nm. Its equivalent coordinates in the CIE 1976 diagram are u' = 0.119, v' = 0.581.

4. Conclusion

The popularity trend for upconversion sub-micron particles is constantly increasing due to their wide applications. The most targeted biological and medicinal applications require for the sub-micron particles to have high efficiency, absorb and emit in the biological windows while having low cytotoxicity. La₂O₂S co-doped with the famous upconverting pairs of Yb³⁺/Ho³⁺ and Yb³⁺/Tm³⁺ satisfy all these criteria. Upconversion sub-micron particles of lanthanum oxysulfide co-doped with Yb³⁺/Ho³⁺ and Yb³⁺/Tm³⁺ rare-earth pairs in various concentrations have been successfully synthesized. The method of choice was the optimized combustion technique which shows high efficiency while being an economically and environmentally friendly process. This simple method is optimal for processing of 50 nm pure-phase spherical particles. The use of the small number of precursors and the elimination of the hazardous gasses flux, while maintaining the high yield with reduced overall production time mark this optimized method as industrially competitive. These sub-micron particles showed the typical visible and NIR emissions of Ho³⁺ and Tm³⁺ upon 980 nm excitation and subsequent energy transfer from Yb³⁺ ions. After two ETUs, the Ho³⁺ showed the highest emissions from ⁵F₄+⁵S₂ to the ground level, slightly weaker from ⁵F₅, and the weakest from ⁵S₂ to the ⁵I₇. In Tm³⁺ the triple ETU was proved by observing emissions from ¹G₄. However, all the emissions but ³H₄→³H₆ at ca. 800 nm were of insignificant intensity. The concentration dependence on upconversion photoluminescence upon the 980 nm irradiation was investigated. The Yb³⁺/Ho³⁺ co-doped sample with 10 %/2 % concentrations, respectively, emitted the most intensely. Analogously, but with the lowest investigated concentrations of 4 %/1 % of Yb³⁺/Tm³⁺ is observed. The latter produced the highest photoluminescence with several times higher yield than the other samples. The spectral shape did not significantly change by changing concentrations. Ho³⁺ co-doped samples emit pure green color, while the vast majority of Tm³⁺ emission lies in the NIR region. Thus, the favoring characteristics of sub-micron particles presented in this paper and their facile, rapid and cheap synthesis label the La₂O₂S:Yb³⁺/Ho³⁺ and especially La₂O₂S:Yb³⁺/Tm³⁺ as a biomedical industrially important material.

CRedit authorship contribution statement

Aleksandar Ćirić: Investigation, Writing – original draft, Writing – review & editing, Visualization, Conceptualization, Project administration. **Milica Sekulić:** Writing – original draft, Writing – review &

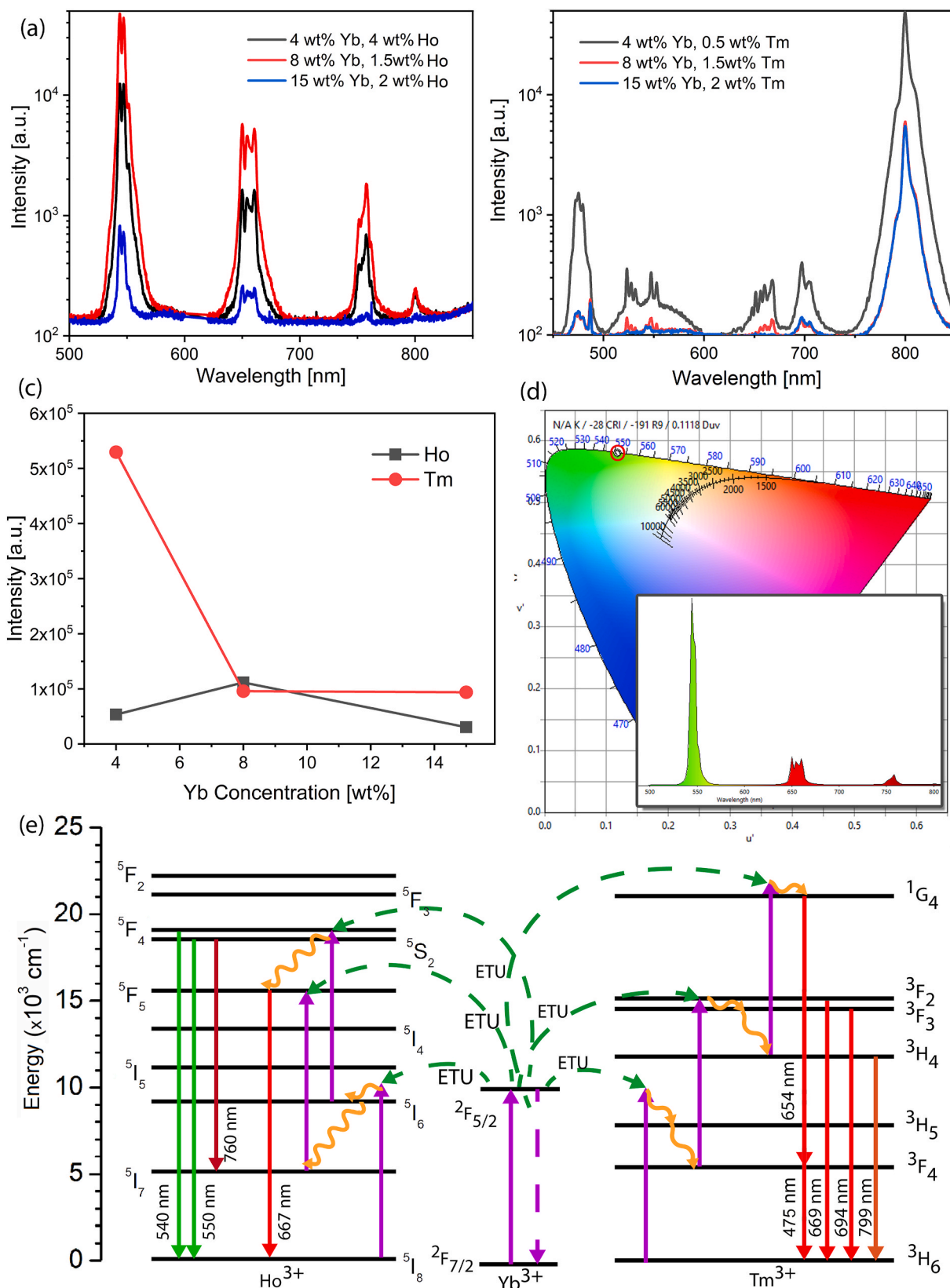


Fig. 3. Emission spectra of La₂O₂S nanoparticles, irradiated by 980 nm 150 mW laser beam, co-doped in various concentrations of (a) Yb³⁺/Ho³⁺ and (b) Yb³⁺/Tm³⁺. (c) Integrated intensities of total upconversion emission in dependence on the Yb³⁺ concentration. (d) CIE 1976 diagram of Ho³⁺ emission calculated from spectrum at (a) converted to irradiance (inset). (e) Corresponding energy level diagram: orange zig-zag lines represent multiphonon de-excitation or phonon assistance to ETU, green-dashed lines represent ETU.

editing, Investigation. **Kevil Shah:** Conceptualization, Methodology, Validation, Resources. **Bishwajit S. Chakrabarty:** Resources, Funding acquisition. **Miroslav D. Dramićanin:** Supervision, Project administration, Writing – review & editing.

Declaration of competing interest

The authors declare that they have no known competing financial interests or personal relationships that could have appeared to influence the work reported in this paper.

Acknowledgments

This research was funded by the Ministry of Education, Science and Technological development of the Republic of Serbia.

The authors wish to thank Dr. Željko Radovanović from the Innovation Center of Technology and metallurgy faculty, University of Belgrade for the EDS measurements.

Appendix A. Supplementary data

Supplementary data to this article can be found online at <https://doi.org/10.1016/j.optmat.2021.111417>.

References

- [1] S. Fischer, J.C. Goldschmidt, P. Löper, G.H. Bauer, R. Brüggemann, K. Krämer, D. Biner, M. Hermle, S.W. Glunz, Enhancement of silicon solar cell efficiency by upconversion: optical and electrical characterization, *J. Appl. Phys.* 108 (2010), <https://doi.org/10.1063/1.3478742>, 04912.
- [2] M. Suta, Ž. Antić, V. Đorđević, S. Kuzman, M.D. Dramićanin, A. Meijerink, Making Nd^{3+} a sensitive luminescent thermometer for physiological temperatures — an account of pitfalls in Boltzmann thermometry making Nd^{3+} a sensitive luminescent thermometer for physiological temperatures — an account of pitfalls in Boltzmann thermometry, *Nanomaterials* 10 (2020) 543, <https://doi.org/10.3390/nano10030543>.
- [3] A.M. Kaczmarek, M. Suta, H. Rijckaert, A. Abalymov, I. Van Driessche, A. G. Skirtach, A. Meijerink, P. Van Der Voort, Visible and NIR upconverting Er^{3+} - Yb^{3+} luminescent nanorattles and other hybrid PMO-inorganic structures for in vivo nanothermometry, *Adv. Funct. Mater.* 30 (2020) 2003101, <https://doi.org/10.1002/adfm.202003101>.
- [4] C.D.S. Brites, P.P. Lima, N.J.O. Silva, A. Millán, V.S. Amaral, F. Palacio, L.D. Carlos, Thermometry at the nanoscale, *Nanoscale* 4 (2012) 4799, <https://doi.org/10.1039/c2nr30663h>.
- [5] M.D. Dramićanin, Trends in luminescence thermometry, *J. Appl. Phys.* 128 (2020), <https://doi.org/10.1063/5.0014825>, 049092.
- [6] F. Wang, D. Banerjee, Y. Liu, X. Chen, X. Liu, Upconversion nanoparticles in biological labeling, imaging, and therapy, *Analyst* 135 (2010) 1839, <https://doi.org/10.1039/c0an00144a>.
- [7] G. Chen, H. Qiu, P.N. Prasad, X. Chen, Upconversion nanoparticles: design, nanochemistry, and applications in theranostics, *Chem. Rev.* 114 (2014) 5161–5214, <https://doi.org/10.1021/cr400425h>.
- [8] C. Wang, L. Cheng, Z. Liu, Drug delivery with upconversion nanoparticles for multi-functional targeted cancer cell imaging and therapy, *Biomaterials* 32 (2011) 1110–1120, <https://doi.org/10.1016/j.biomaterials.2010.09.069>.
- [9] F. Auzel, Upconversion and anti-Stokes processes with f and d ions in solids, *Chem. Rev.* 104 (2004) 139–174, <https://doi.org/10.1021/cr020357g>.
- [10] C. Strohöfer, A. Polman, Absorption and emission spectroscopy in Er^{3+} - Yb^{3+} doped aluminum oxide waveguides, *Opt. Mater.* 21 (2003) 705–712, [https://doi.org/10.1016/S0925-3467\(02\)00056-3](https://doi.org/10.1016/S0925-3467(02)00056-3).
- [11] F. Auzel, Compteur quantique par transfert d'énergie entre deux ions de terres rares dans un tungstate mixte et dans un verre, *CR Acad. Sci. Paris* 262 (1966) 1016–1019.
- [12] V. Lojpur, M. Nikolic, L. Mancic, O. Milosevic, M.D. Dramićanin, $\text{Y}2\text{O}_3:\text{Yb},\text{Tm}$ and $\text{Y}2\text{O}_3:\text{Yb},\text{Ho}$ powders for low-temperature thermometry based on up-conversion fluorescence, *Ceram. Int.* 39 (2013) 1129–1134, <https://doi.org/10.1016/j.ceramint.2012.07.036>.
- [13] X. Li, R. Wang, F. Zhang, D. Zhao, Engineering homogeneous doping in single nanoparticle to enhance upconversion efficiency, *Nano Lett.* 14 (2014) 3634–3639, <https://doi.org/10.1021/nl501366x>.
- [14] J.F. Suyver, J. Grimm, M.K. van Veen, D. Biner, K.W. Krämer, H.U. Güdel, Upconversion spectroscopy and properties of NaYF_4 doped with, and/or, *J. Lumin.* 117 (2006) 1–12, <https://doi.org/10.1016/j.jlumin.2005.03.011>.
- [15] M. Wang, G. Abbineni, A. Clevenger, C. Mao, S. Xu, Upconversion nanoparticles: synthesis, surface modification and biological applications, *Nanomedicine Nanotechnology, Biol. Med.* 7 (2011) 710–729, <https://doi.org/10.1016/j.nano.2011.02.013>.
- [16] M. Pokhrel, A. Kumar Gangadharan, D.K. Sardar, High upconversion quantum yield at low pump threshold in $\text{Er}^{3+}/\text{Yb}^{3+}$ doped $\text{La}_2\text{O}_3\text{S}$ phosphor, *Mater. Lett.* 99 (2013) 86–89, <https://doi.org/10.1016/j.matlet.2013.02.062>.
- [17] N. Hakme, C. Chlique, O. Merdrignac-Conanec, B. Fan, F. Cheviré, X. Zhang, X. Fan, X. Qiao, Combustion synthesis and up-conversion luminescence of $\text{La}_2\text{O}_3\text{S}:\text{Er}^{3+},\text{Yb}^{3+}$ nanophosphors, *J. Solid State Chem.* 226 (2015) 255–261, <https://doi.org/10.1016/j.jssc.2015.02.015>.
- [18] W. Chen, *Doped Nanomaterials and Nanodevices: Quantum Dots, Nanowires, Nanotubes, and Applications*, American Scientific Publishers, 2010.
- [19] G.A. Kumar, M. Pokhrel, A. Martinez, D.K. Sardar, Synthesis and upconversion spectroscopy of Yb Er doped $\text{M}_2\text{O}_2\text{S}$ ($\text{M} = \text{La}, \text{Gd}, \text{Y}$) phosphors, *Sci. Adv. Mater.* 4 (2012) 623–630, <https://doi.org/10.1166/sam.2012.1329>.
- [20] M. Pokhrel, G.A. Kumar, D.K. Sardar, Highly efficient NIR to NIR and VIS upconversion in Er^{3+} and Yb^{3+} doped in $\text{M}_2\text{O}_2\text{S}$ ($\text{M} = \text{Gd}, \text{La}, \text{Y}$), *J. Mater. Chem.* 1 (2013) 11595, <https://doi.org/10.1039/c3ta12205k>.
- [21] M. Kottaisamy, K. Horikawa, H. Kominami, T. Aoki, N. Azuma, T. Nakamura, Y. Nakanishi, Y. Hatanaka, Synthesis and characterization of fine particle $\text{Y}_2\text{O}_3\text{S}:\text{Eu}$ red phosphor at low-voltage excitation, *J. Electrochem. Soc.* 147 (2000) 1612, <https://doi.org/10.1149/1.1393405>.
- [22] K. Ikeue, T. Kawano, M. Eto, D. Zhang, M. Machida, X-ray structural study on the different redox behavior of La and Pr oxysulfates/oxysulfides, *J. Alloys Compd.* 451 (2008) 338–340, <https://doi.org/10.1016/j.jallcom.2007.04.145>.
- [23] I.P. Machado, V.C. Teixeira, C.C.S. Pedroso, H.F. Brito, L.C.V. Rodrigues, X-ray scintillator $\text{Gd}_2\text{O}_2\text{S}:\text{Tb}^{3+}$ materials obtained by a rapid and cost-effective microwave-assisted solid-state synthesis, *J. Alloys Compd.* 777 (2019) 638–645, <https://doi.org/10.1016/j.jallcom.2018.10.348>.
- [24] I.P. Machado, C.C.S. Pedroso, J.M. de Carvalho, V. de C. Teixeira, L.C.V. Rodrigues, H.F. Brito, A new path to design near-infrared persistent luminescence materials using Yb^{3+} -doped rare earth oxysulfides, *Scripta Mater.* 164 (2019) 57–61, <https://doi.org/10.1016/j.scriptamat.2019.01.023>.
- [25] J. Miranda de Carvalho, C.C.S. Pedroso, I.P. Machado, J. Hölsä, L.C.V. Rodrigues, P. Gluchowski, M. Lastusaari, H.F. Brito, Persistent luminescence warm-light LEDs based on Ti-doped $\text{RE}_2\text{O}_2\text{S}$ materials prepared by rapid and energy-saving microwave-assisted synthesis, *J. Mater. Chem. C* 6 (2018) 8897–8905, <https://doi.org/10.1039/C8TC01826J>.
- [26] A.S. Rogachev, V.A. Shugaev, C.R. Kachelmyer, A. Varma, Mechanisms of structure formation during combustion synthesis of materials, *Chem. Eng. Sci.* 49 (1994) 4949–4958, [https://doi.org/10.1016/0009-2509\(94\)00389-0](https://doi.org/10.1016/0009-2509(94)00389-0).
- [27] S.R. Turns, others, *Introduction to Combustion*, McGraw-Hill Companies, 1996.
- [28] J.J. Kingsley, K.C. Patil, A novel combustion process for the synthesis of fine particle α -alumina and related oxide materials, *Mater. Lett.* 6 (1988) 427–432, [https://doi.org/10.1016/0167-577X\(88\)90045-6](https://doi.org/10.1016/0167-577X(88)90045-6).
- [29] A. Varma, A.S. Mukasyan, A.S. Rogachev, K.V. Manukyan, Solution combustion synthesis of nanoscale materials, *Chem. Rev.* 116 (2016) 14493–14586, <https://doi.org/10.1021/acs.chemrev.6b00279>.
- [30] A. Kumar, E.E. Wolf, A.S. Mukasyan, Solution combustion synthesis of metal nanopowders: nickel-Reaction pathways, *AIChE J.* 57 (2011) 2207–2214, <https://doi.org/10.1002/aic.12416>.
- [31] K. Shah, A. Ćirić, K.V.R. Murthy, B.S. Chakrabarty, Investigation of a new way of synthesis for Nano crystallites of $\text{La}_2\text{O}_3\text{S}$ & $1\%\text{Ln}^{3+}$ ($\text{Ln} = \text{Pr}, \text{Eu}, \text{Tb}, \text{Dy}, \text{Er}$) doped $\text{La}_2\text{O}_3\text{S}$ and study their structural and optical properties, *J. Alloys Compd.* 851 (2021) 156725, <https://doi.org/10.1016/j.jallcom.2020.156725>.
- [32] J.-G. Li, X. Wang, W. Liu, Q. Zhu, X. Li, X. Sun, $(\text{La}_{0.97}\text{RE}_{0.01}\text{Yb}_{0.02})_2\text{O}_2\text{S}$ nanophosphors converted from layered hydroxyl sulfate and investigation of upconversion photoluminescence ($\text{RE}=\text{Ho}, \text{Er}$), *Nanoscale Res. Lett.* 12 (2017) 508, <https://doi.org/10.1186/s11671-017-2277-4>.
- [33] X. Wang, Q. Zhu, J.-G. Li, Z. Hu, G. Zhu, C. Wang, $\text{La}_2\text{O}_3\text{S}:\text{Tm}/\text{Yb}$ as a novel phosphor for highly pure near-infrared upconversion luminescence, *Scripta Mater.* 149 (2018) 121–124, <https://doi.org/10.1016/j.scriptamat.2018.02.031>.
- [34] Q. Pan, D. Yang, S. Kang, J. Qiu, G. Dong, Regulating mid-infrared to visible fluorescence in monodispersed Er^{3+} -doped $\text{La}_2\text{O}_3\text{S}$ ($\text{La}_2\text{O}_3\text{SO}_4$) nanocrystals by phase modulation, *Sci. Rep.* 6 (2016) 37141, <https://doi.org/10.1038/srep37141>.
- [35] X. Luo, W. Cao, Ethanol-assistant solution combustion method to prepare $\text{La}_2\text{O}_3\text{S}:\text{Yb},\text{Pr}$ nanometer phosphor, *J. Alloys Compd.* 460 (2008) 529–534, <https://doi.org/10.1016/j.jallcom.2007.06.011>.
- [36] B.M. Jaffar, H.C. Swart, H.A.A. Seed Ahmed, A. Yousif, R.E. Kroon, Optical properties and stability of Bi doped $\text{La}_2\text{O}_3\text{S}$, *Opt. Mater.* 95 (2019) 109260, <https://doi.org/10.1016/j.optmat.2019.109260>.
- [37] A. Ćirić, S. Stojadinović, Photoluminescence studies of $\text{ZrO}_2:\text{Tm}^{3+}/\text{Yb}^{3+}$ coatings formed by plasma electrolytic oxidation, *J. Lumin.* 214 (2019) 2–11, <https://doi.org/10.1016/j.jlumin.2019.116568>.
- [38] W.T. Carnall, H. Crosswhite, H.M. Crosswhite, Energy Level Structure and Transition Probabilities in the Spectra of the Trivalent Lanthanides in LaF_3 , Argonne, IL (United States), 1978, <https://doi.org/10.2172/6417825>.
- [39] H. Huang, H. Zhou, J. Zhou, T. Wang, D. Huang, Y. Wu, L. Sun, G. Zhou, J. Zhan, J. Hu, Enhanced anti-stokes luminescence in $\text{LaNbO}_4:\text{Ln}^{3+}$ ($\text{Ln}^{3+} = \text{Yb}^{3+}, \text{Er}^{3+}/\text{Ho}^{3+}/\text{Tm}^{3+}$) with abundant color, *RSC Adv.* 7 (2017) 16777–16786, <https://doi.org/10.1039/C6RA28592A>.
- [40] C. Li, B. Dong, S. Li, C. Song, Er^{3+} - Yb^{3+} co-doped silicate glass for optical temperature sensor, *Chem. Phys. Lett.* 443 (2007) 426–429, <https://doi.org/10.1016/j.cplett.2007.06.081>.
- [41] I. Martin, V. Rodriguez, V. Lavin, U. Rodriguez-Mendoza, Upconversion dynamics in Yb^{3+} - Ho^{3+} doped fluoroindate glasses, *J. Alloys Compd.* 275–277 (1998) 345–348, [https://doi.org/10.1016/S0925-8388\(98\)00336-3](https://doi.org/10.1016/S0925-8388(98)00336-3).

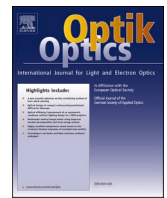
- [42] J.-C. Boyer, L.A. Cuccia, J.A. Capobianco, Synthesis of colloidal upconverting NaYF₄: Er³⁺/Yb³⁺ and Tm³⁺/Yb³⁺ monodisperse nanocrystals, *Nano Lett.* 7 (2007) 847–852, <https://doi.org/10.1021/nl070235+>.
- [43] A. Ćirić, S. Stojadinović, M. Sekulić, M.D. Dramićanin, JOES: an application software for Judd-Ofelt analysis from Eu³⁺ emission spectra, *J. Lumin.* 205 (2019) 351–356, <https://doi.org/10.1016/j.jlumin.2018.09.048>.
- [44] W.S. Stiles, Color vision: the approach through increment-threshold sensitivity, *Proc. Natl. Acad. Sci. U. S. A* 45 (1959) 100.
- [45] A. Ćirić, S. Stojadinović, Photoluminescence of ZrO₂:Gd³⁺ and ZrO₂:Dy³⁺ coatings formed by the plasma electrolytic oxidation, *J. Alloys Compd.* 832 (2020), <https://doi.org/10.1016/j.jallcom.2020.154907>.
- [46] Á. Antal, P. Görög, Á.L. Veres, P. Balla, Á. Török, Colour of stone slabs under different standard illuminations, *Period. Polytech. Civ. Eng.* (2016), <https://doi.org/10.3311/PPci.9038>.



ELSEVIER

Contents lists available at ScienceDirect

Optik

journal homepage: www.elsevier.com/locate/ijleo

La₂O₂S:Er³⁺/Yb³⁺ nanoparticles synthesized by the optimized furnace combustion technique and their high-resolution temperature sensing

Aleksandar Ćirić^{a,*}, Kevil Shah^b, Milica Sekulić^a, B.S. Chakrabarty^b,
Miroslav D. Dramićanin^{a,c}

^a Vinča Institute of Nuclear Sciences – National Institute of the Republic of Serbia, University of Belgrade, Belgrade, Serbia

^b Applied Physics Department, Faculty of Technology & Engineering, The Maharaja Sayajirao University of Baroda, Vadodara, Gujarat, India

^c College of Sciences, Chongqing University of Posts and Telecommunications, Chongqing 400065, People's Republic of China

ARTICLE INFO

Keywords:

Nanoparticles
Upconversion
Yb³⁺
Er³⁺
Furnace combustion
Photoluminescence

ABSTRACT

Nanoparticles of less than 100 nm of La₂O₂S co-doped with Er³⁺ and Yb³⁺ in 2% and 12% concentrations, respectively, were synthesized by the improved furnace combustion technique that limits the precursor usage and without the hazardous chemicals. The lanthanum oxysulfide was identified in hexagonal crystal phase. Under 980 nm excitation the sample exhibits a typical upconversion photoluminescence for Yb³⁺/Er³⁺. Due to the high concentration of Yb³⁺, the red emission of Er³⁺ is of high intensity due to the energy back-transfer. The red emission is less pronounced in downshifting spectrum. Chromaticity analysis shows high color purities of emissions. La₂O₂S:Er³⁺/Yb³⁺ nanoparticle performances as a luminescent temperature sensor were first predicted by the Judd-Ofelt theory and then compared with the conventional experimental thermometry by Luminescence intensity ratio method, with an excellent match in all parameters. The relative sensitivity at 300 K is 1.14 K⁻¹ and it remains relatively high at the physiologically relevant range. The obtained temperature resolution was 0.17 K at 300 K.

1. Introduction

The upconversion, a process of material absorption of lower energy and subsequent emission of higher energy photons, is experiencing a rapid interest since its discovery in 1966 by Auzel [1], owing mostly to the recent applications and escalated research of nanoparticles. The range of applications of upconverting nanoparticles is wide, from medicinal [2], in solar-cells [3], data storage, solid-state lasers [4], sensors [5,6], etc. As they experience no photobleaching, no background luminescence and phosphorescence, while having narrow emission bands they are considered a state-of-the-art in the biomedical diagnosis, anticounterfeiting, or X-ray imaging [7].

Of all the upconversion nanoparticles, those co-doped with Yb³⁺/Er³⁺ are the most famous, due to the efficient absorption and emission in the biological window (spectral regions in which the living tissue is transparent) [8] and high efficiency due to the efficient energy transfer from Yb³⁺ to Er³⁺, while the former has a large absorption cross section [9]. Upon 980 nm irradiation, both Yb³⁺ and Er³⁺ get excited via ²F_{7/2}→²F_{5/2} and ⁴I_{15/2}→⁴I_{11/2} transitions, respectively, former being an order of magnitude more efficient [10].

* Corresponding author.

E-mail address: aleksandar.ciric@ff.bg.ac.rs (A. Ćirić).

Table 1
The comparison of various techniques for La₂O₂S synthesis.

Material	Method	Precursors	Fuel	Temperature and duration	Particle size	Reference
La ₂ O ₂ S 12Yb 2Er	Furnace combustion	Ln(NO ₃) ₃ Thiourea	Urea	490 °C 20 min	Less than 100 nm	This work
La ₂ O ₂ S: Ln (Ln= Pr, Eu, Tb, Dy and Er)	Furnace combustion	Ln(NO ₃) ₃ Thiourea	Urea	490 °C 20 min		[27]
La ₂ O ₂ S: Ln (Ln= Pr, Eu, Tb, Dy and Er)	Hydrothermal	Ln(NO ₃) ₃	sulfur powder	250 °C for 24 h	Not pure	[27]
La ₂ O ₂ S: Ln (Ln= Pr, Eu, Tb, Dy and Er)	Solid State	Ln(NO ₃) ₃	sulfur powder	1000 °C 8 h	Not pure	[27]
La ₂ O ₂ S:Bi	ethanol-assisted solution combustion	Ln(NO ₃) ₃	thioacetamide	400 °C 15 min and 900 °C 2 h in 5%H ₂ in Ar	500 nm	[28]
La ₂ O ₂ S	hydrothermal reaction	RE nitrates, (NH ₄) ₂ SO ₄ , NH ₃ ·		100 °C for 24 h	400 nm	[29]
La ₂ O ₂ S: Yb ³⁺ , Er ³⁺	solid state	La ₂ O ₃ , Yb ₂ O ₃ , Er ₂ O ₃ , S		flow H ₂ at 1200 °C for 1 h	/	[30]
La ₂ O ₂ S: 9%Yb, 1%Er	solid state flux fusion method	La ₂ O ₃ , Yb ₂ O ₃ , Er ₂ O ₃ , S	Na ₂ CO ₃ , K ₃ PO ₄	1200 °C for 6 h under CO reducing	3.8 μm	[20]
La ₂ O ₂ S:Eu ³⁺	hydrothermal method	La ₂ O ₃ and Eu ₂ O ₃ S		1150 °C for 60 min		[31]
La ₂ O ₂ S:Eu ³⁺	hydrothermal method	La ₂ O ₃ and Eu ₂ O ₃ S		120 °C 24 h, 500 °C for 2 h, 600 °C for 1 h	Nanowires 10 nm	[31]
La ₂ O ₂ S:Sm ³⁺	sulfide-fusion method	La ₂ O ₃ , Sm ₂ O ₃ sulfur	Na ₂ CO ₃	150 °C 24 h, 500 °C for 2 h, 600 °C for 1 h	sub-meter materials 500–1000 nm	[31]
La ₂ O ₂ S:Eu, La ₂ O ₂ S:Eu/Yb	solid state	La ₂ O ₃ , Eu ₂ O ₃ , Yb ₂ O ₃ S	Na ₂ CO ₃	1100–1400 °C 95% N ₂ , 5% H ₂ for 2 h	/	[32]
La ₂ O ₂ S:Tb ³⁺	one-step flux method	La ₂ O ₃ , Tb ₄ O ₇ sublimed sulfur	Na ₂ CO ₃	700 °C for 1 h	Not pure	[33]
La ₂ O ₂ S:Tb ³⁺	one-step flux method	La ₂ O ₃ , Tb ₄ O ₇ sublimed sulfur	Na ₂ CO ₃	900–1100 °C	04–1 μm	[34]
La ₂ O ₂ S:Tb ³⁺	one-step flux method	La ₂ O ₃ , Tb ₄ O ₇ sublimed sulfur	Na ₂ CO ₃	900–1100 °C	3.8 μm	[34]

Yb³⁺ is a well-known sensitizer, as it can effectively transfer energy to other ions with energy level difference similar to the energy of the ²F_{5/2}. Other famous pairs are Yb³⁺/Tm³⁺ and Yb³⁺/Ho³⁺, however, as their energy levels closest to the ²F_{5/2} are with lower energy, the energy transfer process is phonon assisted [11]. When Er³⁺ is excited to ⁴I_{11/2} either by ground state absorption or energy transfer from Yb³⁺, it may experience yet another of one of the two effects: excited state absorption or another energy transfer, the latter being by far more frequent. At this point the electron of Er³⁺ ion is in ⁴F_{7/2} state and after rapid depopulation to ²H_{11/2} or ⁴S_{3/2} levels it de-excites radiatively emitting green light, or red after depopulation to the ⁴F_{9/2} [12]. The latter is also promoted by the back-transfer to Yb³⁺, which is proportional to the Yb³⁺:Er³⁺ concentration ratio [13,14]. Conversely, if the doping concentrations are too high, the concentration quenching will dominate over the radiative emissions or Yb³⁺-Er³⁺ energy transfer process [15]. The most frequently used concentration ratio of Yb³⁺/Er³⁺ pair is 3–6:1 [16–18]. The methods for overcoming the concentration limitations such as core-shell structures or by tuning the excitation power density are outside the scope of this article.

La₂O₂S is known as the wide band-gap (4.6 – 4.8 eV) material and an efficient host matrix for the rare-earth doped ions [19]. This was well proven as well for the Yb³⁺/Er³⁺ co-doped La₂O₂S by Pokhrel et al. by comparing the upconversion quantum yields to that of the well-known NaYF₄:Yb³⁺/Er³⁺ nanoparticles [20]. The fluorides, which are considered the most efficient hosts for the upconversion nanoparticles [21], suffer from high cytotoxicity and low chemical stability, limiting their usage for large scale industrial applications or in vivo [20]. The chemically stable oxides are limited by the relatively high phonon energy, thus featuring low upconversion efficiencies. Oxyulfides kept the high chemical stability and low cytotoxicity of oxides, while having the lower phonon energies close to that of fluorides, resulting in the efficient upconversion [22]. Additionally, they can be manufactured rapidly and economically [23]. Despite the comparable efficiencies and the advantages using oxides to fluorides or halides regarding chemical [24] and thermal stabilities [25], there are only a handful of papers describing the La₂O₂S:Yb³⁺/Er³⁺ nanoparticles [20,26].

There are several methods by which the rare-earth doped La₂O₂S nanoparticles can be created (Table 1) [20,27–34]. The solid-state technique requires the high temperature of ca. 1150 °C, different fluxes, and a long synthesis time [20,30]. The ethanol assisted combustion technique has two-steps: (i) the combustion process with Thioacetamide (TTA, CH₃CSNH₂) as a fuel, and (ii) solid-state technique with when H₂S/N₂ gases pass through [22]. We have modified the known furnace combustion technique in a more environmentally and safely manner, as there was no use of fluxes or hazardous gases during the procedure [27]. The approach limits the precursors, minimizing the needed resources. The maximum yield of the final product is obtained with less synthesis time. As this novel modification of the popular furnace combustion technique has ecological and economic advantages, it may catch an eye of the industrial world and research laboratories. To validate this statement for the synthesis of La₂O₂S co-doped with Yb³⁺ and Er³⁺, it was necessary to perform morphological, phase and photoluminescent characterizations. The rare-earth doping concentrations are selected targeting energy back-transfer and high overall emission intensity.

Luminescence thermometry comprises a series of methods for temperature readout based on the temperature dependence of the luminescence intensities, positions or lifetimes [5,35]. For remote or in vivo sensing of temperature the luminescence thermometry is

recognized as the most perspective method [5,36,37]. The most frequently used method in Luminescence thermometry, Luminescence intensity ratio (LIR, frequently called "Fluorescence intensity ratio" or FIR) is based on the ratio of two emissions, as it is self-referencing (does not depend on fluctuations in excitation), economical and relatively simple [38]. When the two energy levels are thermalized (separated below ca. 2000 cm⁻¹ allowing an efficient population of the energetically higher level by thermal energy) their ratio of integrated emissions follows the Boltzmann distribution [39,40]:

$$LIR = \frac{I_H}{I_L} = B \exp\left(-\frac{\Delta E}{kT}\right) \quad (1)$$

where $k = 0.695 \text{ cm}^{-1} \text{ K}^{-1}$ is the Boltzmann constant, B is the temperature invariant parameter that depends only on the host, and ΔE is the energy gap between thermalized levels. The temperature sensor performances are estimated by figures of merit in thermometry, absolute and relative sensitivities and the temperature resolution. They are given for LIR method, respectively as [41]:

$$S_a [K^{-1}] = \left| \frac{\partial LIR}{\partial T} \right| = \frac{\Delta E}{kT^2} LIR \quad (2)$$

$$S_r [\%K^{-1}] = \frac{S_a}{LIR} \cdot 100\% = \frac{\Delta E}{kT^2} \cdot 100\% \quad (3)$$

$$\Delta T [K] = \frac{\sigma_a}{S_a} = \frac{\sigma_r}{S_r} \quad (4)$$

where $\sigma_{a,r}$ are the absolute and relative uncertainties in measurement, respectively, expressed as a standard deviation, and they depend mostly on the experimental conditions. For luminescence temperature sensing by LIR method Er³⁺ within the physiological temperature range Er³⁺ is recognized as one of the most effective single ion luminescent Boltzmann thermometers [42] and this is why it is the most utilized lanthanide for that purpose and labeled as a "workhorse" [43].

Unfortunately, this conventional luminescent thermometry is lengthy and requires a relatively complex data processing. There are numerous hosts in which Er³⁺/Yb³⁺ can be incorporated which greatly complicates the selection of the host for sensor. As we have previously demonstrated [39,44] Judd-Ofelt theory, the centerpiece theory in spectroscopy of lanthanides [45], can provide a guidance by allowing for prediction of thermometric figures of merit. The prediction can be performed by Judd-Ofelt parametrization from a single spectrum at room temperature or simply by taking the Judd-Ofelt parameters from literature for a given lanthanide in a selected host. This means that the temperature invariant parameter B can be estimated from the Judd-Ofelt parameters, and consequently the absolute sensitivity. For the LIR of emissions ²H_{11/2}→⁴I_{15/2} and ⁴S_{3/2}→⁴I_{15/2}, B parameter is approximately equal to [39]:

$$B = \frac{3.35\Omega_2 + 1.94\Omega_4 + \Omega_6}{\Omega_6} \quad (5)$$

and by returning that value into Eqs. 1 and 2, the absolute sensitivity is also given from the Judd-Ofelt parameters.

As the Er³⁺/Yb³⁺ in pair shows high perspective for luminescent probes for biomedical applications, including temperature sensing and imaging, we investigated the temperature sensing performances of Er³⁺/Yb³⁺ co-doped in the host with high upconversion efficiency (due to the low phonon energies) and low cytotoxicity, from room temperature to 550 K. The sensor performances are compared with the theoretically predicted values obtained by the Judd-Ofelt theory, as explained in our earlier work [43]. To our knowledge this is the first time of investigating the luminescence temperature sensing of materials created by the optimized furnace combustion technique and the first time of such investigation on La₂O₂S:Er³⁺/Yb³⁺ nanoparticles.

2. Experimental

The starting chemicals were Lanthanum, Ytterbium and Erbium Nitrate Hexahydrates (Ln(NO₃)₃·6H₂O, Ln = La, Yb, Er, 99% purity, Xinyu advanced materials limited), Thiourea (NH₂CSNH₂), Urea, Ethanol and water. The stoichiometric amounts of Ln(NO₃)₃·6H₂O and Thiourea were taken as per host to activators ratio, for a final product with 12% Yb³⁺ and 2% Er³⁺ concentrations. The 2 g of Urea, 10 ml of Ethanol, and 20 ml of distilled water were added to the stoichiometric solution, poured into the alumina crucible and kept in the furnace. The combustion was started on a full scale at 490 °C for about 20–25 min. The massive amounts of gases were released from the sample because the nitrate solutions were violently reacting with the fuels (Urea + Ethanol). The furnace was shut down after the reaction, and the product was allowed to cool down naturally in the furnace. After 24 h, the crucible was pulled out from the furnace and then crushed into fine powder form by using a mortar – pestle.

The crystallinity of the created powder was estimated by the X-ray diffraction (XRD) measurements on a Rigaku SmartLab diffractometer operating with Cu K radiation (30 mA, 40 kV) in the 2θ range from 10° to 90°, with step of 0.02°. Mira3 Tescan field emission scanning electron microscope (FE-SEM) was used for microstructural characterization, operated at 20 keV with magnification from 10.000 to 100.000. The sample was irradiated by the powerful 980 nm solid-state laser (150 mW optical power, 300 mW/cm² power density, model MDLH 980 3 W). The upconversion emission was recorded via the fiber-optic bundle coupled to the high-resolution spectrograph (model FHR 1000, with Horiba Jobin-Yvon ICCD detector). Temperature of the sample was set by MicroOptic MHCS400 heating/cooling stage with MTDC600 temperature controller. Downshifting emission and excitation spectra were recorded by the Horiba Jobin Yvon Fluorolog FL3–22 spectrofluorometer equipped with 450 W xenon lamp.

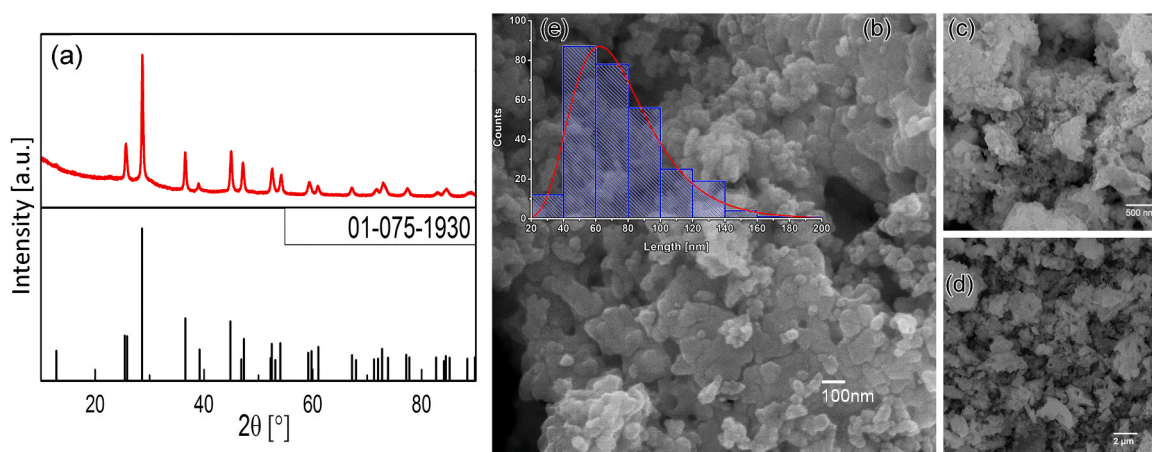


Fig. 1. (a) XRD and (b-d) SEM images of lanthanum oxysulfide co-doped with 12% Yb³⁺ and 2% Er³⁺. (e) Histogram of particle diameters created from SEM images by the ImageJ software.

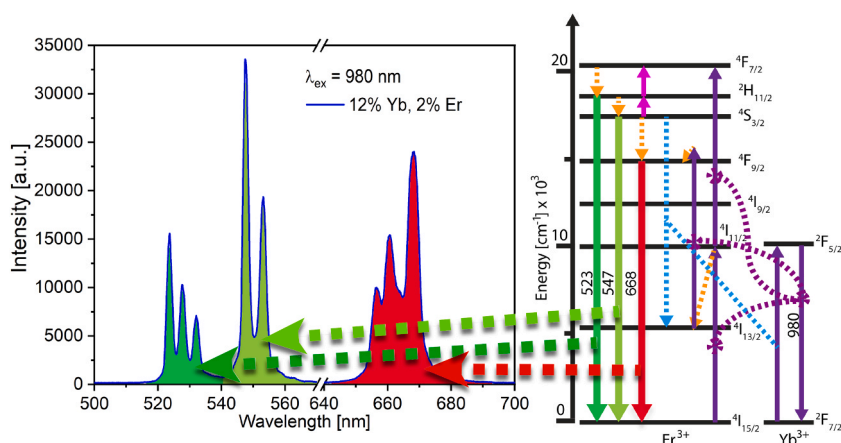


Fig. 2. Upconversion emission spectrum of La₂O₂S:Yb³⁺/Er³⁺, under 980 nm excitation, and the corresponding energy level diagram. Orange-dashed lines represent multiphonon and phonon assisted processes, light-purple arrows are the thermal population, dashed blue line represents the energy back-transfer. (For interpretation of the references to colour in this figure legend, the reader is referred to the web version of this article.)

3. Results

3.1. Morphological and Phase characterizations

The XRD spectrum of La₂O₂S:Yb³⁺/Er³⁺ with 12% Yb³⁺ and 2% Er³⁺ is presented in Fig. 1a), and it corresponds to the ICDD 01-075-1930 card, representing La₂O₂S in Hexagonal (P⁻3m1) phase with average crystallite size 124(6) Å.

SEM images are presented in Fig. 1b-d. The obtained sample displays a typical morphology for combustion synthesis process of strongly agglomerated particles. By the ImageJ software application from the SEM images the average particle size is estimated to be ca. 60 nm, while the majority of the agglomerated particles are below 100 nm in diameter (see Fig. 1e).

3.2. Photoluminescence of La₂O₂S:Er³⁺/Yb³⁺

Fig. 2 shows the PL upconversion spectrum under 980 nm excitation. Three major peaks were observed: ²H_{11/2} → ⁴I_{15/2}, ²S_{3/2} → ⁴I_{15/2}, ⁴F_{9/2} → ⁴I_{15/2} with maxima at 523 nm, 547 nm, and 668 nm, respectively [46,47]. The energy level diagram clearly depicts the well-known mechanisms behind the PL. The Er³⁺ is solely capable of absorbing the 980 nm photons, as the upconversion is observed in single-doped materials [48]. However, the absorption cross-section of Yb³⁺ at this wavelength is an order of magnitude greater. After Yb³⁺ gets excited to its only excited level, ²F_{5/2}, it non-radiatively transfers the energy to the nearest Er³⁺ ion, by the very probable process called energy transfer upconversion (ETU) or APTE (“Addition of Photon for Transfer of Energy”) [13]. After the Er³⁺ has an optical center in ⁴I_{11/2} level, it can radiatively de-excite NIR photons, non-radiatively de-excite to ⁴I_{13/2}, or it can experience the second

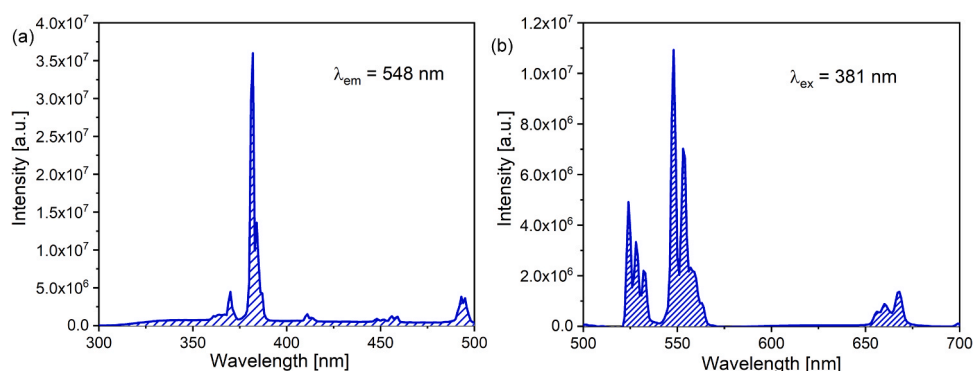


Fig. 3. (a) Excitation spectrum monitored at 548 nm, (b) emission spectrum by 381 nm excitation.

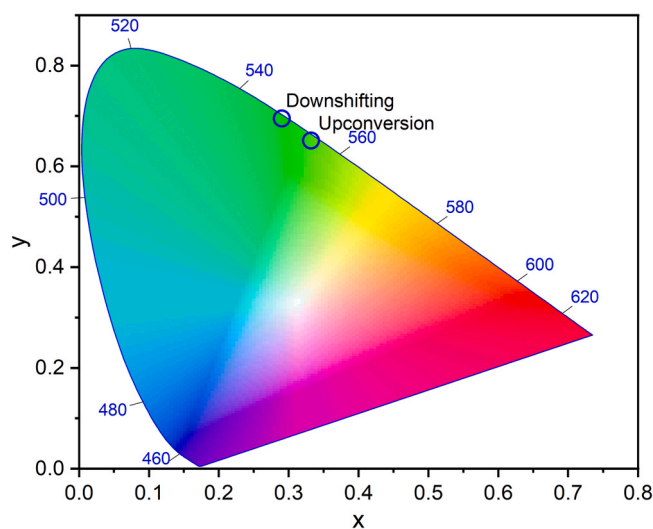


Fig. 4. CIE 1931 chromaticity diagram of downshifting and upconversion spectra of $\text{La}_2\text{O}_2\text{S:Er}^{3+}/\text{Yb}^{3+}$.

Table 2

CIE 1931 chromaticity analysis of upconversion and downshifting spectra of $\text{La}_2\text{O}_2\text{S:Er}^{3+}/\text{Yb}^{3+}$.

Mechanism	x	y	λ_{dom} [nm]	CP [%]
Upconversion	0.332	0.651	554.2	96.1
Downshifting	0.290	0.695	548.2	97.6

boost to the higher levels, most probably by ETU. The two pathways are observed: (i) ${}^4\text{I}_{11/2} \rightarrow {}^4\text{F}_{7/2}$, or (ii) non-radiative de-excitation to ${}^4\text{I}_{13/2}$ with subsequent phonon-assisted upconversion to ${}^4\text{F}_{9/2}$ [48]. Once in ${}^4\text{F}_{7/2}$, Er^{3+} may experience multiphonon de-excitation in steps down to ${}^4\text{F}_{9/2}$, competing with the radiative emissions from each of the levels on this path [49]. As the maximum phonon energy in $\text{La}_2\text{O}_2\text{S}$ is 710 cm^{-1} [50], the multiphonon process is very probable for such small gaps. Competing effect is the population of the higher levels by thermal energy among the thermalized levels ${}^4\text{F}_{7/2}$, ${}^2\text{H}_{11/2}$ and ${}^4\text{S}_{3/2}$, which acts in accordance with the Boltzmann distribution [39]. An interesting phenomenon in $\text{Yb}^{3+}/\text{Er}^{3+}$ co-doped materials is the dependence of the spectral shape on the Yb^{3+} concentration, due to the energy back transfer ${}^4\text{S}_{3/2} (\text{Er}^{3+}) + {}^2\text{F}_{7/2} (\text{Yb}^{3+}) \rightarrow {}^4\text{I}_{13/2} (\text{Er}^{3+}) + {}^2\text{F}_{5/2} (\text{Yb}^{3+})$ [51]. This energy transfer contributes to the de-population of the ${}^4\text{F}_{7/2}$ in favor of ${}^4\text{F}_{9/2}$ level. Thus, the high intensity of the red emission at 668 nm is due to the high concentration of 12% Yb^{3+} used.

Excitation spectrum monitored at 548 nm which corresponds to the ${}^4\text{S}_{3/2} \rightarrow {}^4\text{I}_{15/2}$ downshifting emission of Er^{3+} is presented in Fig. 3a. The peaks at 370 nm, 382 nm, 411 nm, 448 nm, 456 nm, and 493 nm correspond to the excitations from the ground state to ${}^4\text{G}_{9/2}$, ${}^4\text{G}_{11/2}$, ${}^2\text{H}_{9/2}$, ${}^4\text{F}_{3/2}$, ${}^4\text{F}_{5/2}$, ${}^4\text{F}_{7/2}$, and ${}^2\text{H}_{11/2}$, respectively [52]. Downshifting emission under 381 nm excitation is displayed in Fig. 3b, and it is evident that the relative intensity of the red emission is significantly weaker, which is due to the level population mechanisms explained in Fig. 2.

Fig. 4. displays the CIE 1931 chromaticity diagram as obtained by the JOES application software [53]. The (x,y) CIE 1931

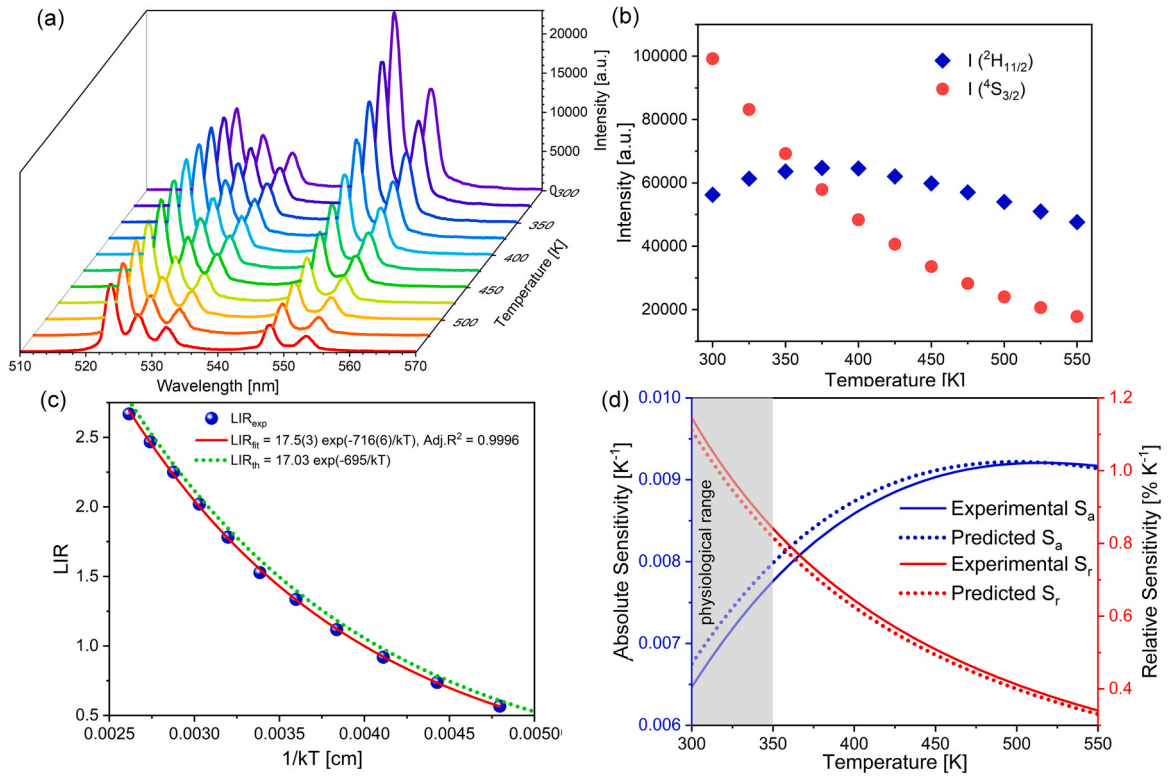


Fig. 5. (a) Upconversion spectra of $\text{La}_2\text{O}_2\text{S}:\text{Er}^{3+}/\text{Yb}^{3+}$ at various temperatures; (b) Integrated intensities of emissions from ${}^2\text{H}_{11/2}$ and ${}^4\text{S}_{3/2}$ to the ground level of Er^{3+} ; (c) Experimentally obtained LIR and theoretical fit to the Boltzmann distribution, and theoretical LIR obtained from the Judd-Ofelt thermometric model; (d) Absolute and Relative sensitivities from experimental LIR and from Judd-Ofelt thermometric model.

Table 3

Comparison of thermometric parameters and sensitivities of fitted values with obtained by the Judd-Ofelt thermometric model, as given in Ref. [43].

Method	ΔE	S_r (300 K)	S_a (300 K)	max (S_a)	T (max(S_a))	S_r (T (max(S_a)))
Exp. fit	716 cm^{-1}	$1.14\% \text{ K}^{-1}$	0.0065 K^{-1}	0.0092 K^{-1}	514 K	$0.39\% \text{ K}^{-1}$
Theoretical	695 cm^{-1}	$1.11\% \text{ K}^{-1}$	0.0068 K^{-1}	0.0092 K^{-1}	499 K	$0.40\% \text{ K}^{-1}$

coordinates are given together with the dominant wavelength (λ_{dom}) and Color Purity (CP) in Table 2. CP is estimated by [54]:

$$CP = \sqrt{\frac{(x-1/3)^2 + (y-1/3)^2}{(x_d-1/3)^2 + (y_d-1/3)^2}} \quad (5)$$

where (x_d, y_d) are the CIE coordinates of the dominant wavelength. Due to the more intense red peak in the spectrum of upconversion emission, the dominant wavelength is shifted to higher values, while both downshifting and upconversion mechanisms give high CP values.

3.3. Luminescence temperature sensing and predictions by the Judd-Ofelt theory

Fig. 5a shows the temperature dependent upconversion emission spectra of $\text{La}_2\text{O}_2\text{S}:\text{Er}^{3+}/\text{Yb}^{3+}$ from 300 K to 550 K, and in Fig. 5b are given the integrated intensities of Er^{3+} transitions ${}^2\text{H}_{11/2} \rightarrow {}^4\text{I}_{15/2}$ and ${}^4\text{S}_{3/2} \rightarrow {}^4\text{I}_{15/2}$. The emission intensity of the latter drops uniformly with temperature, while the former experiences rise due to the thermal population from the ${}^4\text{S}_{3/2}$ level which competes with the thermal quenching, i.e. non-radiative transitions. The ratio of emissions from the higher ${}^2\text{H}_{11/2}$ (H) to the energetically lower ${}^4\text{S}_{3/2}$ (L) level is given in Fig. 5c together with the fit to the Boltzmann distribution as given in Eq. 1 (with excellent quality). ΔE of 716 cm^{-1} matches the energy difference between these two thermalized levels. Sensitivities obtained by Eqs. 2 and 3 are given in Fig. 5d, giving the value of $1.14\% \text{ K}^{-1}$ at 300 K. $\text{La}_2\text{O}_2\text{S}:\text{Er}^{3+}/\text{Yb}^{3+}$ shows good relative sensitivity values throughout the whole physiologically relevant temperature range (from 300 K to 350 K). The 25 consecutive spectra were obtained at room temperature from which the relative uncertainty in measurement of LIR is estimated: $\sigma_r = 0.2\%$, giving the temperature (see Eq. 4) resolution of 0.17 K at 300 K.

LIR and sensitivities are predicted from the parameters for $\text{La}_2\text{O}_2\text{S}:\text{Er}^{3+}/\text{Yb}^{3+}$ as given in Ref. [43], and the values are compared in

Fig. 5c and d. Additional comparison of parameters is given in Table 3.

4. Conclusion

The green-emitting nanoparticle upconversion phosphor $\text{La}_2\text{O}_2\text{S}:\text{Yb}^{3+}/\text{Er}^{3+}$ with 12% and 2% of Yb^{3+} and Er^{3+} , respectively, was successfully created by the alternated furnace combustion technique that limits the precursors and eliminates the flux of the hazardous gasses. The high output yield and fast production time make it a perspective method for industrial applications. Examined sample was confirmed to have pure hexagonal phase and particle size of less than 100 nm.

The sample shows a typical upconversion fluorescence upon 980 nm excitation. After two energy transfers from Yb^{3+} the Er^{3+} emits two green peaks at 523 nm and 547 nm, and a red peak at 668 nm. Due to the high Yb^{3+} concentration and the energy back-transfer the red peak at 668 nm is of comparable intensity to the green emissions. The emission color purity is of high 99.7% and with 548.6 nm dominant wavelength.

$\text{La}_2\text{O}_2\text{S}:\text{Yb}^{3+}/\text{Er}^{3+}$ nanoparticles are a promising phosphor for luminescence thermometry applications by the Luminescence Intensity Ratio method. The experimentally obtained parameters and sensitivities were compared with those obtained theoretically from the Judd-Ofelt thermometric model. As all of the values are excellently matching this work gives another confirmation that the Judd-Ofelt thermometric model can be used for prediction of the luminescent thermometer sensor performances.

Declaration of Competing Interest

The authors declare that they have no known competing financial interests or personal relationships that could have appeared to influence the work reported in this paper.

Acknowledgments

This research was funded by the Ministry of Education, Science and Technological development of the Republic of Serbia.

References

- [1] F. Auzel, *Compteur quantique par transfert d'énergie entre deux ions de terres rares dans un tungstate mixte et dans un verre*, CR Acad. Sci. Paris 262 (1966) 1016–1019.
- [2] N.M. Idris, M.K. Gnanasammandhan, J. Zhang, P.C. Ho, R. Mahendran, Y. Zhang, In vivo photodynamic therapy using upconversion nanoparticles as remote-controlled nanotransducers, Nat. Med. 18 (2012) 1580–1585, <https://doi.org/10.1038/nm.2933>.
- [3] V. Kumar, A. Pandey, S.K. Swami, O.M. Ntwaeaborwa, H.C. Swart, V. Dutta, Synthesis and characterization of Er^{3+} - Yb^{3+} doped ZnO upconversion nanoparticles for solar cell application, J. Alloy. Compd. 766 (2018) 429–435, <https://doi.org/10.1016/j.jallcom.2018.07.012>.
- [4] Y. Yang, C. Mi, F. Jiao, X. Su, X. Li, L. Liu, J. Zhang, F. Yu, Y. Liu, Y. Mai, A. Novel, Multifunctional upconversion phosphor: $\text{Yb}^{3+}/\text{Er}^{3+}$ codoped La_2S_3 , J. Am. Ceram. Soc. 97 (2014) 1769–1775, <https://doi.org/10.1111/jace.12822>.
- [5] M.D. Dramićanin, Trends in luminescence thermometry, J. Appl. Phys. 128 (2020), 040902, <https://doi.org/10.1063/5.0014825>.
- [6] K. Li, D. Zhu, H. Lian, Up-conversion luminescence and optical temperature sensing properties in novel $\text{KBaY}(\text{MoO}_4)_3:\text{Yb}^{3+},\text{Er}^{3+}$ materials for temperature sensors, J. Alloy. Compd. 816 (2020), 152554, <https://doi.org/10.1016/j.jallcom.2019.152554>.
- [7] Y. Tian, Y. Fu, M. Xing, X. Luo, Upconversion luminescence properties of $\text{Y}_2\text{O}_3:\text{Yb},\text{Er}$ and $\text{Y}_2\text{O}_2\text{S}:\text{Yb},\text{Er}$ nanoparticles prepared by complex precipitation, J. Nanomater. 2015 (2015) 1–7, <https://doi.org/10.1155/2015/573253>.
- [8] M. Runowski, S. Goderski, D. Przybylska, T. Grzyb, S. Lis, I.R. Martín, Sr 2 LuF 7:Yb 3+ –Ho 3+ –Er 3+ upconverting nanoparticles as luminescent thermometers in the first, second, and third biological windows, ACS Appl. Nano Mater. 3 (2020) 6406–6415, <https://doi.org/10.1021/acsnm.0c00839>.
- [9] C. Li, B. Dong, S. Li, C. Song, $\text{Er}^{3+}-\text{Yb}^{3+}$ co-doped silicate glass for optical temperature sensor, Chem. Phys. Lett. 443 (2007) 426–429, <https://doi.org/10.1016/j.cplett.2007.06.081>.
- [10] A. Bril, J.L. Sommerdijk, A.W. de Jager, On the efficiency of $\text{Yb}^{3+}-\text{Er}^{3+}$ activated up-conversion phosphors, J. Electrochem. Soc. 122 (1975) 660–663, <https://doi.org/10.1149/1.2134287>.
- [11] Y. Xu, Y. Wang, L. Shi, L. Xing, X. Tan, Bright white upconversion luminescence in $\text{Ho}^{3+}/\text{Yb}^{3+}/\text{Tm}^{3+}$ triple doped CaWO_4 polycrystals, Opt. Laser Technol. 54 (2013) 50–52, <https://doi.org/10.1016/j.optlastec.2013.05.005>.
- [12] A. Ćirić, S. Stojadinović, Photoluminescence of Gd_2O_3 and $\text{Gd}_2\text{O}_3:\text{Ln}^{3+}$ ($\text{Ln} = \text{Eu}, \text{Er}, \text{Ho}$) formed by plasma electrolytic oxidation of pure gadolinium substrate, Opt. Mater. (2019), 109546, <https://doi.org/10.1016/j.optmat.2019.109546>.
- [13] S. Stojadinović, N. Tadić, R. Vasilčić, Photoluminescence properties of $\text{Er}^{3+}/\text{Yb}^{3+}$ doped ZrO_2 coatings formed by plasma electrolytic oxidation, J. Lumin. 208 (2019) 296–301, <https://doi.org/10.1016/j.jlumin.2018.12.067>.
- [14] D. Gao, X. Zhang, H. Zheng, W. Gao, E. He, $\text{Yb}^{3+}/\text{Er}^{3+}$ codoped $\beta\text{-NaYF}_4$ microrods: synthesis and tuning of multicolor upconversion, J. Alloy. Compd. 554 (2013) 395–399, <https://doi.org/10.1016/j.jallcom.2012.12.010>.
- [15] F. Vetrone, J.-C. Boyer, J.A. Capobianco, A. Speghini, M. Bettinelli, Significance of Yb^{3+} concentration on the upconversion mechanisms in codoped $\text{Y}_2\text{O}_3:\text{Er}^{3+}, \text{Yb}^{3+}$ nanocrystals, J. Appl. Phys. 96 (2004) 661–667, <https://doi.org/10.1063/1.1739523>.
- [16] K. Li, J. Liu, D. Mara, R. Van Deun, Synthesis and up-conversion luminescence properties of a novel $\text{Yb}^{3+}, \text{Er}^{3+}$ co-doped $\text{Ca}_5\text{Mg}_4(\text{VO}_4)_6$ phosphor, J. Alloy. Compd. 737 (2018) 767–773, <https://doi.org/10.1016/j.jallcom.2017.12.171>.
- [17] D. Zhou, D. Li, X. Zhou, W. Xu, X. Chen, D. Liu, Y. Zhu, H. Song, Semiconductor plasmon induced up-conversion enhancement in $\text{mCu}_2-x\text{S}@\text{SiO}_2@Y_2O_3:\text{Yb}^{3+}/\text{Er}^{3+}$ core-shell nanocomposites, ACS Appl. Mater. Interfaces 9 (2017) 35226–35233, <https://doi.org/10.1021/acsaami.7b09850>.
- [18] Y. Gao, F. Huang, H. Lin, J. Zhou, J. Xu, Y. Wang, A novel optical thermometry strategy based on diverse thermal response from two intervalence charge transfer states, Adv. Funct. Mater. 26 (2016) 3139–3145, <https://doi.org/10.1002/adfm.201505332>.
- [19] Q. Dai, H. Song, M. Wang, X. Bai, B. Dong, R. Qin, X. Qu, H. Zhang, Size and concentration effects on the photoluminescence of $\text{La}_2\text{O}_2\text{S}:\text{Eu}^{3+}$ nanocrystals, J. Phys. Chem. C 112 (2008) 19399–19404, <https://doi.org/10.1021/jp808343f>.
- [20] M. Pokhrel, A. kumar Gangadharan, D.K. Sardar, High upconversion quantum yield at low pump threshold in $\text{Er}^{3+}/\text{Yb}^{3+}$ doped $\text{La}_2\text{O}_2\text{S}$ phosphor, Mater. Lett. 99 (2013) 86–89, <https://doi.org/10.1016/j.matlet.2013.02.062>.
- [21] A.M. Kaczmarek, M. Suta, H. Rijckaert, A. Abalymov, I. Van Driessche, A.G. Skirtach, A. Meijerink, P. Van Der Voort, Visible and NIR upconverting $\text{Er}^{3+}-\text{Yb}^{3+}$ + luminescent nanorattles and other hybrid PMO-inorganic structures for in vivo nanothermometry, Adv. Funct. Mater. 30 (2020), 2003101, <https://doi.org/10.1002/adfm.202003101>.

- [22] N. Hakmeh, C. Chlique, O. Merdrignac-Conanec, B. Fan, F. Cheviré, X. Zhang, X. Fan, X. Qiao, Combustion synthesis and up-conversion luminescence of La₂O₂S:Er³⁺,Yb³⁺ nanophosphors, *J. Solid State Chem.* 226 (2015) 255–261, <https://doi.org/10.1016/j.jssc.2015.02.015>.
- [23] W. Chen, *Doped Nanomaterials and Nanodevices: Quantum Dots, Nanowires, Nanotubes, and Applications*, American Scientific Publishers, 2010.
- [24] E. Palo, M. Salomäki, M. Lastusaari, Restraining fluoride loss from NaYF₄:Yb³⁺,Er³⁺ upconverting nanoparticles in aqueous environments using crosslinked poly(acrylic acid)/poly(allylamine hydrochloride) multilayers, *J. Colloid Interface Sci.* 538 (2019) 320–326, <https://doi.org/10.1016/j.jcis.2018.11.094>.
- [25] S. Jiang, P. Zeng, L. Liao, S. Tian, H. Guo, Y. Chen, C. Duan, M. Yin, Optical thermometry based on upconverted luminescence in transparent glass ceramics containing NaYF₄:Yb³⁺/Er³⁺ nanocrystals, *J. Alloy. Compd.* 617 (2014) 538–541, <https://doi.org/10.1016/j.jallcom.2014.08.080>.
- [26] G.A. Kumar, M. Pokhrel, A. Martinez, D.K. Sardar, Synthesis and upconversion spectroscopy of Yb Er doped M 2 O 2 S (M = La, Gd, Y) phosphors, *Sci. Adv. Mater.* 4 (2012) 623–630, <https://doi.org/10.1166/sam.2012.1329>.
- [27] K. Shah, A. Ćirić, K.V.R. Murthy, B.S. Chakrabarty, Investigation of a new way of synthesis for Nano crystallites of La₂O₂S & 1%Ln³⁺ (Ln = Pr, Eu, Tb, Dy, Er) doped La₂O₂S and study their structural and optical properties, *J. Alloy. Compd.* 851 (2021), 156725, <https://doi.org/10.1016/j.jallcom.2020.156725>.
- [28] B.M. Jaffar, H.C. Swart, H.A.A. Seed Ahmed, A. Yousif, R.E. Kroon, Optical properties and stability of Bi doped La₂O₂S, *Opt. Mater.* 95 (2019), 109260, <https://doi.org/10.1016/j.optmat.2019.109260>.
- [29] X. Wang, Q. Zhu, J.-G. Li, Z. Hu, G. Zhu, C. Wang, La₂O₂S:Tm/Yb as a novel phosphor for highly pure near-infrared upconversion luminescence, *Scr. Mater.* 149 (2018) 121–124, <https://doi.org/10.1016/j.scriptamat.2018.02.031>.
- [30] Y. Yang, C. Mi, F. Yu, X. Su, C. Guo, G. Li, J. Zhang, L. Liu, Y. Liu, X. Li, Optical thermometry based on the upconversion fluorescence from Yb³⁺/Er³⁺ codoped La₂O₂S phosphor, *Ceram. Int.* 40 (2014) 9875–9880, <https://doi.org/10.1016/j.ceramint.2014.02.081>.
- [31] L. Yu, F. Li, H. Liu, Fabrication and photoluminescent characteristics of one-dimensional La₂O₂S:Eu³⁺ nanocrystals, *J. Rare Earths.* 31 (2013) 356–359, [https://doi.org/10.1016/S1002-0721\(12\)60285-3](https://doi.org/10.1016/S1002-0721(12)60285-3).
- [32] G. Liu, Q. Zhang, H. Wang, Y. Li, A reddish La₂O₂S-based long-afterglow phosphor with effective absorption in the visible light region, *Mater. Sci. Eng. B* 177 (2012) 316–320, <https://doi.org/10.1016/j.mseb.2011.12.045>.
- [33] J.J. Oh, B.K. Jin, W.J. Chung, D.W. Shin, Y.G. Choi, Wavelength conversion characteristics of Eu³⁺/Yb³⁺-activated La₂O₂S luminophor, *Curr. Appl. Phys.* 11 (2011) S15–S18, <https://doi.org/10.1016/j.cap.2011.01.047>.
- [34] L. Wang, X. Yang, Q. Zhang, B. Song, C. Wong, Luminescence properties of La₂O₂S:Tb³⁺ phosphors and phosphor-embedded polymethylmethacrylate films, *Mater. Des.* 125 (2017) 100–108, <https://doi.org/10.1016/j.matdes.2017.04.003>.
- [35] X. Wang, O.S. Wolfbeis, R.J. Meier, Luminescent probes and sensors for temperature, *Chem. Soc. Rev.* 42 (2013) 7834–7869, <https://doi.org/10.1039/c3cs60102a>.
- [36] C.D.S. Brites, S. Balabhadra, L.D. Carlos, Lanthanide-based thermometers: at the cutting-edge of luminescence thermometry, *Adv. Opt. Mater.* 1801239 (2018), 1801239, <https://doi.org/10.1002/adom.201801239>.
- [37] P.R.N. Childs, J.R. Greenwood, C.A. Long, Review of temperature measurement, *Rev. Sci. Instrum.* 71 (2000) 2959–2978, <https://doi.org/10.1063/1.1305516>.
- [38] M.D. Dramićanin, Sensing temperature via downshifting emissions of lanthanide-doped metal oxides and salts. A review, *Methods Appl. Fluoresc.* 4 (2016), 042001, <https://doi.org/10.1088/2050-6120/4/4/042001>.
- [39] A. Ćirić, S. Stojadinović, M.D. Dramićanin, An extension of the Judd-Ofelt theory to the field of lanthanide thermometry, *J. Lumin.* 216 (2019), 116749, <https://doi.org/10.1016/j.jlumin.2019.116749>.
- [40] M. Suta, Ž. Antić, V. Đorđević, S. Kuzman, M.D. Dramićanin, A. Meijerink, Making Nd³⁺ a sensitive luminescent thermometer for physiological temperatures—an account of pitfalls in Boltzmann thermometry, *Nanomaterials* 10 (2020) 543, <https://doi.org/10.3390/nano10030543>.
- [41] M. Sekulić, V. Đorđević, Z. Ristić, M. Medić, M.D. Dramićanin, Highly sensitive dual self-referencing temperature readout from the Mn⁴⁺/Ho³⁺ binary luminescence thermometry probe, *Adv. Opt. Mater.* 6 (2018), 1800552, <https://doi.org/10.1002/adom.201800552>.
- [42] M. Suta, A. Meijerink, A theoretical framework for ratiometric single ion luminescent thermometers—thermodynamic and kinetic guidelines for optimized performance, *Adv. Theory Simul.* 3 (2020), 2000176, <https://doi.org/10.1002/adts.202000176>.
- [43] A. Ćirić, T. Gavrilović, M.D. Dramićanin, Luminescence intensity ratio thermometry with Er³⁺: performance overview, *Crystals* 11 (2021) 189, <https://doi.org/10.3390/cryst11020189>.
- [44] A. Ćirić, I. Zeković, M. Medić, Ž. Antić, M.D. Dramićanin, Judd-Ofelt modelling of the dual-excited single band ratiometric luminescence thermometry, *J. Lumin.* 225 (2020), 117369, <https://doi.org/10.1016/j.jlumin.2020.117369>.
- [45] B.G. Wybourne, The fascination of the rare earths—then, now and in the future, *J. Alloy. Compd.* 380 (2004) 96–100, <https://doi.org/10.1016/j.jallcom.2004.03.034>.
- [46] A. Ćirić, J. Aleksić, T. Barudžija, Ž. Antić, V. Đorđević, M. Medić, J. Periša, I. Zeković, M. Mitrić, M.D. Dramićanin, Comparison of three ratiometric temperature readings from the Er³⁺ upconversion emission, *Nanomaterials* 10 (2020) 1–10, <https://doi.org/10.3390/nano10040627>.
- [47] A. Ćirić, S. Stojadinović, Structural and photoluminescence properties of Y₂O₃ and Y₂O₃:Ln³⁺ (Ln = Eu, Er, Ho) films synthesized by plasma electrolytic oxidation of yttrium substrate, *J. Lumin.* 217 (2020), 116762, <https://doi.org/10.1016/j.jlumin.2019.116762>.
- [48] F. Auzel, Upconversion and anti-stokes processes with f and d ions in solids, *Chem. Rev.* 104 (2004) 139–174, <https://doi.org/10.1021/cr020357g>.
- [49] H. Huang, H. Zhou, J. Zhou, T. Wang, D. Huang, Y. Wu, L. Sun, G. Zhou, J. Zhan, J. Hu, Enhanced anti-stokes luminescence in LaNbO₄:Ln³⁺ (Ln³⁺ = Yb³⁺, Er³⁺ /Ho³⁺ /Tm³⁺) with abundant color, *RSC Adv.* 7 (2017) 16777–16786, <https://doi.org/10.1039/C6RA28592A>.
- [50] Q. Pan, D. Yang, S. Kang, J. Qiu, G. Dong, Regulating mid-infrared to visible fluorescence in monodispersed Er³⁺-doped La₂O₂S (La₂O₂SO₄) nanocrystals by phase modulation, *Sci. Rep.* 6 (2016) 37141, <https://doi.org/10.1038/srep37141>.
- [51] H.M. Noh, H.K. Yang, B.K. Moon, B.C. Choi, J.H. Jeong, H. Choi, J.H. Kim, Effect of Yb³⁺ concentrations on the upconversion luminescence properties of ZrO₂:Er³⁺,Yb³⁺ phosphors, *Jpn. J. Appl. Phys.* 52 (2013) 01AM02, <https://doi.org/10.7567/JJAP.52.01AM02>.
- [52] S. Stojadinović, N. Tadić, R. Vasilčić, Down-conversion photoluminescence of ZrO₂:Er³⁺ coatings formed by plasma electrolytic oxidation, *Mater. Lett.* 219 (2018) 251–255, <https://doi.org/10.1016/j.matlet.2018.02.126>.
- [53] A. Ćirić, S. Stojadinović, M. Sekulić, M.D. Dramićanin, JOES: An application software for Judd-Ofelt analysis from Eu³⁺ emission spectra, *J. Lumin.* 205 (2019) 351–356, <https://doi.org/10.1016/j.jlumin.2018.09.048>.
- [54] A. Ćirić, S. Stojadinović, Photoluminescence of ZrO₂:Gd³⁺ and ZrO₂:Dy³⁺ coatings formed by the plasma electrolytic oxidation, *J. Alloy. Compd.* 832 (2020), 154907, <https://doi.org/10.1016/j.jallcom.2020.154907>.

Exploring Lanthanum Sulphide Characteristics For Its Physical Properties

Kavita R. Kolte, Kevil Shah, B.S. Chakrabarty

Abstract: The rare earth Lanthanum sulphide (La_2S_3) complex has been synthesized and characterized by X-ray diffraction (XRD), Optical Microscopy, Fourier transform infrared spectroscopy (FTIR) and Photo-luminescent measurements techniques. The synthesized samples have been doped with Europium (Eu) and Terbium (Tb) to study its physical properties. Under the photo excitation, these complexes exhibited characteristic emission similar to its metal ions. These investigations indicate that synthesized complexes have different energy levels than the doped lanthanide sulphide complexes. Presented data and detail examination of the synthesized complexes shows better characteristics than conventional Lanthanum sulphide. The properties of the undoped Lanthanum sulphide complex and doped samples were studied for exploring its possible thermoelectric applications.

Index Terms: Europium (Eu), Lanthanum sulphide (La_2S_3), Photoluminescence (PL), Terbium (Tb), Thermoelectric

1 INTRODUCTION

It is well known that the rare earth elements have interesting physical and chemical properties. The excited states of Europium and Terbium complexes have strong fluorescence emission, large Stokes' shifts, narrow emission profiles and long fluorescence lifetimes [1–4]. These have been widely used in many aspects for various physical devices [5–11]. Conversely, the application of lanthanide based luminescence suffers from serious draw-backs: The low absorption coefficients because of the f–f electronic transitions are forbidden and the efficient non-radioactive deactivation of their excited states by OAH oscillators such as water [12]. These evident problems can be avoided for the lanthanide complexes using mentioned strategies (I) addition of effective photo-sensitized ligands, (II) vibrational frequency suppression by high vibrational CAH & OAH bonds [13] and (III) forming asymmetric co-ordination structures for better transitions of electric dipoles [14,15]. Using these pathways, the lanthanide ions serve as an antenna or sensitizer. Described processes of these complexes will absorb the excitation light energy and transfer the energy from its lowest triplet state energy level (T1) to the resonance level of lanthanides [16]. Different types of Ligands like the macro-cyclic and the macro-bicyclic have been extensively used for these purposes [17–20]. This type of ligands have drawn much attention in present times, mainly due to possession of spheroidal cavities and binding sites that are hard.

Hence they stabilize its complexes and shield the encapsulated ion from interaction with the surroundings [21]. Among these numerous compounds which have demonstrated their potential use in many applications [22–24], amide type compound are more popular in preparing the lanthanide complexes because they possess strong luminescent properties. It is expected that the amide type compound, which are flexible in structure and have terminal group effects [25], will shield the encapsulated lanthanide ion from interaction with the surroundings effectively, and thus help to achieve strong luminescent properties. In the present work, lanthanum sulphide complexes have been synthesized from the lanthanide nitrates using a novel ligand, 2-4-tetradecyloxybenzylidene carbathioamide, and studied the luminescent characteristics after doping this complex with Europium (Eu) and terbium (Tb). The complexes have been studied by XRD and FTIR results. Under the photo excitation, the Eu & Tb doped complexes which exhibit the characteristic emission of corresponding lanthanide ions have been correlated with physical properties of the lanthanide complexes.

2 Materials and Methods

2.1 Experimental Characterization

4-n-tetradecyloxybenzaldehyde [26] and 2-4-tetradecyloxy benzylidene thiosemicarbazide [27,28] were as prepared according to the literature methods. Other chemicals were obtained from commercial sources and used without further purification. The La^{+3} ion was determined by EDTA titration using xylenol-orange as an indicator. Carbon, nitrogen and hydrogen were determined using an Elemental Vario EL. FTIR was recorded in the $4000 - 200 \text{ cm}^{-1}$ range using KBr pellets on a Nicolet Nexus 670 FTIR spectrometer. XRD measurements were carried out on Philips Xpert MPD X-Ray Diffractometer having 2θ range from 5 to 70. Photoluminescence Spectra were obtained on SHIMADZU RF 6000 spectrofluorophotometer equipped with Xenon lamp as an excitation source at room temperature. ^1H NMR spectra were measured on a Varian Mercury 300 spectrometer in d-DMSO solution, with TMS as internal standard. Fluorescence quantum yields were determined by using eosin solution ($U = 0.190$ in water) as standard for the Eu^{3+} complex, and quinine sulphate ($U = 0.558$ in $0.5 \text{ mol cm}^{-3} \text{ H}_2\text{SO}_4$) for the Tb^{3+} complex.

• Kavita R kolte is currently pursuing doctoral degree in Applied Physics Department, Faculty of Tech. & Engg., The M.S. University of Baroda, India.

E-mail: kavitaKolte@yahoo.co.in

• B.S. Chakrabarty is currently working as Head of the Department in Applied Physics Department, Faculty of Tech. & Engg., The M.S. University of Baroda, India.

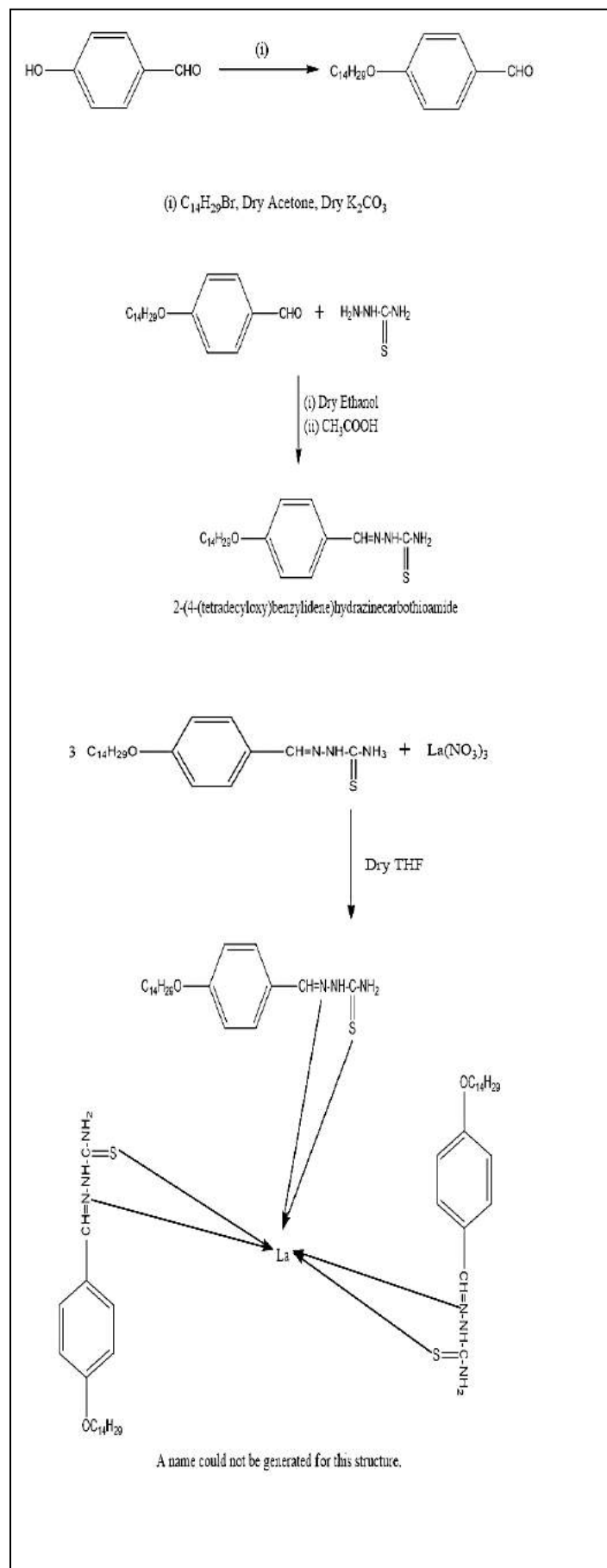
E-mail: bschakrabarty@rediffmail.com

2.2 Procedure

(a) Synthesis of 4-n-Tetradecyloxybenzaldehydes: These were synthesized by alkylation of 4-hydroxybenzaldehyde using the reported method of Vyas and Shah [31]. 0.1 Mole 4-Hydroxybenzaldehyde, 0.15 mole of anhydrous K_2CO_3 and 0.15 mole of corresponding 1-bromoalkane were added to 60 ml dry acetone. The mixture was refluxed on water bath for 10 to 12 hours. Completion of the reaction was checked by TLC (70% Ethyl acetate-hexane). The whole mass was added to cold water and was extracted with ethers. Ether extract washed with 5% solution of NaOH(aq) (25 ml x 3), water (25 ml x 3), brine and was then dried over anhydrous Na_2SO_4 . Reaction mass was purified by column chromatography using silica (100-200 mesh size) and 10% ethyl acetate-hexane as eluent furnished the product. Yield: 59-64%.

(b) 4-n-tetradecyloxybenzylidene thiosemicarbazide synthesis : The corresponding 0.1 Mole of thiosemicarbazide was dissolved in dry ethanol. The solution was added drop wise to the round bottom flask containing 0.1mole of 4-n-decyloxybenzaldehydes [a], which was previously dissolved in ethanol and few drops of acetic acid. After mixing them the content of the flask heated under reflux for 6-8 hours. The crude product was repeatedly crystallized from the ethanol. Yield in general is 40-45% and M.P is 92–94 °C. The Elemental Analysis results for $C_{22}H_{37}ON_3S$ were found to be: C- 67.5; H-9.4; N- 10.74 S- 8.18 whereas the Observed results are found to be: C- 67.61; H- 9.36; N- 10.71, S- 8.16%. ¹H NMR spectrum (400 MHz) results are: δ 0.88 (t,3H,-CH₃), 1.2-1.4 (m, 22H, 11 x -CH₂-), 1.76(quant. 2H, Ar-O-C-CH₂-) 3.90-4.08 (m, 2H, of Ar-O-CH₂-), 7.06 (m, 2H of ArH), 7.83 (d, 2H, ArH), 8.54 (s, 1H-CH=N-), 2.0(-NH), 8.56 (-NH₂).

(c) Synthesis of the lanthanide complex [Tris {4-n-Tetradecyloxybenzylidene thiosemicarbazide} lanthanum]: A mixture of the 4-n-tetradecyloxybenzylidene thiosemicarbazide ligand (0.6 mmol) in dry MeOH solvent mixture was stirred for 10 min at room temperature, following which a dry THF solution of $La(NO_3)_3 \cdot 6H_2O$ (0.2 mmol) was added drop wise, and the reaction mixture was stirred subsequently for 48h. The precipitates formed were filtered off, washed with MeOH, dried over anhydrous Na_2SO_4 and purified by ethanol. After the successful synthesis of Lanthanum sulphide complex as shown in step (c), a further procedure was followed for preparing doped Lanthanide complex. $Eu(NO_3)_3 \cdot 6H_2O$ (0.01 mmol) and $Tb(NO_3)_3 \cdot 6H_2O$ (0.01 mmol) were added as dopant sources respectively during the procedure shown in step (c) to obtain the doped Lanthanum sulphide complexes. Analytical data and values of the complexes are given. All the complexes are near to white colour powders and stable in air.



3 RESULT AND DISCUSSION

Experiment and characterization has been performed by standard instrumental setup and procedure as given in previous section for the further discuss.

3.1 Infrared spectra

IR peaks as shown in Fig 2 for the complexes are reported here. The complexes have IR spectra, of which the characteristic bands have similar shifts (see Table 1), suggesting a similar coordination structure of complexes.

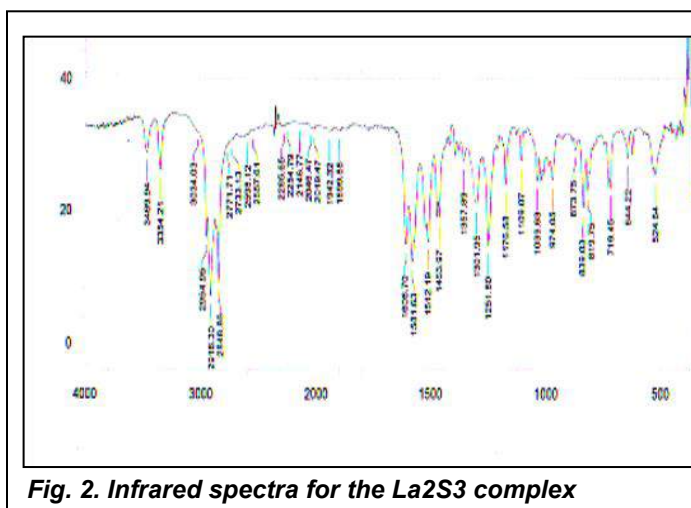


Fig. 2. Infrared spectra for the La₂S₃ complex

The IR spectrum of the free ligand L shows bands at 3469(N-H), 2916(C-H), 1606(CH=N), 1581(C=N), 314(Ln-N), 227(Ln-S), which are attributable to the stretch vibration of the azomethine group [CH=N] and (C=N), respectively. In the complexes, the low-energy band remains unchanged, but the high-energy band red shifts to about 1606 cm⁻¹ ($\nu = 38$ cm⁻¹) as compared to its counterpart for the "free" ligand, thus indicating that only the nitrogen atom of [CH=N] takes part in coordination to the lanthanide ions. The characteristic frequencies of the coordinating nitrate groups (ν_{2v}) appear at ca 1484 cm⁻¹ (ν_1), 1300 cm⁻¹ (ν_4), 1045 cm⁻¹ (ν_2) and 812 cm⁻¹ (ν_3), and the difference between two strongest absorptions (ν_1 and ν_4) of the nitrate groups is about 180 cm⁻¹, clearly establishing that the NO₃⁻ groups in the solid complexes coordinate to the lanthanide ion as bidentate ligands [30,31]. Additionally, no bands at 1380, 820 and 720 cm⁻¹ in the spectra of complexes indicates that free nitrate groups (D_{3h}) are absent. In addition, broad bands at ca. 3395 cm⁻¹ indicate that water molecules are existent in the complexes, confirming the analysis results.

3.2 X-Ray Diffraction spectra

The XRD patterns are shown in Fig. 3 for La₂S₃ powders and found that samples can be indexed as cubic phase (JCPDS 25-1041). These XRD patterns prepared by the describe method of lanthanide complex consist of γ -La₂S₃. The results show that the samples have a better crystallization and resembles to the lanthanum structure having γ phase.

TABLE 1

FTIR PEAKS OF LANTHANUM SULPHIDE COMPLEX

Compounds	N-H	(CH=N)	C=N	C-H	La-N	La-S
Lanthanum Sulphide Complex	3469	1606	1581	2916	314	227
Eu Doped Lanthanum Sulphide Complex	3470	1605	1582	2915	315	225
Tb Doped Lanthanum Sulphide Complex	3468	1604	1580	2914	316	226

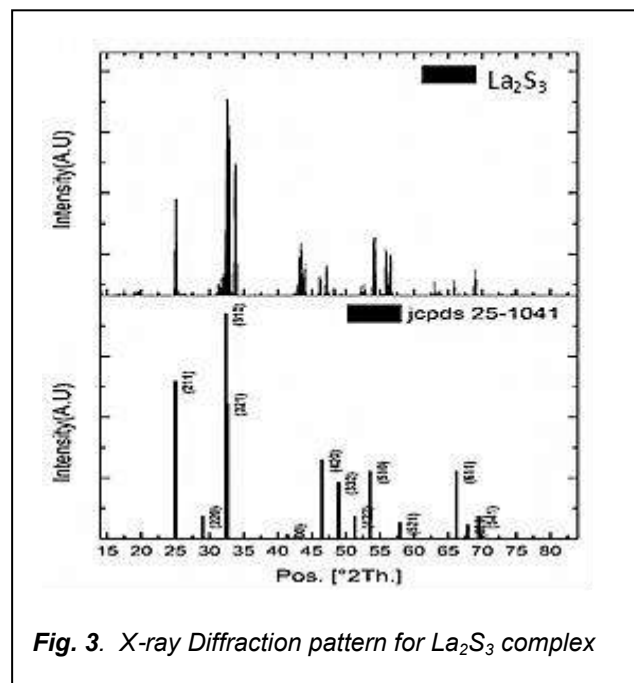


Fig. 3. X-ray Diffraction pattern for La₂S₃ complex

3.3 Morphology

As shown in Fig. 4 morphological image of doped La₂S₃ of prepared samples consist of mainly mixed particles as seen from the images. In accordance with XRD peaks and analysis further it is seen that the phase of La₂S₃ is in the stoichiometric composition. Based on the morphological results, the better atmosphere condition can be investigated to find the effect of decomposition temperature on the powder preparation.



Fig. 4. (a) Optical image of doped Lanthanum sulphide complex (b) Magnified image of doped Lanthanum sulphide complex

3.4 Photoluminescence

The luminescent properties of the Lanthanum sulphide complex and doped Lanthanum sulphide complexes with Eu and Tb were investigated. The excitation and emission spectra were recorded at room temperature under laboratory conditions. The Fig. 5 shows properties for Eu & Tb doped Lanthanum sulphide complexes. For the undoped sample, there is no significant change in emission peaks. For the doped samples the excitation wavelength is found to be 246 nm. Under this excitation, the strong emission peaks for doped sample are observed at 398 nm and 470 nm respectively. The excited state is independent of the doped complexes which is similar to other lanthanide structures.

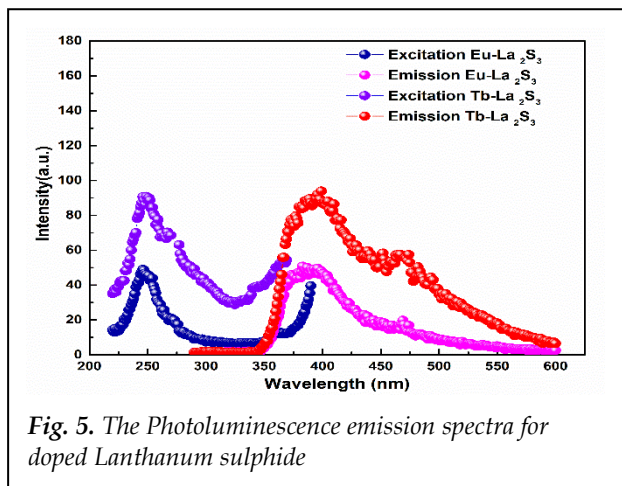


Fig. 5. The Photoluminescence emission spectra for doped Lanthanum sulphide

Further, the thermoelectric properties for the γ -phase of the doped Lanthanide were similar with reported materials. It is interesting to characterize temperature dependent analysis for its behavioural understanding. The thermoelectric measurement in the temperature range of 250 K to 800 K are found to have the values of $30 \mu\text{V K}^{-1}$ to $80 \mu\text{V K}^{-1}$ for lanthanide complex which are in accordance with reported values by other researchers [Michihiro ohta, et.al 2005].

4 CONCLUSION

In the present results and discussion, the novel Lanthanum sulphide with doped Eu and Tb can form a stable solid complex. These Lanthanide complexes are confirmed by XRD pattern and IR spectra of as prepared and doped samples. It is noteworthy that the characterization of these complexes demonstrates stoichiometric composition. Thus, the lanthanum complex could be effectively synthesized and characterized by instrumental analysis. The luminescent properties of the Eu and Tb doped complexes were investigated and they exhibit the characteristic luminescence of Europium and Terbium ions. The state of energy level indicates that the doped Lanthanide matches better to the energy level of the prepared lanthanide complex. It indicates that the excited state of the efficient ions can absorb and transfer energy to the lanthanide complexes. Also, thermoelectric exploration shows that these complexes can be used for possible thermo power applications.

ACKNOWLEDGMENT

I would like to thank The M. S. University of Baroda for their support in carrying out this work.

REFERENCES

- [1] W. Zheng, S.J. Li, C.H. Li, Y.X. Zheng, X.Z. You, J. Lumin. 146 (2014) 544.
- [2] C.J. Gao, A.M. Kirillov, W. Dou, X.L. Tang, L.L. Liu, X.H. Yan, Y.J. Xie, P.X. Zang, W.S. Liu, Y. Tang, Inorg. Chem. 53 (2014) 935.
- [3] T.Z. Miao, Z. Zhang, W.X. Feng, P.Y. Su, H.N. Feng, X.Q. Lu, D.D. Fan, W.K. Wong, R.A. Jones, C.Y. Su, Spectrochim. Acta A 132 (2014) 205.
- [4] L.F. Marques, C.C. Correa, H.C. Garcia, T.M. Francisco, S.J.L. Ribeiro, J.D.L. Dutra, R.O. Freire, F.C. Machado, J. Lumin. 148 (2014) 307.
- [5] J.D. Xu, T.M. Comeillie, E.G. Moore, G.L. Law, N.G. Butlin, K.N. Raymond, J. Am. Chem. Soc. 133 (2011) 19900.
- [6] J. Shi, Y.J. Hou, W.Y. Chu, X.H. Shi, H.Q. Gu, B.L. Wang, Z.Z. Sun, Inorg. Chem. 52 (2013) 5013.
- [7] J.Y. Li, H.F. Li, P.F. Yan, G.F. Hou, G.M. Li, Inorg. Chem. 51 (2012) 5050.
- [8] J.-C.G. Bünzli, Chem. Rev. 110 (2010) 2729.
- [9] J. Pauli, K. Licha, J. Berkemeyer, M. Grabolle, M. Spieles, N. Wegner, P. Welker, U. Resch-genger, Bioconjugate Chem. 24 (2013) 1174.
- [10] S. Sumalekshmy, C.J. Fahrni, Chem. Mater. 23 (2011) 483.
- [11] X.Q. Zhao, B. Zhao, S. Wei, P. Cheng, Inorg. Chem. 48 (2009) 11048.
- [12] S.W. Magennis, S. Parsons, Z. Pikramenou, Chem. Eur. J. 8 (2002) 5761.
- [13] Y. Hasegawa, Y. Kimura, K. Murakoshi, Y. Wada, J.H. Kim, N. Nakashima, T. Yamanaka, S. Yanagida, J. Phys. Chem. 100 (1996) 10201.
- [14] Y. Hasegawa, M. Yamamuro, Y. Wada, N. Kanehisa, Y. Kai, S. Yanagida, J. Phys. Chem. A 107 (2003) 1697.
- [15] K. Miyata, T. Nakagawa, R. Kawakami, Y. Kita, K. Sugimoto, T. Nakashima, T. Harada, T. Kawai, Y. Hasegawa, Chem. Eur. J. 17 (2011) 521.
- [16] G.F. de Sá, O.L. Malta, D.C. de Mello, A.M. Simas, R.L. Longo, P.A. Santa-Cruz, E.F. da Silva, Coord. Chem. Rev. 196 (2000) 165.
- [17] J.M. Lehn, J.B. Regnouf de Vains, Helv. Chim. Acta 75 (1992) 1221.
- [18] V.M. Mukkala, J.J. Kankare, Helv. Chim. Acta 75 (1992) 1578.
- [19] B. Alpha, J.M. Lehn, G. Mathgis, Angew. Chem. Int. Ed. Engl. 26 (1987) 266.
- [20] V. Balzani, E. Berghmans, J.M. Lehn, N. Sabbatini, A. Mecai, R. Therorode, R. Ziessel, Helv. Chim. Acta 73 (1990) 2083.
- [21] N. Fatin-Rouge, E. Tóth, D. Perret, R.H. Backer, A.E. Merbach, J.C.G. Bünzli, J. Am. Chem. Soc. 122 (2000) 10810.
- [22] D.L. Reger, R.F. Semeniuc, M.D. Smith, Inorg. Chem. 42 (2003) 8137.
- [23] Q. Wang, X.H. Yan, W.S. Liu, M.Y. Tan, Y. Tang, J. Fluoresc. 20 (2010) 493.
- [24] X.H. Yan, Z.H. Cai, C.L. Yi, W.S. Liu, M.Y. Tan, Y. Tang, Inorg. Chem. 50 (2011) 2346.
- [25] B. Tümmler, G. Maass, F. Vögtle, J. Am. Chem. Soc. 101 (1979) 2588.

- [26] Vyas, G. N., Shah, N. M., *Org. Syn. Coll. Vol. IV*, (Revised-edition of annual volume 30-39, John Wiley and Sons Inc., New York, p. 836 (1963).
- [27] Dave, J. S. and Patel, P. R., *Mol. Cryst.*, 2, 115 (1966).
- [28] K. Nakagawa, K. Amita, H. Mizuno, Y. Inoue, T. Hakushi, *Bull. Chem. Soc. Jpn.* 60 (6) (1987) 2037.
- [29] W.J. Greary, *Coord. Chem. Rev.* 7 (1971) 81.
- [30] W. Camall, S. Siegel, J. Ferrano, B. Tani, E. Gebert, *Inorg. Chem.* 12 (1973) 560.
- [31] K. Nakamoto, *Infrared and Raman Spectra of Inorganic and Coordination Compounds*, fifth ed., Wiley, New York, 1997.

Synthesis And Optical Properties Of Zirconia (ZrO₂)-Polyacrylicacid (PAA) Nanocomposites

Dhaval Hirani, Kevil Shah, B. S. Chakrabarty

Abstract: In this paper, we present the synthesis of ZrO₂ (Zirconia) nanoparticles by hydrothermal method and the synthesis of Zirconia (ZrO₂)-polyacrylicacid (PAA) nanocomposite. The structural, morphological and optical properties of ZrO₂-polyacrylicacid nanocomposite have been investigated through XRD, SEM, EDX, FTIR, UV-Vis absorption and photoluminescence (PL) spectroscopy. X-ray diffraction (XRD) spectra confirms the formation of ZrO₂ and crystallinity of samples. SEM and EDX performed the surface morphological and elemental characterizations. Scanning electron microscope (SEM) shows the irregular morphology of the particles and chunks of ZrO₂ distributed throughout the sample. Energy Dispersive X-ray (EDX) spectroscopy and Fourier transform infrared (FTIR) spectra confirms the formation of ZrO₂ in crystalline phase. Ultraviolet-visible (UV-Vis) spectroscopy and photoluminescence (PL) spectroscopy gives optical properties. Absorption spectra shows a well-defined peak in absorbance curve. Photoluminescence (PL) spectra exhibits an additional emission peak may be due to interstitial defect created by ZrO₂ in the polyacrylicacid film.

Index Terms: nanocomposites, hydrothermal, optical property, polyacrylicacid (PAA), zirconia (ZrO₂), UV-Vis spectroscopy, Photoluminescence (PL)

1 INTRODUCTION

Nanocomposite is a mixture of different component materials, in which at least one being of nanometer scale. Such materials may display combined features of all components or quite new properties resulting from mutual interactions between components. Organic-inorganic polymer composites have recently found wide technological applications. In the last years, a special interest has been focused on nanocomposites based on polymer networks involving nanoparticles being characterized by different electric, magnetic or optical features. Different kinds of materials, among which are sulfides, organic compounds and oxides nanocrystals, have been proposed as nano-fillers in these composites [1, 2]. Polymer nanocomposites are materials in which nanoscopic inorganic particles are dispersed in an organic polymer matrix in order to improve the performance properties of the polymer. Polymer nanocomposites represent a new alternative to conventionally filled polymers [3]. Because of their nanometer sizes, filler dispersion nanocomposites exhibit markedly improved properties when compared to the pure polymers or their traditional composites [4]. Nano-size zirconia has attracted much attention due to its specific optical and electrical properties as well as other potential applications in transparent optical devices, electro- chemical capacitor electrodes, oxygen sensors, fuel cells, catalysts and advanced ceramics [5]. ZrO₂ is a technologically important material due to its superior hardness, high refractive index, optical transparency, chemical stability, photothermal stability, high thermal expansion coefficient, low thermal conductivity, high thermomechanical resistance and high corrosion resistance [6]. These unique properties of ZrO₂ have led to their widespread applications in the fields of optical [7], structural materials, solid-state electrolytes, gas-sensing, thermal barriers coatings [8], corrosion-resistant, catalytic [9].

In present paper, ZrO₂-polyacrylicacid nanocomposites were prepared by hydrothermally synthesised ZrO₂ was mixed with polyacrylicacid. The purpose of introducing ZrO₂ with polyacrylicacid was to enhance its optical properties as ZrO₂ has better optical properties.

2 EXPERIMENTAL PART

2.1 Materials

Acrylicacid monomer was purchased from Merck chemicals. Zirconium oxichloride was purchased from Sigma-Aldrich. All chemicals used are of analytical grade and used as obtained.

2.2 Synthesis of ZrO₂ by hydrothermal method

In which zirconium oxichloride and acrylicacid were initial chemicals. The ZrO₂ was prepared by hydrolysis of zirconium oxichloride and then drop wise addition of ammonium hydroxide into the above solution to make pH=10 of the solution. Add hydrogen peroxide (20% volume of solution) to make 50 ml of solution which kept under vigorous stirring at room temperature. The ZrO₂ nanoparticles were obtained by transferring the solution into Teflon lined autoclave at 160 °C for 24h. Then, wash the solution for 2-3 times by ethanol and distilled water and was calcinated in oven at 100 °C for 1h.

2.3 Preparation of ZrO₂-Polyacrylicacid nanocomposites

ZrO₂-Polyacrylicacid nanocomposite was prepared by introducing hydrothermally synthesized ZrO₂ to the acrylicacid (monomer) using oven as a conventional polymerization technique [10]. Thus, synthesized ZrO₂ with various concentrations (0.1 & 0.5 mol%) were ultrasonicated with acrylicacid. With drop wise addition of potassium persulfate (KPS) as an activator, initiate the polymerization. And the solution kept in the oven for 20 min. at 120 °C for desired nanocomposites. The preparation of film can be done by deep coating method [11].

2.4 Characterization technique

As prepared and calcinated ZrO₂ nanopowder and ZrO₂-polyacrylicacid (PAA) characterised through various techniques, namely XRD, SEM, EDX, FTIR, Uv-vis absorption spectroscopy and photoluminescence studies. The crystalline nature and phase purity of ZrO₂ nanoparticles was recorded by Bruker D8 Advance X-ray diffractometer. Surface morphology and grain size distribution of samples is analysed

- Dhaval Hirani is currently pursuing doctoral degree in Applied Physics Department, Faculty of Tech. & Engg., The M.S. University of Baroda, India.
PH- 9909516712. E-mail: dhaval.hirani1602@gmail.com
- B.S. Chakrabarty is currently working as Head of the Department in Applied Physics Department, Faculty of Tech. & Engg., The M.S. University of Baroda, India.
E-mail: bschakrabarty@rediffmail.com

through JEOL make Model JSM 5810 LV scanning electron microscope. Nicolet iS10 FTIR Spectrometer of Thermo Scientific in the wave number region between 4000–400 cm^{-1} studies the quality and occurrence of functional group in ZrO_2 -polyacrylicacid nanocomposites. Evolution 600 UV-Vis Spectrometer of Thermo Scientific recorded the UV-Vis absorbance spectra and Photoluminescence spectra were recorded using Horiba Jobin Yvon make Fluoromax-4 Spectrophotometer at room temperature with excitation wavelength 300 nm.

3 RESULTS AND DISCUSSION

3.1 X-ray Diffraction (XRD)

The XRD patterns were recorded on Bruker D8 Advance X-

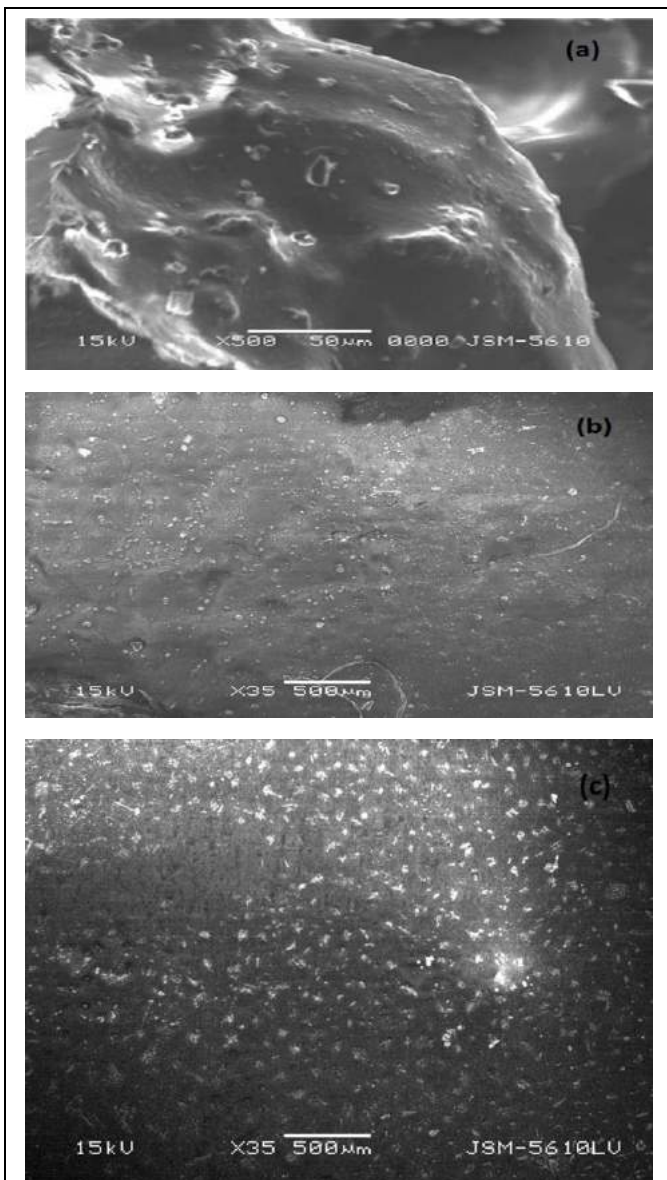


Fig. 2. SEM images of ZrO_2 -polyacrylicacid nanocomposites (a) pure polyacrylicacid (b) 0.1% ZrO_2 -polyacrylicacid & (c) 0.5% ZrO_2 -polyacrylicacid nanocomposites.

ray diffractometer in 2θ range of 20° to 90° at room temperature with a least count of 0.05° . The 2θ values are mentioned in degrees.

In order to investigate the crystallization process of zirconia, Fig. 1. shows XRD of as-prepared products. This figure indicates that a mixture of monoclinic (m) and tetragonal (t) phases of zirconia was obtained. The distinguishing characteristic peaks occurred at 2θ 30.161, 35.021, 50.371 and 60.021 for (1 1 1), (2 0 0), (2 2 0) and (3 1 1) reflections respectively. This is very close to the values in the literature (JCPDS no. 003-0640).

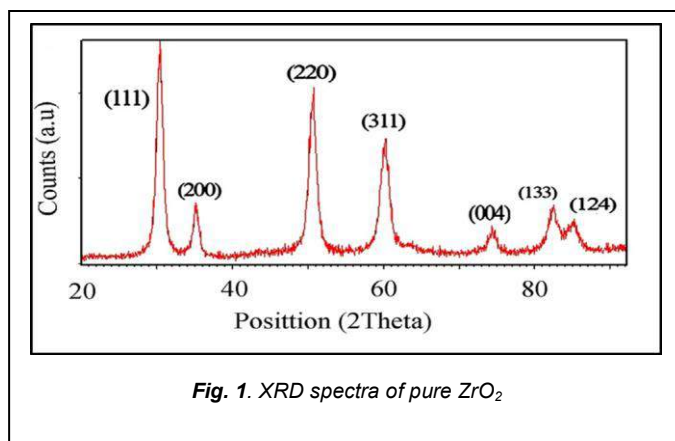


Fig. 1. XRD spectra of pure ZrO_2

The crystallite size of the as-prepared ZrO_2 calculated with the Scherer formula, was found 12.1 nm and XRD results showed that the phase of ZrO_2 nanoparticles were monoclinic and tetragonal.

3.2 SEM Analysis

Morphological analysis of the samples was done by JEOL make Model JSM 5810 LV scanning electron microscope. SEM images of pure acrylicacid shown in Fig. 2. (a) and two samples of ZrO_2 -polyacrylicacid nanocomposites having ZrO_2 with 0.1% and 0.5% of concentrations are shown in Fig. 2. (b-c) respectively. The nanosized particles can be observed from SEM images. It is clear that the chunks of ZrO_2 material were spread homogeneously throughout whole sample and no change in morphology is observed due to ZrO_2 doping.

3.3 Energy Dispersive X-ray spectroscopy

The Energy Dispersive X-ray (EDX) spectroscopy is an analytical technique used for the elemental analysis of a sample, which identifies the elemental composition of materials imaged in a scanning electron microscope. And Fig. 3 (a-b) reveal that the ZrO_2 -polyacrylicacid nanocomposites are composed of C, O and Zr elements, which is in good agreement with the used chemicals. The elemental Weight% and Atomic% of C, O and Zr for Fig. 3 (a) is 24.03, 74.49, 1.48 and 29.99, 69.77, 0.24 respectively. And elemental Weight% and Atomic% of C, O and Zr for Fig. 3 (b) is 18.22, 79.44, 2.34 and 23.31, 76.30, 0.39 respectively.

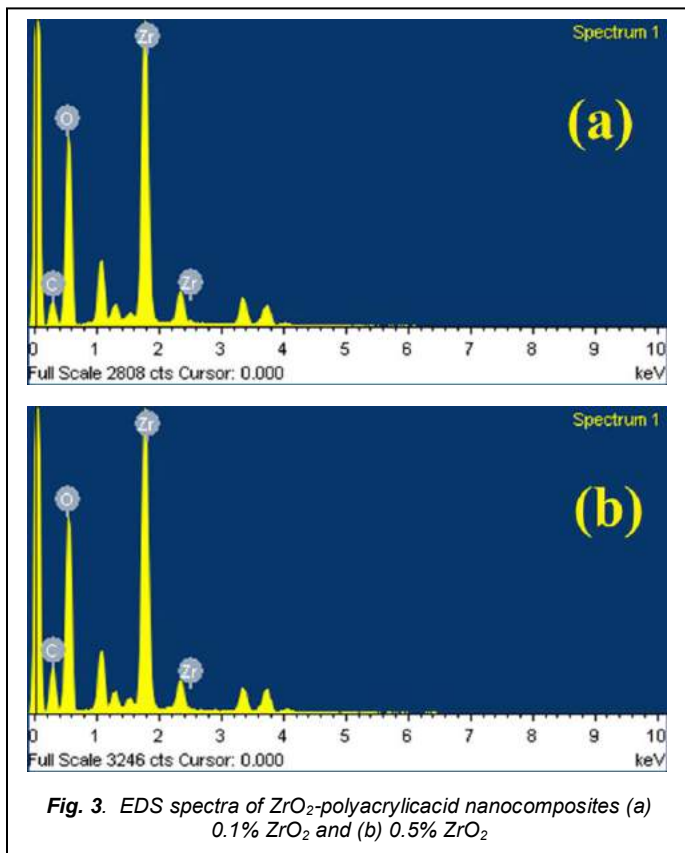


Fig. 3. EDS spectra of ZrO_2 -polyacrylicacid nanocomposites (a) 0.1% ZrO_2 and (b) 0.5% ZrO_2

3.4 Fourier transform infrared (FTIR) Spectroscopy

FTIR spectrographs were recorded by a Nicolet iS10 FTIR Spectrometer of Thermo Scientific in the wave number region between 4000–400 cm^{-1} studies the quality and occurrence of functional group in ZrO_2 - polyacrylicacid nanocomposites. Fig. 4 (a-b) shows the FTIR spectrographs of pure polyacrylicacid and ZrO_2 -polyacrylicacid nanocomposite, which shows enhanced optical property as the transmittance of ZrO_2 -polyacrylicacid nanocomposites has higher value with compare to pure polyacrylicacid.

3.5 Ultraviolet-visible (UV-Vis) Spectroscopy

The absorption spectra were recorded by Evolution 600 UV-Vis Spectrometer of Thermo Scientific. The spectra were taken

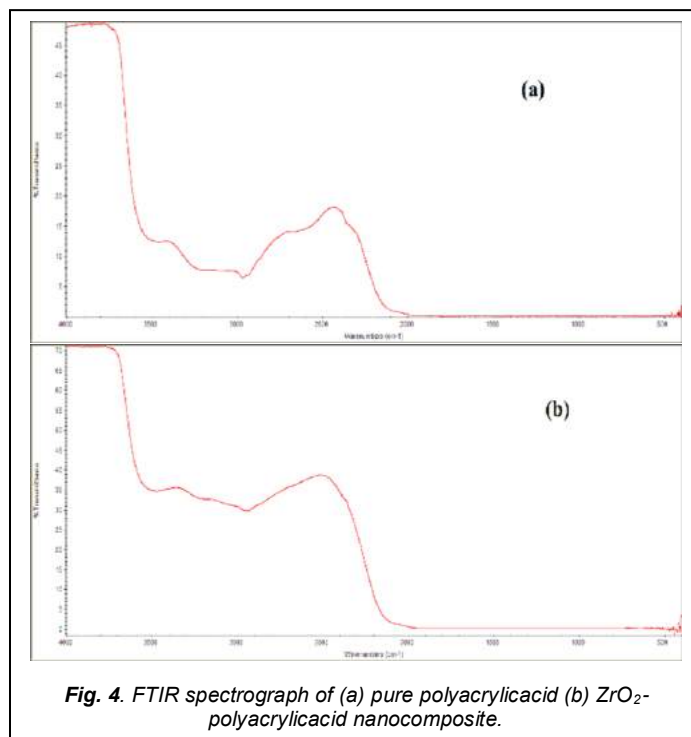


Fig. 4. FTIR spectrograph of (a) pure polyacrylicacid (b) ZrO_2 -polyacrylicacid nanocomposite.

for the wavelength range of 280nm to 900nm. Fig. 5 (a-b) shows the absorption spectra of ZrO_2 -polyacrylicacid nanocomposites with different concentration of ZrO_2 with 0.1% and 0.5% respectively. A well-defined peak is obtained around 290nm in the absorbance curve. It reveals that the absorbance increases because the amount of ZrO_2 increases in the sample [12]. This directly proves that with varying doping concentration we can get a desired energy band gap for ZrO_2 nanomaterial.

3.6 Photoluminescence (PL) Spectroscopy

Photoluminescence spectra were obtained by Horiba Jobin Yvon make Fluoromax-4 Spectrofluorometer. Emission spectra for both the samples are shown in Fig. 6 (a-b).

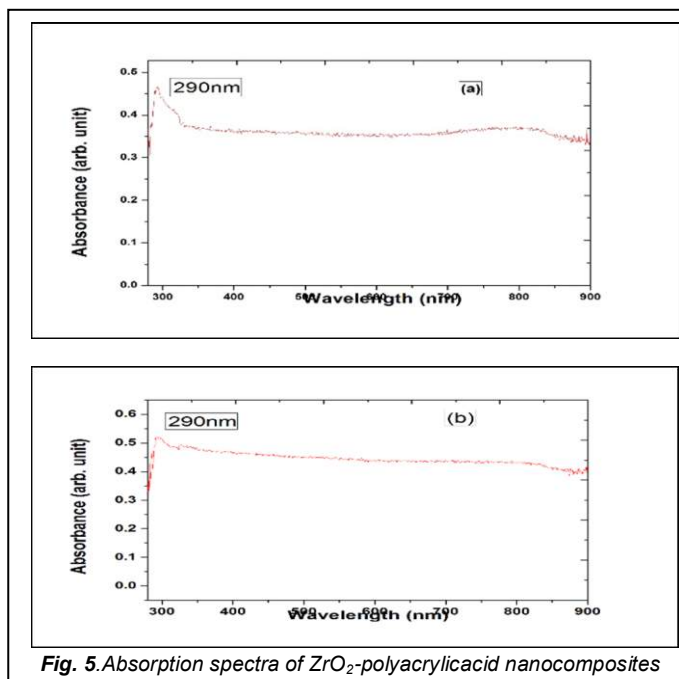


Fig. 5. Absorption spectra of ZrO_2 -polyacrylicacid nanocomposites

The samples were excited at 300nm, the additional emission peak was obtained at 465nm in both the samples of ZrO₂-polyacrylicacid nanocomposites. This peak may be obtained due to interstellar defect created by ZrO₂ in the polyacrylicacid film [13].

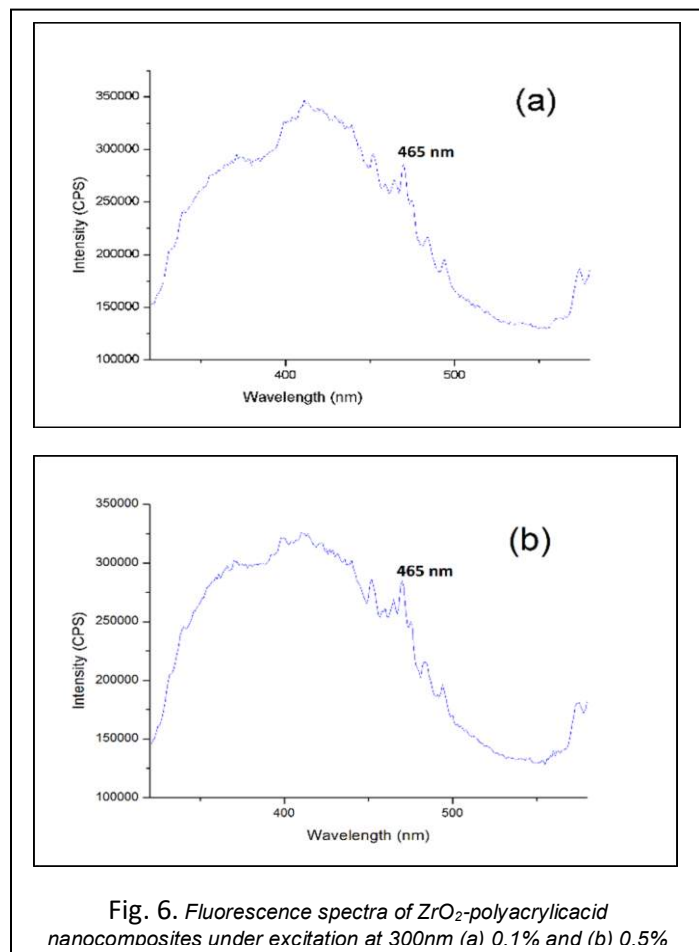


Fig. 6. Fluorescence spectra of ZrO₂-polyacrylicacid nanocomposites under excitation at 300nm (a) 0.1% and (b) 0.5%

4 CONCLUSION

We have successfully synthesized ZrO₂ nanoparticles by hydrothermal technique. Samples of ZrO₂-polyacrylicacid nanocomposites were prepared with different concentration of zirconia. With the help of XRD the crystalline size of ZrO₂ calculated with the Scherer formula was found 12.1nm and the phase of ZrO₂ nanoparticles were monoclinic and tetragonal. SEM gives good morphological properties showing no significant change in structure of PAA due to ZrO₂ doping and the

EDX analysis confirmed that the samples were composed of C, O and Zr elements. FTIR spectrographs shows that the transmittance increases in the case of ZrO₂-polyacrylicacid with compare to pure acrylicacid and UV-Vis spectroscopy revealed that a well-defined peak is obtained around 290nm in the absorbance curve, the absorbance increases as the amount of ZrO₂ increases in the samples so we can have desired band gap of material as well. Photoluminescence spectra shows an additional peak obtained around 465nm with good intensity as a significance of ZrO₂ in the samples.

ACKNOWLEDGEMENT

The work is supported by University Grants Commission (UGC), India.

REFERENCES

- [1] RAY S.S., OKAMOTO M., Prog. Polym. Sci., 28 (2003), 1539.
- [2] KICKELBICK G., Prog. Polym. Sci., 28 (2003), 83.
- [3] V. R. Gowariker, Polymer Science, Age International (P) Limited, Publishers.
- [4] Byrappa K (ed.), Recent progress in the hydrothermal growth of crystals, "Recent progress in crystal growth and characterization of materials," Pergamon Press, Oxford, UK, (1991) 199-254.
- [5] M.R. Loghman-Estarki, H. Edris, R. Shoja Razavi, Large scale synthesis of non-transformable tetragonal Sc₂O₃, Y₂O₃ doped ZrO₂ nanopowders via the citric acid based gel method to obtain plasma sprayed coating, Ceram. Int. 1 (39) (2013) 7817–7829.
- [6] H.D.E. Harrison, N.T. McLamed, E.C. Subbarao, J. Electrochem. Soc. 110 (1963) 23.
- [7] G.A. Kourouklis, E. Liarokapis, J. Am. Ceram. Soc. 74 (1991) 52.
- [8] I. Birkby, R. Stevens, Key Eng. Mater. 122 (1996) 527.
- [9] Y. Murase, E. Kato, J. Am. Ceram. Soc. 66 (1982) 196.
- [10] M. Venkatesan, C. Fitzgerald and J. Coey, Unexpected magnetism in a dielectric oxide, Nature. 430 (2004) 630.
- [11] Autoclave Engineers, Catalogue Brice LC Hydrothermal growth, crystal growth processes, (1986) Blackie Halsted Press, Glasgow, 194.
- [12] Nanotechnology : principles and practices by Sulbha .K. Kulkarni
- [13] P. Deniss Christy, N. S. Nirmala Jothi, N. Melikechi and P. Sagayaraj, "Synthesis, structural and optical properties of well dispersed anatase TiO₂ nanoparticles by non-hydrothermal method," Crystal Research and Technology, vol. 44, issue 5, (2009) 484-488.